

NATIONAL ACADEMY OF SCIENCES OF UKRAINE  
G. V. KURDYUMOV INSTITUTE FOR METAL PHYSICS

Manuscript

**Mazur Dmytro Viktorovych**

Copy #\_\_\_\_\_  
UDK 538.915; 544.22; 537.632

**Features of x-ray absorption and magnetic circular dichroism  
spectra of the 4th period metal compounds containing oxygen.**

**Scientific Advisor**  
Corresponding member of NAS of Ukraine  
**Prof. Dr. Habil. Antonov Victor Mykolayovych**

Kyiv, 2024

## CONTENTS

<b>1 Overview</b>	<b>4</b>
1.1 ZnO-based DMS . . . . .	5
1.2 A-site ordered double perovskites. . . . .	9
<b>2 Theoretical framework</b>	<b>13</b>
2.1 Density Functional Theory . . . . .	13
2.2 Linear Method of MT Orbitals . . . . .	21
2.3 Magneto-optical effects . . . . .	51
<b>3 Electronic band structure and x-ray spectra in ZnO-based diluted magnetic semiconductors</b>	<b>60</b>
3.1 Crystal structure and details of calculations . . . . .	60
3.2 (Zn,V)O . . . . .	62
3.3 (Zn,Mn)O . . . . .	65
3.4 (Zn,Fe)O . . . . .	71
3.5 (Zn,Co)O . . . . .	73
3.6 Conclusions for Chapter 3 . . . . .	80
<b>4 Electronic band structure and x-ray spectra in A-site ordered double perovskites</b>	<b>81</b>
4.1 CaMnTi <sub>2</sub> O <sub>6</sub> . . . . .	81
4.2 CaCo <sub>3</sub> V <sub>4</sub> O <sub>12</sub> . . . . .	90
4.3 Conclusions for Chapter 4 . . . . .	97
<b>5 Conclusions</b>	<b>98</b>
<b>Bibliography</b>	<b>99</b>

## ABBREVIATIONS

<i>ab initio</i>	from first principles
AFM	antiferromagnetic
DFT	density-functional theory
DMS	diluted magnetic semiconductor
DOS	density of states
$E_F$	the Fermi energy
FM	ferromagnetic
GGA	generalized gradient approximation
LMTO	linear muffin-tin method
L(S)DA	local (spin) density approximation
PM	paramagnetic
$T_C$	Curie temperature
TM	transition metal
XA	x-ray absorption
XLD	x-ray linear dichroism
XMCD	x-ray magnetic circular dichroism

# CHAPTER 1

## OVERVIEW

The original results presented in this manuscript are published in [1–5].

Spintronics is a multidisciplinary field whose central theme is the active manipulation of spin degrees of freedom in solid-state systems [6]. The goal of spintronics is to understand the interaction between the particle spin and its solid-state environments and to make useful devices using the acquired knowledge. Fundamental studies of spintronics include investigations of spin transport in electronic materials, as well as of spin dynamics and spin relaxation.

Spintronics covers at least two large groups of interest, those that are used in the novel applications and those already investigated and applied in well-established schemes and materials. The latter group, often described as magnetoelectronics typically covers paramagnetic and ferromagnetic metals and insulators, which utilize magnetoresistive effects, realized, for example, as magnetic read heads in computer hard drives, circuit insulators, and nonvolatile magnetic random access memory (MRAM). The nonvolatile nature of MRAM makes it one of its biggest benefit points when compared to dynamic random access memory (DRAM). MRAM can also deliver better read and write speeds and operate at lower voltages, and it has the potential to offer greater scalability. In addition, MRAM does not require periodic charge refreshes like DRAM and retains data after the power supply is disconnected. The commercially-produced MRAM products and the vast majority of MRAM technologies under development are based on magnetic tunnel junction (MTJ) devices which operate because of electron tunneling. An MRAM device is made up of an array of MTJs that are connected to form the circuitry. This is similar to how arrays of transistors in an integrated circuit form DRAM.

Spintronics also benefits from a large class of emerging materials, such as ferromagnetic semiconductors, organic semiconductors, organic ferromagnets, high-temperature superconductors, and carbon nanotubes, which can bring novel functionalities to the traditional devices. The physical properties of these materials can be tuned by both charge and spin, thus, they have great potential of being used in magneto-optical, magneto-electrical, and magneto-transport devices. Spintronics is an emerging field of

nanoscale electronics involving the detection and manipulation of electron spin. This field is in-between magnetic and electrical properties of semiconductors [7]. DMSs obtained by doping magnetic element as impurity into the host semiconductor are ferromagnetic semiconductors and can be used for spintronic devices [8]. In DMS, apart from electron charge degree of freedom, one uses the spin degree of freedom which can lead to a new class of devices and circuits.

The starting materials, which were expected to be the promising candidates for spintronics are Group III-V materials, such as (Ga,Mn)As [9, 10] with the highest  $T_C \sim 110\text{ K}$  [11]. Other candidates, which can show this property, are transition metal doped Group III nitrides, phosphides and semiconducting oxides. Dietl *et al.* [12] predicted theoretically a Curie temperature  $T_C$  higher than room temperature for transition element doped semiconducting materials, such as, GaN and ZnO. After the report of  $T_C \sim 280\text{ K}$  in (Zn,Co)O [13], there have been many reports on ZnO-based DMSs showing high  $T_C$  [14].

### 1.1 ZnO-based DMS

**ZnO.** Zinc oxide, a representative wide-band-gap II-VI compound semiconductor, has attracted considerable attention due to its many attractive properties, such as its direct wide band gap  $E_g = 3.37\text{ eV}$ , large exciton binding energy (60 meV at room temperature), good piezoelectric characteristics, chemical stability and biocompatibility. This suggests a host of possible practical applications such as energy efficient or smart windows, electrodes for solar cells, flat-panel displays, *etc.* [15]. Recently, ZnO has been widely considered as a candidate for *transparent* diluted magnetic semiconductors with potentially high  $T_C$  [16], aiming at practical applications in spintronic devices.

The electronic and the magnetic properties of TM-doped ZnO have been calculated *ab initio* by using a wide range of different methods, such as the Korringa-Kohn-Rostoker coherent potential approximation [17–19], the LMTO method [20–22], the full potential local orbital band structure method [23], the nonlocal Hartree-Fock method [24], the real-space multiple-scattering approach [25], the projector augmented wave method [26–31] and the pseudopotential method [32–36], all based on the LSDA. The

self-interaction-corrected LSDA to investigate the ground-state valence configuration of TM = Mn and Co impurities in ZnO is used in [37]. The most of recent *ab initio* investigations of the electronic structure, magnetism and transport properties of DMSs based on electronic structure theory within the LSDA to DFT are summarized in [38].

In wide band gap DMS for low concentrations (e.g., well below percolation threshold), due to the spinodal decomposition phase, nanoclusters of magnetic impurities are formed [39]. This phase formation always suppresses  $T_C$  because produced nanoclusters are well separated and have no magnetic correlation with each other due to the short-ranged interactions. Thus, the system shows superparamagnetism (i.e.,  $T_C = 0$ ). However, according to the phenomenology of the superparamagnetism, one can observe ferromagnetic (hysteretic) behavior in the magnetization process at finite temperature due to the blocking effect [40]. Using *ab initio* and Monte Carlo calculations of superparamagnetic blocking phenomena in the spinodal decomposition phases it is shown how the formation of the nanoclusters affects the magnetic properties of DMSs [40–43].

**Defects in ZnO.** The physical properties of ZnO are well known to be very sensitive to different kinds of defects in the crystal. In spite of numerous experimental studies controversy still exist as to what are the relevant native defects of this oxide. Single-crystal ZnO has always been observed to contain metal excess (or oxygen deficiency) [44]. The metal excess can be accommodated in part by the presence of zinc interstitials or oxygen vacancies. Experiments have been inconclusive as to which of these is the predominant defect. Results presented in the literature point in both directions, and different interpretations have even been given for the same set of experimental data (see, for example, Ref. [45]). Interstitial zinc atoms have been proposed as the dominant defect on the basis of ionic diffusion or size considerations [44, 46–48]. Other authors, based on calculation of reaction rates [45], diffusion experiments [49], or electrical conductivity and Hall effect measurements [50] have concluded that oxygen vacancies give the predominant defect. One would expect that unsolved problem of defects in pure ZnO will transfer to TM-doped ZnO.

**(Zn,Co)O.** After the report of  $T_C \sim 280$  K in (Zn,Co)O [13], there are many reports on ZnO-based DMSs showing high  $T_C$ . A review is presented in [14]. There have been

a number of reports on the growth of (Zn,Co)O films [13, 51, 52] and characterization of their structural, magnetic, and optical properties. However, substantial disagreement of the magnetic and optical properties of magnetic alloys has been found.

**Defects in (Zn,Co)O.** Despite the partial success, the nature of the host-impurity couplings, and of the FM interactions in TM-doped oxides, is not very well understood. The accumulated experience of experiments with thin films of magnetically doped semiconductors indicates a high sensitivity of the samples to the technology of their preparation and subsequent heat treatment [53]. The existing technologies, e.g. ion implantation, pulsed laser deposition, reactive magnetic sputtering etc. permit one to obtain extremely imperfect films in a state far from thermodynamic equilibrium. Those samples, as a rule, are unstable against transition to a nonuniform state, specifically: precipitations of other crystallographic phases, phase separation of the host matrix into insulating and conducting regions, spinodal decomposition in the magnetic subsystem, the appearance of diffusion and implantation profiles, etc. Even in carefully controlled situations, when the precipitation of parasitic phases and aggregations of superparamagnetic clusters with an excess concentration of magnetic ions are prevented as much as possible, it is impossible to completely avoid the fundamental inhomogeneities of all DMSs, this problem persists for all (Zn,T)O alloys. Therefore it is quite difficult to interpret any experimental measurements without theoretical calculations.

**(Zn,Mn)O.** Mn doped DMSs are most suitable for spintronic applications because the Mn ion possesses the largest magnetic moment compared to other 3d transitional metals and it also creates a fully polarized stable state due to its half-filled 3d bands. There have been several experimental works on (Zn,Mn)O thin films [26, 54–57], powders [26, 58], nanostructures [59–61], and bulks [62]. However, contradictory conclusions, including PM, FM and AFM behaviors have been obtained. Some groups observed high-temperature ferromagnetism in low-temperature-grown bulk and thin films of ZnO doped by Mn [26, 63] whereas others have observed PM or even spin-glass behaviors [54, 64]. In addition, some studies have shown the absence of FM ordering in single-phase (Zn,Mn)O down to 2 K [65]. Moreover, two samples with different Mn concentrations and different magnetic properties at room temperature,

namely FM in the case of  $(\text{Zn}_{0.98}\text{Mn}_{0.02}\text{O})$  and no magnetic order for  $(\text{Zn}_{0.96}\text{Mn}_{0.04}\text{O})$ , have been reported by Bondino *et al.* [66]. The inconsistent results indicate that the magnetic properties of  $(\text{Zn},\text{Mn})\text{O}$  are highly sensitive to the preparation methods and conditions. In fact, depending on the growth modes and mechanisms, microstructures in  $(\text{Zn},\text{Mn})\text{O}$  systems, such as the distribution of Mn ions in  $\text{ZnO}$  crystal lattice and the local environment around Mn ions, are very different, which considerably affects the magnetic properties of the  $(\text{Zn},\text{Mn})\text{O}$ .

**Defects in  $(\text{Zn},\text{Mn})\text{O}$ .** The influence of various defects on the electronic and the magnetic structures of  $(\text{Zn},\text{Mn})\text{O}$  DMSs was investigated theoretically by several authors [18, 19, 25, 67]. Gu *et al.* [67] used the Haldane-Anderson impurity model and the tight-binding approximation to study the FM state in the compound  $(\text{Zn},\text{Mn})\text{O}$ . They found that the FM correlations were strongly influenced by the crystal structure. In particular, in *p*-type  $(\text{Zn},\text{Mn})\text{O}$ , they observed the development of FM correlations with an extended range at low temperatures for wurtzite and zinc-blende crystal structures. However, for the rocksalt structure, no FM correlations were observed between the impurities. Iușan *et al.* [18] studied Mn-doped  $\text{ZnO}$  in the presence of several defects by a using combined approach of *ab-initio* electronic structure calculations with Korringa-Kohn-Rostoker-coherent potential approximation and Monte Carlo simulations. Electronic structure and magnetic interactions are found to have similar trends for wurtzite and zinc-blende crystal structures. A weak AFM interaction is found for 5% Mn doping in defect-free  $\text{ZnO}$ . Defects such as O vacancies and Zn interstitials lead to AFM interactions between the Mn atoms while Zn vacancies and oxygen substitution by nitrogen yield FM interactions. As the concentration of Mn is low and the exchange interactions are short ranged, simulations show the values of the  $T_C$  not more than 50 K. However, for a few cases with codoping of Mn and defects, the higher  $T_C$  of around 130 K are obtained. Based on *ab initio* calculations Yan *et al.* [25] proposed that the Zn vacancy could induce room-temperature FM state in Mn-doped  $\text{ZnO}$ .

**XA and XMCD spectra in DMSs.** Most of interest in previous investigations is concentrated on the nature of the magnetic interactions in the DMSs. In the present study, the focus is on XA, XMCD and XLD spectra in TM-doped  $\text{ZnO}$ -based DMSs.

The XMCD is a powerful tool to study the element-specific local magnetic moments and the spin and orbital polarizations of the local electronic states by measuring the difference of XA intensities of left and right directions of circular polarization.

Field and temperature dependences of the XA and XMCD spectra at the V  $L_{2,3}$  edges are reported by Ishida *et al.* [68]. They found a linear increase of the XMCD signal with external magnetic field indicating that the PM signal dominates the XMCD signal and that the FM component is small, consistent with their magnetization measurements. The XA and the XMCD spectra at the Zn, Mn, and O  $K$  and the  $L_{2,3}$  edges in the Mn-doped ZnO have been measured by several groups [25, 69–80]. The XA and XMCD spectra at the Fe  $L_{2,3}$  edges also have been measured by several groups [71, 81–83]. The XA and XMCD spectra at the Zn, Co, and O  $K$  and  $L_{2,3}$  edges for the Co-doped ZnO have been measured by several groups [84–90, 69, 91–100]. Theoretically dichroism spectra in DMSs have been investigated mostly using atomic multiplet calculations with some adjustable parameters [84, 86, 88, 69, 97, 70]. DFT calculations of XA spectra at Mn, and O  $K$ -edges for the (Zn,Mn)O DMS have also been reported [25, 101].

## 1.2 A-site ordered double perovskites.

The past decade has witnessed dramatic progress in the fundamental physics of multiferroics and magnetoelectrics. The challenge and opportunity for solid state physicists is to identify mechanisms that provide large, robust, and coupled magnetization and polarization, combined with large susceptibilities at low electric or magnetic fields, all at room temperature. Multiferroics continue to reveal novel, unanticipated physics, and the potential applications now stretch far beyond electrical control of ferromagnetism. The recent progress on the basic materials physics aspects stimulates the physics community to dream up entirely new device paradigms that exploit the novel and unique functionalities of multiferroics.

Multiferroics are materials that possess both ferroelectric and magnetic order, and these two types of order have symmetry restrictions that multiferroics must simultaneously satisfy. Ferroelectrics must have their space inversion symmetry broken. This means only crystals with noncentrosymmetric space groups can exhibit ferroelectricity

[102]. There is plenty of fascinating physics in these materials, owing to the strong entanglement of spin-charge-orbital degrees of freedom [103, 104] and great potential for technological applications in energy-efficient information processing and storage [105–107]. For widespread implementation of new technology, the coexistence of long range magnetic and electric orders at room temperature will be required. To present, there is only one material,  $\text{BiFeO}_3$ , known to exhibit ferroelectric and AFM orders above room temperature [108]. Recently, several manganese and iron oxides have been shown to possess strong magnetic coupling and be promising for realizing room-temperature multiferroic materials. However, ferroelectricity in these materials is rather weak [109].

So far, room-temperature ferroelectric materials are generally associated to single perovskites based on second-order Jahn-Teller active cations with  $d^0$  ( $\text{Ti}^{4+}$ ,  $\text{Zr}^{4+}$ ,  $\text{Nb}^{5+}$ ) or  $s^2$  ( $\text{Pb}^{2+}$ ,  $\text{Bi}^{3+}$ ) valence band electron configurations. These cations are prone to anisotropic covalent bonding with ligands inducing structural distortions that may lead to the appearance of a collective polar mode and a macroscopic electric dipolar moment, whenever the relevant distortions do not allow generating antiparallel effects [110].

TM perovskites have been studied for half a century, and most intensively during the last decade, for their fascinating electronic and magnetic properties arising from narrow  $3d$  bands and strong Coulomb correlations [111–115]. Perovskite structure oxides with the general formula  $\text{ABO}_3$  display a large variety of intriguing properties and raise lots of important fundamental issues in solid state physics and chemistry. The structure can be described as a framework of corner-sharing  $\text{BO}_6$  octahedra that has an A-site cavity formed by twelve coordinated oxygen ions. The smaller B-site cations have octahedral coordination by the O anions. The octahedra share corners to form a three dimensional network, while the larger A-site cations sit in the 12-coordinate cubo-octahedral cavities within this network. Perovskites display a wide range of properties including superconductivity (e.g.  $(\text{Ba},\text{K})\text{BiO}_3$ ), colossal magnetoresistance (e.g.  $(\text{La},\text{Ca})\text{MnO}_3$ ), itinerant electron ferromagnetism (e.g.  $\text{SrRuO}_3$ ), multiferroic behavior (e.g.  $\text{TbMnO}_3$ ), ferroelectricity (e.g.  $\text{BaTiO}_3$ ), piezoelectricity (e.g.  $\text{Pb}(\text{Zr},\text{Ti})\text{O}_3$ ), and ionic conductivity (e.g.  $\text{La}_{0.67-\delta}\text{Li}_{0.33-\delta'}\text{TiO}_3$ ,  $\text{BaCeO}_{3-\delta}$ ). Perovskites arguably represent the most important family of complex oxides. Distortions from the ideal perovskite structure can

significantly impact the physical properties. Octahedral tilting distortions, which are present in 80-90% of all perovskites, occur when the A-site cation is too small for the cubo-octahedral cavities [116, 117]. The octahedral tilting distortions alter the conduction bandwidth [118] and the strength of the magnetic superexchange interactions [119] and provide a mechanism for fine tuning the electrical, magnetic and optical properties.

More sophisticated double perovskites, e.g., those that are called “A-site ordered” with the general formula  $\text{AA}'\text{B}_4\text{O}_{12}$ , comprise one more site ( $\text{A}'$ ) for cations with unusual two-dimensional square oxygen coordination. The A-site ordered perovskite-structure oxides  $\text{AA}'\text{B}_4\text{O}_{12}$  can be obtained by filling 3/4 of the A sites with small TM cations and the other 1/4 with larger alkali, alkaline earth, or rare earth cations. They have a  $2a \times 2a \times 2a$  structure stabilized by heavy-tilted  $\text{BO}_6$  octahedra and consequently forming  $\text{A}'\text{O}_4$  square-planar units. Cu and Mn are typical TM cations readily accommodated by the  $\text{A}'$  site. Compounds with this structure type were synthesized in the 1960s and 1970s [120, 121], and recently lots of fascinating functional properties have been discovered in this class of compounds. Among them are a large dielectric constant in  $\text{CaCu}_3\text{Ti}_4\text{O}_{12}$  [122], a large negative thermal-expansion-like volume change due to intersite charge transfer in  $\text{LaCu}_3\text{Fe}_4\text{O}_{12}$  [123], and multiferroism in  $\text{CaMn}_3\text{Mn}_4\text{O}_{12}$  (or  $\text{CaMn}_7\text{O}_{12}$ ) [124]. New A-site ordered perovskites with novel properties recently have attracted much attention [125]. These perovskites not only have the B-B interaction (or B-O-B interaction via oxygen ions) largely responsible for the properties of simple perovskites but also have interactions between the TM ions at the  $\text{A}'$  sites ( $\text{A}'\text{-A}'$  interaction) and between those at the  $\text{A}'$  and B sites ( $\text{A}'\text{-B}$  interaction).

Among different families of the A-site ordered  $\text{AA}'\text{B}_4\text{O}_{12}$  double perovskites, the most studied to date are compounds with  $\text{B} = \text{Fe}$  due to their nontrivial magnetic properties and charge disproportionation reactions, which can lead to spectacular phenomena [123]. Members of other double-perovskite families, e.g., those of V-based perovskites,  $\text{AA}'_3\text{V}_4\text{O}_{12}$ , also find various applications, but they are less systematically studied to date [126, 127]. Recent investigations of some vanadium compounds show that V-based perovskites may reveal rather spectacular and novel physical properties [127, 128].

Recently, Aimi *et al.* [129] have synthesized a new tetragonal double perovskite

ferroelectric  $\text{CaMnTi}_2\text{O}_6$  with less common A-site order and proved that A-site ordering and second-order Jahn-Teller distortions can couple to enable ferroelectricity. Gou *et al.* [130] identify the origin of the ferroelectricity in  $\text{CaMnTi}_2\text{O}_6$  using *ab initio* calculations combined with detailed symmetry analyses. They explore the material properties of  $\text{CaMnTi}_2\text{O}_6$ , including its ferroelectric polarization, dielectric and piezoelectric responses, magnetic order, electronic structure, and optical absorption coefficient. It is found that  $\text{CaMnTi}_2\text{O}_6$  exhibits room-temperature-stable ferroelectricity and moderate piezoelectric responses.  $\text{CaMnTi}_2\text{O}_6$  presents a new class of ferroelectric perovskites for potential applications in ferroelectric photovoltaic solar cells. Soft XA and XMCD spectra for  $\text{CaMnTi}_2\text{O}_6$  have been measured recently by Herrero-Martin *et al.* [110].

$\text{CaCo}_3\text{V}_4\text{O}_{12}$  has been synthesized by Ovsyannikov *et al.* [131]. It has been shown that this new double perovskite possesses high-spin  $\text{Co}^{2+}$  ions in the  $Im\bar{3}$  cubic symmetry. The magnetic susceptibility measured on bulk polycrystalline samples of  $\text{CaCo}_3\text{V}_4\text{O}_{12}$  shows a sharp maximum around 98 K, which is a characteristic of an AFM ordering transition. The authors established that the  $\text{Co}^{2+}$  ions in  $\text{Co}_3\text{V}_4\text{O}_{12}$  are in the high-spin state with a sizable orbital moment. Electrical resistivity data suggest semiconducting behavior in the temperature range of 1.6–370 K. The chemical formula of this perovskite can be written as  $\text{Ca}^{2+}\text{Co}_3^{2+}\text{V}_4^{4+}\text{O}_{12}^{2-}$ . Later Ovsyannikov *et al.* have investigated the structural, vibrational, magnetic, and electronic properties of the  $\text{CaCo}_3\text{V}_4\text{O}_{12}$  perovskite at low temperatures and high pressure [127]. They have found no apparent signatures of metallization of this perovskite up to 60 GPa. From the high-pressure thermoelectric power measurements its electrical conduction is described as semimetallic and strongly compensated. By means of ambient-pressure neutron powder diffraction, the authors established that below 100 K  $\text{CaCo}_3\text{V}_4\text{O}_{12}$  transforms into an AFM phase in which all the magnetic moments of the  $\text{Co}^{2+}$  ions are aligned along the *c*-axis, and the magnetic structure has a 2-fold periodicity along this axis. They also have measured the XA spectra at the Ca, Co, and V *K* edges at 70 K and 298 K.

The energy band structure of  $\text{CaCo}_3\text{V}_4\text{O}_{12}$  is calculated within the *ab initio* approach taking into account strong electron correlations by applying a GGA to the DFT supplemented by a Hubbard *U* term (GGA+*U*) [132].

## CHAPTER 2

### THEORETICAL FRAMEWORK

#### 2.1 Density Functional Theory

*Ab initio* theoretical investigation of solids ends in obtaining a quantum many-body problem solution. In general, that requires the Schrödinger or Dirac equation to be solved for an enormous number of nuclei and electrons. It is out of question to deal with the task of such difficulty without any approximations, and the first one is to “freeze” the nuclei at fixed positions, taking into account only the electron subsystem. In this so called Born-Oppenheimer adiabatic approximation the non-relativistic Hamiltonian of a many-electron system in a crystal with the ideal lattice is (in atomic units)

$$H = - \sum_i \nabla_i^2 + \sum_i V(\mathbf{r}_i) + \sum'_{i,j} \frac{2}{|\mathbf{r}_i - \mathbf{r}_j|}, \quad (2.1)$$

where the first term is the sum of the kinetic energies of the individual electrons, the second defines the interaction of each of these electrons with the external potential generated by the nuclei, and the final term contains the repulsive Coulomb interaction energy between pairs of electrons.

It is interesting to note here that the kinetic and electron-electron terms are independent of the particular kind of a many-electron system ( $\text{Br}_2$  or  $\text{H}_2\text{O}$ , Cu or Fe, bcc-Fe or fcc-Fe, ...), they are universal. System-specific information (which nuclei and on which positions) is given entirely by the second term of the above equation.

The motion of electrons in condensed media is highly correlated. At first glance, this leads to the conclusion that it is impossible to describe such a system in an approximation of independent particles. However, we can use a model system of non-interacting particles, where the total energy  $E$  and the electron density  $\rho(\mathbf{r})$  match similar functions of the real system, and all the effects of interactions between electrons are described by an external field. This is the essence of the DFT.

**Formalism.** The DFT is based on the Hohenberg and Kohn theorem [133] whereby there is one-to-one correspondence between the ground state electron density  $\rho(\mathbf{r})$  of a many-electron system and the external potential  $v_{\text{ext}}(\mathbf{r})$ , and thus all ground state

properties of the interacting electron gas can be retrieved in a unique way from the electron density  $\rho(\mathbf{r})$  only, i.e. they can be described by introducing certain functionals of the density. The standard Hamiltonian of the system is replaced by [134]

$$E[\rho] = \int d\mathbf{r} \rho(\mathbf{r}) v_{\text{ext}}(\mathbf{r}) + \int \int d\mathbf{r}' d\mathbf{r} \frac{\rho(\mathbf{r}') \rho(\mathbf{r})}{|\mathbf{r}' - \mathbf{r}|} + G[\rho], \quad (2.2)$$

where  $v_{\text{ext}}(\mathbf{r})$  is the external potential. The functional  $G[\rho]$  includes the kinetic and exchange-correlation energy of electrons. The ground state total energy of the system is given by the minimal value of the functional  $E[\rho]$  which is reached for the ground state electron density corresponding to  $v_{\text{ext}}(\mathbf{r})$ . Note that  $G[\rho]$  is universal and does not depend on any external fields.

Sham and Kohn [135] suggested a form for  $G[\rho]$

$$G[\rho] = T[\rho] + E_{\text{xc}}[\rho], \quad (2.3)$$

where  $T[\rho]$  is the kinetic energy of the system of noninteracting electrons with density  $\rho(\mathbf{r})$  and the functional  $E_{\text{xc}}[\rho]$  contains many-electron effects, namely the exchange and correlation.

The ground state can be found by minimizing  $E[\rho]$  with respect to single-particle wave functions  $\varphi_i(\mathbf{r})$  subject to the usual normalization constraints  $\langle \varphi_i | \varphi_j \rangle = \delta_{ij}$ .

The Lagrange multiplier method of minimization leads to the Kohn-Sham Schrödinger-like equations

$$\left[ -\nabla^2 - \sum_I \frac{2Z_I}{|\mathbf{r} - \mathbf{R}_I|} + \int d\mathbf{r}' \frac{2\rho(\mathbf{r}')}{|\mathbf{r}' - \mathbf{r}|} + V_{\text{xc}}(\mathbf{r}) \right] \varphi_i = \varepsilon_i \varphi_i. \quad (2.4)$$

Here,  $\mathbf{R}_I$  is the position of the nucleus  $I$  of charge  $Z_I$ .  $\varepsilon_i$  are the Lagrange factors forming the energy spectrum of one-particle states. The exchange-correlation potential  $V_{\text{xc}}$  is a functional derivative

$$V_{\text{xc}}(\mathbf{r}) = \frac{\delta E_{\text{xc}}[\rho(\mathbf{r})]}{\delta \rho(\mathbf{r})}. \quad (2.5)$$

The exact ground state electron density of a  $N$ -electron system is

$$\rho(\mathbf{r}) = \sum_{i=1}^N |\varphi_i(\mathbf{r})|^2, \quad (2.6)$$

where the single-particle wave functions  $\varphi_i(\mathbf{r})$  are the  $N$  lowest-energy solutions of Kohn-Sham equations (2.4).

Thus to find the ground state of a many-electron system Schrödinger-like equations for non-interacting particles described by the wave functions  $\varphi_i(\mathbf{r})$  should be solved.

Although the DFT is rigorously substantiated only for the ground state, and for the exchange-correlation energy functional there are at present only rough approximations, the importance of this theory to practical applications can hardly be overestimated, since it reduces the many-electron problem to an essentially one-particle problem with the effective local potential

$$V(\mathbf{r}) = - \sum_I \frac{2Z_I}{|\mathbf{r} - \mathbf{R}_I|} + \int d\mathbf{r}' \frac{2\rho(\mathbf{r}')}{|\mathbf{r}' - \mathbf{r}|} + V_{xc}(\mathbf{r}). \quad (2.7)$$

Obviously, Kohn-Sham equations (2.4) should be solved self-consistently, since  $V(\mathbf{r})$  depends on the orbitals  $\varphi_i(\mathbf{r})$  which are being searched.

Equations (2.2)–(2.6) are exact in so far as they define exactly the electron density and the total energy when an exact value of the functional  $E_{xc}[\rho]$  is given. Thus, the central issue in applying DFT is the way in which the functional  $E_{xc}[\rho]$  is defined.

The formally exact expression of  $E_{xc}[\rho]$  for the *inhomogeneous* electron gas may be written as the Coulomb interaction between an electron and the exchange-correlation hole with the charge density  $\rho_{xc}(\mathbf{r}, \mathbf{r}' - \mathbf{r})$  which surrounds it (the region immediately surrounding any electron is depleted of other electrons because of the Pauli exclusion principle and electrostatic repulsion; this positively charged region is the exchange-correlation hole) [136–138]:

$$E_{xc}[\rho] = \frac{1}{2} \int d\mathbf{r} \rho(\mathbf{r}) \int d\mathbf{r}' \frac{\rho_{xc}(\mathbf{r}, \mathbf{r}' - \mathbf{r})}{|\mathbf{r}' - \mathbf{r}|}. \quad (2.8)$$

In (2.8),  $\rho_{xc}$  is defined as

$$\rho_{xc}(\mathbf{r}, \mathbf{r}' - \mathbf{r}) = \rho(\mathbf{r}') \int_0^2 d\lambda [g(\mathbf{r}', \mathbf{r}; \lambda) - 1], \quad (2.9)$$

where  $g(\mathbf{r}', \mathbf{r}; \lambda)$  is the pair correlation function,  $\lambda$  is the coupling constant.

The functional  $E_{xc}[\rho]$  turns out to be independent of the actual shape of the exchange-correlation hole. Indeed, the variable substitution  $\mathbf{R} = \mathbf{r}' - \mathbf{r}$  in (2.8) allows to perform integration over angles of the vector  $\mathbf{R}$ , so that [139]

$$E_{xc}[\rho] = 2\pi \int d\mathbf{r} \rho(\mathbf{r}) \int dR R \bar{\rho}_{xc}(\mathbf{r}, R), \quad (2.10)$$

$$\bar{\rho}_{xc}(\mathbf{r}, R) = \frac{1}{4\pi} \int d\hat{\mathbf{R}} \rho_{xc}(\mathbf{r}, \mathbf{R}). \quad (2.11)$$

Thus the  $E_{xc}[\rho]$  is in fact depends only on the spherically averaged charge density, which follows from the isotropic nature of the Coulomb interaction. Since the hole contains one electron, the hole charge density satisfies the sum rule [139]

$$4\pi \int dR R^2 \bar{\rho}_{xc}(\mathbf{r}, R) = -2. \quad (2.12)$$

**Local Density Approximation.** The simplest and most frequently used approximation for the exchange-correlation potential  $V_{xc}(\mathbf{r})$  is the LDA, where  $\rho_{xc}(\mathbf{r}, \mathbf{r}' - \mathbf{r})$  has a form similar to that for a homogeneous electron gas, but with the density at every point of the space replaced by the local value of the charge density  $\rho(\mathbf{r})$ :

$$\rho_{xc}(\mathbf{r}, \mathbf{r}' - \mathbf{r}) = \rho(\mathbf{r}) \int_0^2 d\lambda [g_0(|\mathbf{r}' - \mathbf{r}|; \lambda) - 1], \quad (2.13)$$

where  $g_0(|\mathbf{r}' - \mathbf{r}|; \lambda)$  is the pair correlation function of a homogeneous electron system. This approximation satisfies the sum rule (2.12), which is one of its basic advantages. Substituting (2.13) into (2.8) we obtain the LDA functional[134]:

$$E_{xc}[\rho] = \int d\mathbf{r} \rho(\mathbf{r}) \varepsilon_{xc}(\rho(\mathbf{r})). \quad (2.14)$$

Here,  $\varepsilon_{xc}$  is the contribution of exchange and correlation into the total energy (per electron) of a homogeneous interacting electron gas with the density  $\rho(\mathbf{r})$ . This approximation corresponds to surrounding every electron by an exchange-correlation hole and must, as expected, be quite good when  $\rho(\mathbf{r})$  varies slowly. Calculations of  $\varepsilon_{xc}$  by several techniques led to results which differed from one another by a few percent [140]. Therefore, we may consider the quantity  $\varepsilon_{xc}(\rho)$  to be well defined enough. The interpolation expression for  $\varepsilon_{xc}(\rho)$  was given by Hedin and Lundquist [141]. In the LDA, the effective potential (2.7) is

$$V(\mathbf{r}) = - \sum_I \frac{2Z_I}{|\mathbf{r} - \mathbf{R}_I|} + \int d\mathbf{r}' \frac{2\rho(\mathbf{r}')}{|\mathbf{r}' - \mathbf{r}|} + \mu_{xc}(\mathbf{r}), \quad (2.15)$$

where  $\mu_{xc}(\mathbf{r})$  is the exchange-correlation part of the chemical potential of a homogeneous interacting electron gas with the local density  $\rho(\mathbf{r})$ ,

$$\mu_{xc}(\mathbf{r}) = \frac{d(\rho(\mathbf{r})\varepsilon_{xc}(\rho(\mathbf{r})))}{d\rho(\mathbf{r})}. \quad (2.16)$$

For spin-polarized systems, the LSDA [135, 142] is used

$$E_{xc}[\rho^+, \rho^-] = \int d\mathbf{r} \rho(\mathbf{r}) \varepsilon_{xc}(\rho^+(\mathbf{r}), \rho^-(\mathbf{r})). \quad (2.17)$$

Here,  $\varepsilon_{xc}(\rho^+, \rho^-)$  is the exchange-correlation energy per electron of a homogeneous system with the densities  $\rho^+(\mathbf{r})$  and  $\rho^-(\mathbf{r})$  for spins up and down, respectively.

The LDA and LSDA contain no fitting parameter. Furthermore, since the DFT has no small parameter, a purely theoretical analysis of the accuracy of different approximations is almost impossible. Thus, the application of any approximation to the exchange-correlation potential in the real systems may be justified by a tolerable agreement between the calculated and experimental data.

**LDA+U method.** The main difference between the LDA and the exact density functional is that in the latter the potential must jump discontinuously as the number of electrons  $N$  increases through integer values [143] and in the former the potential is

a continuous function of  $N$ . The absence of the potential jump, which appears to the exact density functional, is the reason for LDA failure in describing the band gap of Mott insulators such as transition metal and rare-earth compounds [144]. The second important fact is that while LDA orbital energies which are derivatives of the total energy  $E$  on orbital occupation numbers  $n_i$  ( $\varepsilon_i = \partial E / \partial n_i$ ) are often in rather bad agreement with experiment or more rigorous calculations, the LDA total energy is usually quite good. A good example is a hydrogen atom where the LDA orbital energy is  $-0.54$  Ry (instead of  $-1.0$  Ry) but the total energy ( $-0.976$  Ry) is quite close to  $-1.0$  Ry [145]. The way to overcome this deficiency of the LDA was suggested in Ref. [132] by adding an orbital-dependent correction to LDA potential, the so-called LDA+ $U$  method. The main idea of the LDA+ $U$  method is to separate electrons into two subsystems: localized  $d$  or  $f$  electrons for which the Coulomb  $d$ - $d$  or  $f$ - $f$  interactions should be taken into account in model Hamiltonian (through one-site Coulomb interaction  $U$ ) and delocalized  $s$  and  $p$  electrons which are described by an orbital-independent one-electron potential (LDA).

The meaning of  $U$  has been carefully discussed by Herring [146]. In a  $3d$  electron system with  $n$   $3d$  electrons per atom,  $U$  is defined as the energy cost for the reaction

$$2d^n \rightarrow d^{n+1} + d^{n-1},$$

i.e., the energy cost for moving a  $3d$  electron between two atoms which both initially had  $n$   $3d$  electrons.

Let us consider  $d$  ion as an open system with a fluctuating number of  $d$  electrons. The correct formula for the Coulomb energy of  $d$ - $d$  interactions as a function of the number of  $d$  electrons  $N$  given by the LDA should be  $E = (U/2)N(N - 1)$  [147]. If we subtract this expression from the LDA total energy functional and add a Hubbard-like term (neglecting for a while exchange and nonsphericity) we will have the following functional:

$$E = E_{\text{LDA}} - \frac{U}{2}N(N - 1) + \frac{U}{2} \sum_{i \neq j} n_i n_j. \quad (2.18)$$

The orbital energies  $\varepsilon_i$  are derivatives of (2.18) on orbital occupation numbers  $n_i$ :

$$\varepsilon_i = \partial E / \partial n_i = E_{\text{LDA}} + U (1/2 - n_i).$$

This simple formula gives the shift of the LDA orbital energy  $-U/2$  for occupied orbitals ( $n_i = 1$ ) and  $+U/2$  for unoccupied orbitals ( $n_i = 0$ ). The half-filled orbitals ( $n_i = 1/2$ ) are not shifted. A similar formula is found for the orbital dependent potential  $V_i(\mathbf{r}) = \delta E / \delta n_i(\mathbf{r})$  where variation is taken not on the total charge density  $\rho(\mathbf{r})$  but on the charge density of a particular  $i$ -th orbital  $n_i(\mathbf{r})$ :

$$V_i(\mathbf{r}) = V_{\text{LDA}}(\mathbf{r}) + U(1/2 - n_i). \quad (2.19)$$

Expression (2.19) restores the discontinuous behavior of the exact DFT.

The functional (2.18) neglects exchange and nonsphericity of the Coulomb  $d$ - $d$  interaction. If we take into account exchange, then for electrons with the same spin projection  $\sigma$ , the interaction energy will be  $(U - J)$ , where  $J$  is the exchange parameter, and with different spins it is still  $U$ :

$$E = \frac{U}{2} \sum_{m,m',\sigma} n_{m\sigma} n_{m' - \sigma} + \frac{U - J}{2} \sum_{m',m \neq m',\sigma} n_{m\sigma} n_{m'\sigma}. \quad (2.20)$$

In the LDA exchange is partially taken into account in such a way that the number of electrons with different spin projections are equal ( $N_\uparrow = N_\downarrow$ ,  $N = N_\uparrow + N_\downarrow$ ). That leads to the following expression for the LDA Coulomb energy of  $d$ - $d$  interactions as a function of total number of  $d$  electrons  $N$ :  $(U/2)N(N - 1) - (J/2)N(N - 2)$ .

Finally we could take into account non-sphericity of the Coulomb and exchange interactions, i.e., dependence on what particular orbitals  $m$  and  $m'$  are occupied by introducing matrices  $U_{mm'}$  and  $J_{mm'}$ :

$$U_{mm'} = \sum_k a_k F^k, \quad (2.21)$$

$$J_{mm'} = \sum_k b_k F^k, \quad (2.22)$$

$$a_k = \frac{4\pi}{2k+1} \sum_{q=-k}^k \langle lm | Y_{kq} | lm \rangle \langle lm' | Y_{kq}^* | lm' \rangle, \quad (2.23)$$

$$b_k = \frac{4\pi}{2k+1} \sum_{q=-k}^k | \langle lm | Y_{kq} | lm' \rangle |^2. \quad (2.24)$$

$F^k$  are Slater integrals and  $\langle lm | Y_{kq} | lm' \rangle$  are integrals over products of three spherical harmonics  $Y_{lm}$ .

One can now write the total energy functional in the form [147]:

$$\begin{aligned} E = E_{\text{LDA}} - \frac{U}{2}N(N-1) + \frac{J}{4}N(N-2) + \\ \frac{1}{2} \sum_{m,m',\sigma} U_{mm'} n_{m\sigma} n_{m'-\sigma} + \\ \frac{1}{2} \sum_{m',m \neq m',\sigma} (U_{mm'} - J_{mm'}) n_{m\sigma} n_{m'\sigma}. \end{aligned} \quad (2.25)$$

Let  $U_{\text{eff}} = U - J/2$ . The derivative of (2.25) over orbital occupancy  $n_{m\sigma}$  gives us the expression for the orbital-dependent one-electron potential [147]:

$$\begin{aligned} V_{m\sigma}(\mathbf{r}) = & V_{\text{LDA}}(\mathbf{r}) + \sum_{m'} (U_{mm'} - U_{\text{eff}}) n_{m-\sigma} + \\ & \sum_{m' \neq m} (U_{mm'} - J_{mm'} - U_{\text{eff}}) n_{m\sigma} + U_{\text{eff}} \left( \frac{1}{2} - n_{m\sigma} \right) - \frac{J}{2}. \end{aligned} \quad (2.26)$$

In order to calculate the matrices  $U_{mm'}$  and  $J_{mm'}$  one should know the Slater integrals  $F^k$  ( $F^0$ ,  $F^2$ ,  $F^4$  for  $d$  electrons). The screened Coulomb and exchange parameters  $U$  and  $J$  can be calculated self-consistently in the supercell approximation as described in Ref. [148]. The Coulomb parameter  $U$  can be identified with the Slater integral  $F^0$ . If we average matrices  $U_{mm'}$  and  $(U_{mm'} - J_{mm'})$  over all possible pairs of  $mm'$  we should obtain  $U$  and  $(U - J)$  as in expression (2.20). Using properties of the Clebsch-Gordan coefficients one can prove that this averaging gives [147]:

$$U = \frac{1}{(2l+1)^2} \sum_{mm'} U_{mm'} = F^0, \quad (2.27)$$

$$U - J = \frac{1}{2l(2l+1)} \sum_{mm'} (U_{mm'} - J_{mm'}) = F^0 - (F^2 + F^4), \quad (2.28)$$

$$J = (F^2 + F^4)/14. \quad (2.29)$$

To define all three Slater integrals from  $U$  and  $J$  one needs to know only the ratio  $F^4/F^2$ . In Ref. [149]  $F^2$  and  $F^4$  are tabulated for all  $3d$  metals. The ratio  $F^4/F^2$  for all ions is between 0.62 and 0.63. So if we fix the value of this ratio at 0.625, the expression for the Slater integrals are

$$F^2 = \frac{14}{1.625} J, \quad (2.30)$$

$$F^4 = 0.625 F^2. \quad (2.31)$$

Expressions (2.21)–(2.31) define the so-called LDA+ $U$  method [132, 147]. The most important property of LDA+ $U$  functional is its discontinuity and the maximum occupied orbital energy as the number of electrons increases through an integer value, the absence of which is the main deficiency of the LDA comparing with the exact density functional [143] as far as band gaps are concerned.

The LDA+ $U$  method was proved to be a very efficient and reliable tool in calculating the electronic structure of systems where the Coulomb interaction is strong enough to cause localization of the electrons. It works not only for nearly core-like  $4f$  orbitals of rare-earth ions, where the separation of the electronic states in the subspaces of the infinitely slow localized orbitals and infinitely fast itinerant ones is valid [150], but also for such systems as transition metal oxides, where  $3d$  orbitals hybridize quite strongly with oxygen  $2p$  orbitals [132], and  $5f$  compounds, where the degree of localization of  $f$  states is not so clear as in  $4f$  metals [151].

## 2.2 Linear Method of MT Orbitals

The traditional methods of solving the Kohn-Sham equations (like any other single-particle equations) may be divided into those which express the wave functions as linear combinations of some fixed basis functions and those which employ matching of partial waves. The linear muffin-tin orbital (LMTO) method employs a fixed basis set in the form of muffin-tin orbitals (MTO). A MTO is everywhere continuous and differentiable,

and inside the so-called muffin-tin (MT) spheres it is constructed from the partial waves and their first energy derivatives evaluated at a fixed but arbitrary energy. Outside the spheres the MTO is a spherical wave at fixed energy and phase shift of  $\pi/2$ . If the linear combinations of MTOs are used in a variational procedure the LMTO secular equations in terms of the matrix elements of the single-particle Hamiltonian in the MTO states and overlap matrices are obtained. The equations will give all eigenvalues and eigenvectors at a given point in  $\mathbf{k}$  space in one single matrix diagonalization.

**Atomic Sphere Approximation.** One of the first band theory calculation methods was that proposed by Wigner and Seitz in 1933 [152]. In this method the crystal is divided into polyhedral Wigner-Seitz cells inside which the potential is assumed to be spherically symmetric. This approximation is good enough for close-packed crystal structures with 8–12 nearest neighbors on a central atom. In this case, the solution of the Schrödinger equation of arbitrary energy  $E$  may be represented by the partial waves

$$\Phi_L(\mathbf{r}, E) \equiv i^l u_l(r, E) Y_L(\hat{\mathbf{r}}), \quad (2.32)$$

where the index  $L$  is a combination of the quantum numbers  $l, m$ ;  $u_l$  is the solution of the radial Schrödinger equation.

The wave function of a valence electron in a crystal has the form

$$\Psi_{\mathbf{k}}(\mathbf{r}, E) = \sum_L C_L(\mathbf{k}) \sum_{\mathbf{R}} e^{i\mathbf{k}\cdot\mathbf{R}} \theta(\mathbf{r} - \mathbf{R}) \Phi_L(\mathbf{r} - \mathbf{R}, E). \quad (2.33)$$

Here,  $\mathbf{R}$  is the lattice vector,  $\theta(\mathbf{r})$  is the function equal to unity inside the cell located at the coordinate origin and to zero outside the cell.

If, for a given  $E$  and wave vector  $\mathbf{k}$  we find the coefficients  $C_L(\mathbf{k})$  so that  $\Psi_{\mathbf{k}}(\mathbf{r}, E)$ , and its derivative are continuous functions on passing from one Wigner-Seitz cell to the other, (2.33) is the solution of the Schrödinger equation in the crystal, and  $E$  is the energy eigenvalue for the wave vector  $\mathbf{k}$ . Obviously, these boundary conditions depend on  $\mathbf{k}$  and crystal structure. In the atomic sphere approximation (ASA), when the Wigner-Seitz cell is replaced by a sphere of equivalent volume, this condition reduces

to that specified for the radial logarithmic derivatives

$$D_l(E) \equiv S u'_l(S, E) / u_l(S, E), \quad (2.34)$$

where  $\Omega_0$  is the volume of the Wigner-Seitz cell and the sphere radius is defined from the condition  $S = (3\Omega_0/4\pi)^{1/3}$ .

It has been proved that for an arbitrary  $\mathbf{k}$ -point the boundary condition in the Wigner-Seitz method can almost never be satisfied, while the spherical approximation of the  $\mathbf{k}$ -space is very crude. For this reason, this method was almost never used for 40 years.

To overcome these difficulties, in 1937, Slater proposed to use touching MT spheres [153]. In the MT model, the potential inside the spheres is spherically symmetric, while in the interstitial region it is assumed to be equal to the constant  $V_c$ . In this region, which for the close-packed structures takes up approximately 30% of the cell volume, the kinetic energy of an electron equals  $q_0^2 = E - V_c$ .

Later, the calculation of the band structure is formulated in terms of multiple scattering of an electron wave between the MT spheres which led to the Korringa-Kohn-Rostoker (KKR) method. The major difficulty of the KKR method equations

$$\det|A_{L'L}^{\mathbf{k}}(E) + \delta_{L'L} q_0 \cot \eta_l| = 0, \quad (2.35)$$

written here in the notation of phase shifts, is the dependence of the structure constants  $A_{L'L}^{\mathbf{k}}$  on the energy  $E$ . The potential function in KKR

$$q_0 \cot \eta_l = q_0 \frac{n_l(q_0 S) D_l(S, E) - q_0 S n'_l(q_0 S) / n_l(q_0 S)}{j_l(q_0 S) D_l(S, E) - q_0 S j'_l(q_0 S) / j_l(q_0 S)} \quad (2.36)$$

also depends strongly on  $q_0$ . However, the dependence of the structure constants and potential function on  $q_0$  to a large extent cancel each other out, as was shown in the derivation of a parametric representation of the Fermi surface of transition metals (TM) [154, 155]. Thus, 40 years after the proposal of the cellular method Andersen proposed to return to the ASA but in the KKR formalism [156]. In the ASA, the volume of the

interstitial region is zero, so that only one condition is specified for  $q_0^2$ , i.e., it should approximate the kinetic energy of an electron in all outer regions of the atomic spheres. Andersen used  $q_0^2 = 0$ . This condition significantly simplifies the KKR equations,

$$\det|S_{L'L}^{\mathbf{k}} - \delta_{L'L} P_l(E)| = 0, \quad (2.37)$$

where the potential function is

$$P_l(E) = 2(2l+1) \frac{D_l(E) + l + 1}{D_l(E) - l}, \quad (2.38)$$

the structure constants are

$$S_{L'L}^{\mathbf{k}} = \sum_{\mathbf{R} \neq 0} e^{i\mathbf{k}\mathbf{R}} S_{L'L}(\mathbf{R}), \quad (2.39)$$

$$\begin{aligned} S_{L'L}(\mathbf{R}) &= -\frac{8\pi(2l+2l'-1)!!}{(2l-1)!!(2l'-1)!!} \\ &\times \sum_{L''}^{l''=l+l'} C_{LL''L'}(-i)^{l''} \left(\frac{R_s}{S}\right)^{-l''-1} Y_{L''}(\hat{\mathbf{R}}) \end{aligned} \quad (2.40)$$

and  $C_{LL''L'}$  are the Gaunt coefficients,

$$C_{LL'L''} = \int d\hat{\mathbf{r}} Y_L(\hat{\mathbf{r}}) Y_{L'}^*(\hat{\mathbf{r}}) Y_{L''}(\hat{\mathbf{r}}). \quad (2.41)$$

Equations (2.37)–(2.40) are important because the structure constants (2.39) do not depend on energy. All the information about the crystal potential is contained only in the potential function, while the data on the crystalline structure are contained in the structure constants. Clearly, such a separation considerably simplifies and accelerates the calculation of the band structure. If the contribution of the interstitial region the kinetic energy of an electron is neglected, the error in the eigenvalues does not exceed several percent of the valence band width. Equation (2.37) is obtained as the limit  $q_0 = 0$  from the KKR expression (2.35) and is called the KKR-ASA equation. This expression can also be obtained by introducing the MT orbitals.

**MT orbitals.** Here we consider a *single* atomic sphere. Assume that inside this sphere the potential is spherically symmetric, while outside it  $q_0^2 = E - V_c = 0$ . Then, inside the sphere, the wave function of an electron will satisfy the Schrödinger equation and allow the separation of the variables. Outside the sphere, we have the Laplace equation  $\nabla^2\Psi = 0$ . The radial part of its solution is  $\Phi_l(r) = a_l r^l + b_l r^{-l-1}$ . The coefficients  $a_l$  and  $b_l$  are determined from the condition of continuity and differentiability of the wave function on the sphere surface. Thus, the radial wave function is

$$\Phi_l(r, E) = \begin{cases} u_l(r, E), & r \leq S, \\ \left[ \frac{D_l + l + 1}{2l + 1} \left( \frac{r}{S} \right)^l + \frac{l - D_l}{2l + 1} \left( \frac{r}{S} \right)^{-l-1} \right] u_l(S, E), & r > S, \end{cases}$$

where  $u_l(r, E)$  is the normalized solution of the radial Schrödinger equation in the atomic sphere of the radius  $S$ .

These functions are not used as basis functions since the solution for  $r > S$  contains a diverging wave. Therefore, we write new functions

$$\bar{\Phi}_l(r, D) = \begin{cases} \Phi_l(r, D) - \frac{D + l + 1}{2l + 1} \frac{\Phi_l(S, D)}{\Phi_l(S, l)} \Phi_l(r, l), & r \leq S, \\ \frac{l - D}{2l + 1} \left( \frac{r}{S} \right)^{-l-1} \Phi_l(S, D), & r > S. \end{cases} \quad (2.42)$$

This expression is obtained from  $\Phi_l(r, E)$  by subtracting the diverging wave  $(D + l + 1)(r/S)^l/(2l + 1)$ . Also, for  $r \leq S$ , instead of  $(r/S)^l$  the function  $\Phi_l(r, l)/\Phi_l(S, l)$  is used, and the variable  $E$  is replaced by the logarithmic derivative  $D$  for the corresponding energy  $E$ . This may always be done if the number of nodes of the wave function is known. The function (2.42) is, thus far, not the solution of the Schrödinger equation inside the atomic sphere, however, it is continuous and smooth over the entire space and decreases outside the sphere. Therefore, we can use it to build the basis function  $\bar{\Phi}_L(\mathbf{r}, D) = i^l Y_L(\hat{\mathbf{r}}) \bar{\Phi}_l(r, D)$ .

Let us form a *crystal* by surrounding every atom with a sphere equivalent to the Wigner-Seitz cell, i.e., use the ASA. Here we consider *one* atom per unit cell. In deriving the basis function, it is necessary to include all the tails of the functions contributing

into the central sphere coming from sites situated at  $\mathbf{R}$  with respect to the central sphere.

We write the Bloch sum

$$\chi_L^{\mathbf{k}}(\mathbf{r}, D) = \sum_{\mathbf{R} \neq 0} e^{i\mathbf{k} \cdot \mathbf{R}} \bar{\Phi}_L(\mathbf{r} - \mathbf{R}, D). \quad (2.43)$$

The tail coming from the site at  $\mathbf{R}$ , is

$$\bar{\Phi}_L(\mathbf{r} - \mathbf{R}, D) = i^l Y_L(\widehat{\mathbf{r} - \mathbf{R}}) \left| \frac{\mathbf{r} - \mathbf{R}}{S} \right|^{-l-1} \frac{l-D}{2l+1} \Phi_l(S, D). \quad (2.44)$$

We decompose this function in terms of the angular momentum relative to the center by means of the theorem of additivity [157]:

$$i^l Y_L(\widehat{\mathbf{r} - \mathbf{R}}) \left| \frac{\mathbf{r} - \mathbf{R}}{S} \right|^{-l-1} = 4\pi \sum_{L'' L'}^{l''=l+l'} C_{LL''L'} \frac{(2l''-1)!!}{(2l-1)!!(2l'+1)!!} \times \\ (-i)^{l''} (R/S)^{-l''-1} Y_{L''}^*(\hat{\mathbf{R}}) \times i^{l'} (r/S)^{l'} Y_{L'}(\hat{\mathbf{r}}). \quad (2.45)$$

For the function to be continuous and differentiable on the sphere surface, we must carry out an augmentation, i.e., use  $\Phi_{l'}(r, l')/\Phi_{l'}(S, l')$  instead of  $(r/S)^{l'}$  in (2.45). Finally, we have the basis functions

$$\chi_L^{\mathbf{k}}(\mathbf{r}, D) = \begin{cases} \Phi_L(\mathbf{r}, D) - \Phi_l(S, D) \frac{l-D}{2l+1} \sum_{L'} [S_{L'L}^{\mathbf{k}} - \\ \frac{l+1+D}{l-D} 2(2l+1) \delta_{L'L}] \times \Phi_{L'}(\mathbf{r}, l') \frac{1}{\Phi_{l'}(S, l') 2(2l'+1)}, & r \leq S, \\ \Phi_l(S, D) \frac{l-D}{2l+1} \left[ i^l Y_L(\mathbf{r}) \left( \frac{r}{S} \right)^{-l-1} + \sum_{L'} S_{L'L}^{\mathbf{k}} \right. \\ \left. \times i^{l'} Y_{L'}(\hat{\mathbf{r}}) \left( \frac{r}{S} \right)^{l'} \frac{1}{2(2l'+1)} \right], & r > S, \end{cases} \quad (2.46)$$

where  $S_{L'L}^{\mathbf{k}}$  are defined in (2.39). These are the MT orbitals. The obtained functions can be used as basis function in, for example, the Ritz variational methods.

Note that for the linear combination

$$\Psi_{\mathbf{k}}(\mathbf{r}, E) = \sum_L C_L(\mathbf{k}) \sum_{\mathbf{R}} e^{i\mathbf{k} \cdot \mathbf{R}} \chi_L(\mathbf{k}, \mathbf{r} - \mathbf{R}, D_l(E)) \quad (2.47)$$

of MTO to be the solution of the Schrödinger equation for the entire crystal, it must

be equivalent to (2.33). In other words, inside the central sphere (hence, inside any other sphere), the sum of tails coming from all the other atomic positions are mutually canceled with the unphysical terms of the central MTO proportional to  $i^l r^l Y_L(\hat{\mathbf{r}})$ , i.e., in (2.46), the second term for  $r \leq S$  should go to zero. This condition leads to a set of linear homogeneous equations

$$\sum_L [S_{L'L}^{\mathbf{k}} - \delta_{L'L} P_l(E)] \Phi_l(S, D_l) C_L(\mathbf{k}) = 0, \quad (2.48)$$

with the potential function and structure constants defined in (2.38)–(2.39). We again obtain the KKR-ASA equations.

The problem of calculating the band structure reduces to the determination of eigenvalues and eigenvectors for a single atomic sphere with a spherically symmetric potential with  $\mathbf{k}$ -dependent boundary conditions imposed by the surroundings. The atom sizes and crystal potential are contained in the logarithmic derivatives  $D_l(E)$ , while those of the crystal structure are in the energy independent structure constants  $S_{L'L}^{\mathbf{k}}$  which also do not depend on the lattice constant.

**Relativistic KKR-ASA.** The relativistic KKR-ASA equation is derived just like it is in the nonrelativistic case. Let us consider a single atomic sphere inside which the potential is spherically symmetric and outside of which the electron kinetic energy  $q_0^2 = E - V_c = 0$ . Now, however, the Schrödinger equation is replaced by the Dirac one

$$[c\boldsymbol{\alpha} \cdot \mathbf{p} + \beta c^2/2 + V(\mathbf{r})] \Psi_{\mathbf{k}}(\mathbf{r}, E) = (c^2/2 + E) \Psi_{\mathbf{k}}(\mathbf{r}, E), \quad (2.49)$$

where  $c$  is the speed of light (in atomic units,  $c = 2/\alpha = 274.0746$ ),  $\mathbf{p} = -i\nabla$  is the momentum operator,  $\boldsymbol{\alpha}$  is the Dirac four-dimensional matrix

$$\boldsymbol{\alpha} = \begin{pmatrix} 0 & \boldsymbol{\sigma} \\ \boldsymbol{\sigma} & 0 \end{pmatrix},$$

$\boldsymbol{\sigma}$  corresponds to the set of Pauli matrices

$$\sigma_x = \begin{pmatrix} 0 & 1 \\ 1 & 0 \end{pmatrix}, \quad \sigma_y = \begin{pmatrix} 0 & -i \\ i & 0 \end{pmatrix}, \quad \sigma_z = \begin{pmatrix} 1 & 0 \\ 0 & -1 \end{pmatrix},$$

and the  $\beta$ -matrix is

$$\beta = \begin{pmatrix} 1 & 0 & 0 & 0 \\ 0 & 1 & 0 & 0 \\ 0 & 0 & -1 & 0 \\ 0 & 0 & 0 & -1 \end{pmatrix}.$$

The solution of the Dirac equation with a spherically symmetric potential is

$$\Phi_K(\mathbf{r}, E) = i^l \Phi_\kappa(r, E) Z_K(\hat{\mathbf{r}}), \quad (2.50)$$

where, as usual,  $K = (\kappa, \mu)$ ,  $\kappa$  is the relativistic quantum number,  $\Phi_\kappa(r, E)$  is the matrix of radial solutions,

$$\Phi_\kappa(r, E) = \begin{pmatrix} g_\kappa(r, E) \\ i f_\kappa(r, E) \end{pmatrix}, \quad (2.51)$$

$Z_K(\hat{\mathbf{r}})$  is the matrix of the spin-angular functions

$$Z_K(\hat{\mathbf{r}}) = \begin{pmatrix} \chi_\kappa^\mu(\hat{\mathbf{r}}) & 0 \\ 0 & \chi_{-\kappa}^\mu(\hat{\mathbf{r}}) \end{pmatrix}, \quad (2.52)$$

$$\chi_\kappa^\mu(\hat{\mathbf{r}}) = \sum_{m=\pm 1/2} C_{l,\mu-m,1/2,m}^{j\mu} Y_{l,\mu-m}(\hat{\mathbf{r}}) \chi(m), \quad (2.53)$$

$C_{l,\mu-m,1/2,m}^{j\mu}$  are the Clebsch-Gordan coefficients,  $Y_{lm}(\hat{\mathbf{r}})$  are the spherical harmonics,  $j$  is the eigenvalue of the operator of the total angular momentum  $j = l \pm 1/2$ ,

$$\chi\left(\frac{1}{2}\right) = \begin{pmatrix} 1 \\ 0 \end{pmatrix}, \quad \chi\left(-\frac{1}{2}\right) = \begin{pmatrix} 0 \\ 1 \end{pmatrix}$$

are the Pauli spinors. The spin-angular functions are orthogonal and normalized according to

$$\int d^2\hat{\mathbf{r}} Z_{K'}^\dagger(\hat{\mathbf{r}}) Z_K(\hat{\mathbf{r}}) = I \delta_{K'K}. \quad (2.54)$$

The radial wave functions are normalized in a sphere of radius  $S$ :

$$\langle \Phi_\kappa(r, E) | \Phi_\kappa(r, E) \rangle = \int_0^S dr r^2 (g_\kappa^2(r, E) + f_\kappa^2(r, E)) = 1. \quad (2.55)$$

The relativistic analog of the logarithmic derivative for the radial wave function  $\Phi_\kappa(r, E)$  has the form

$$D_\kappa(E) = S \frac{c f_\kappa(S, E)}{g_\kappa(S, E)} - \kappa - 1. \quad (2.56)$$

Assume  $E = V_c = 0$  in the region outside the atomic sphere. Here, the radial Dirac equations for free electrons

$$\begin{aligned} \left( \frac{d}{dr} + \frac{1-\kappa}{r} \right) \tilde{f}_\kappa(r) &= 0, \\ \left( \frac{d}{dr} + \frac{1+\kappa}{r} \right) \tilde{g}_\kappa(r) - c \tilde{f}_\kappa(r) &= 0 \end{aligned} \quad (2.57)$$

have the solutions [158]

$$\tilde{\Phi}_\kappa(r, D) = \begin{pmatrix} g_\kappa(D, r) \\ i f_\kappa(D, r) \end{pmatrix} = \begin{pmatrix} (r/S)^\kappa \\ i(2\kappa+1)/cS (r/S)^{\kappa-1} \end{pmatrix}, \quad D = \kappa, \quad (2.58)$$

$$\tilde{\Phi}_\kappa(r, D) = \begin{pmatrix} g_\kappa(D, r) \\ i f_\kappa(D, r) \end{pmatrix} = \begin{pmatrix} (r/S)^{-\kappa-1} \\ 0 \end{pmatrix}, \quad D = -\kappa - 1, \quad (2.59)$$

$$\tilde{\Phi}_K(\mathbf{r}, D) = i^l \tilde{\Phi}_\kappa(r, D) Z_K(\hat{\mathbf{r}}). \quad (2.60)$$

Commonly used expression for the singular and regular at the origin solutions (2.58)–(2.59) has the form, respectively

$$\tilde{\Phi}_K(\mathbf{r}, -l-1) = i^l Z_K(\hat{\mathbf{r}}) \begin{pmatrix} (r/S)^{-l-1} \\ i(-l-1+\kappa+1)/cS (r/S)^{-l-2} \end{pmatrix}, \quad (2.61)$$

$$\tilde{\Phi}_K(\mathbf{r}, l) = i^l Z_K(\hat{\mathbf{r}}) \begin{pmatrix} (r/S)^l \\ i(1+\kappa+1)/cS (r/S)^{l-1} \end{pmatrix}. \quad (2.62)$$

Thus, in the region outside the sphere, the solution to the Dirac equation, matching continuously at the surface the solution inside the sphere, will be

$$\Phi_K(\mathbf{r}, D) = i^l Z_K(\hat{\mathbf{r}}) \begin{cases} \begin{pmatrix} g_\kappa(r, D) \\ if_\kappa(r, D) \end{pmatrix}, & r \leq S, \\ g_\kappa(S, D) \left( \frac{D+l+1}{2l+1} \tilde{\Phi}_\kappa(r, l) + \frac{l-D}{2l+1} \tilde{\Phi}_\kappa(r, -l-1) \right), & r > S. \end{cases} \quad (2.63)$$

As in (2.42), we write new functions by subtracting the diverging wave from the Dirac equation solution inside and outside the sphere

$$\bar{\Phi}_K(\mathbf{r}, D) = i^l Z_K(\hat{\mathbf{r}}) \begin{cases} \Phi_\kappa(r, D) - \frac{D+l+1}{2l+1} \frac{g_\kappa(S, D)}{g_\kappa(S, l)} \tilde{\Phi}_\kappa(r, l), & r \leq S, \\ \frac{l-D}{2l+1} \tilde{\Phi}_\kappa(r, -l-1) g_\kappa(S, D), & r > S. \end{cases} \quad (2.64)$$

We use these functions to form the Bloch summation

$$\chi_K^\mathbf{k}(\mathbf{r}, D) = \sum_{\mathbf{R}} e^{i\mathbf{k}\mathbf{R}} \bar{\Phi}_K(\mathbf{r} - \mathbf{R}, D) \quad (2.65)$$

and expand the tail of the function coming from the site situated at  $\mathbf{R}$  about the zero center. For this, we use the generalized theorem of additivity

$$i^l \tilde{\Phi}_\kappa(|\mathbf{r} - \mathbf{R}|, -l-1) Z_K(\hat{\mathbf{r}}) = \sum_{K'} i^{l'} \tilde{\Phi}_{\kappa'}(r, l') Z_{K'}(\hat{\mathbf{r}}) \frac{S_{K'K}(\mathbf{R})}{-2(2l'+1)}, \quad (2.66)$$

where

$$\begin{aligned} S_{K'K}(\mathbf{R}) &= \sum_{LL'L''}^{l''=l+l'} \left( -\frac{1}{2} \right) \frac{4\pi(2l''-1)!!}{(2l-1)!!(2l'-1)!!} C_{l', \mu'-m, 1/2, m}^{j'\mu'} \\ &\times C_{L''L'L}(-i)^{l''} (R/S)^{-l''-1} Y_{L''}^*(\hat{\mathbf{R}}) C_{l, \mu-m, 1/2, m}^{j\mu}, \end{aligned} \quad (2.67)$$

$C_{L''L'L}$  are the Gaunt coefficients.

We do the augmentation as in the nonrelativistic case to obtain expressions for the exact relativistic MTO (RMTO) inside the central sphere (so, inside any other sphere):

$$\begin{aligned}
\chi_K^{\mathbf{k}}(\mathbf{r}, D) &= i^l \Phi_{\kappa}(r, D) Z_K(\hat{\mathbf{r}}) - \frac{D-l}{2l+1} g_{\kappa}(S, D) \\
&\times \sum_{K'} i^{l'} \Phi_{\kappa'}(r, l') Z_{K'}(\hat{\mathbf{r}}) \frac{1}{g_{\kappa}(S, l')} \left( -\frac{1}{2(2l'+1)} \right) \\
&\times \left( S_{K'K}^{\mathbf{k}} - \delta_{K'K} \frac{D+l+1}{D-l} 2(2l+1) \right). \tag{2.68}
\end{aligned}$$

Here

$$S_{K'K}^{\mathbf{k}} = \sum_{\mathbf{R} \neq 0} e^{i\mathbf{k} \cdot \mathbf{R}} S_{K'K}(\mathbf{R}), \tag{2.69}$$

$$S_{K'K}^{\mathbf{k}} = \sum_{m=\pm 1/2} C_{l', \mu'-m, 1/2, m}^{j' \mu'} S_{l', \mu'-m, l, \mu-m}^{\mathbf{k}} C_{l, \mu-m, 1/2, m}^{j \mu}, \tag{2.70}$$

$S_{L'L}^{\mathbf{k}}$  are the structure constants of the nonrelativistic KKR-ASA method. For the linear combination of MT orbitals (2.68) to satisfy the Dirac equation over the entire space, it is required that, inside the central sphere, the sum of tails coming from all other positions be mutually canceled with the nonphysical term of the central MT orbital. This condition leads to the set of linear homogeneous equations

$$\sum_{K'} \left( S_{K'K}^{\mathbf{k}} - \delta_{K'K} 2(2l+1) \frac{D_{\kappa}(E) + l + 1}{D_{\kappa}(E) - l} \right) g_{\kappa}(S, D_{\kappa}) C_K(\mathbf{k}) = 0, \tag{2.71}$$

where the energy  $E$  may take on only those values for which the secular determinant equals zero:

$$\det \left| S_{K'K}^{\mathbf{k}} - \delta_{K'K} 2(2l+1) \frac{D_{\kappa}(E) + l + 1}{D_{\kappa}(E) - l} \right| = 0. \tag{2.72}$$

Like in the nonrelativistic case, the relativistic KKR-ASA method has all the data on the crystal potential function within  $P_{\kappa}(E)$ , while the data on the crystal structure are stored in the structure constants which do not depend on energy. The relativistic structure constants may be calculated from the nonrelativistic analogs using (2.70).

**The LMTO method.** We can use the MTOs (2.46) or the relativistic analogs (2.68) as the trial functions in the variational procedure to find the linear combination of MTOs

$$\det |\langle \chi_{L'}^{\mathbf{k}}(\mathbf{r} - \mathbf{R}'_I) | \mathbf{H} - E | \chi_L^{\mathbf{k}}(\mathbf{r} - \mathbf{R}'_I) \rangle| = 0. \quad (2.73)$$

This method is as time-consuming as the KKR method, allows to use non-MT crystal potentials and frequently yields better convergence than KKR. However, because the MTOs implicitly depend on energy, the computational efforts of this method become comparable to APW and KKR. The situation becomes much simpler if we use energy independent MT orbitals. Below we follow primarily the line of [159].

**Basis functions.** Let us represent the basis radial wave function as an expansion in a Taylor series about an arbitrary point  $E_\nu$  and limit ourselves to the linear term

$$\Phi(r, D) = \Phi_\nu(r) + \omega(D)\dot{\Phi}_\nu(r), \quad (2.74)$$

where  $\Phi_\nu(r) \equiv u_l(r, E_\nu)$ ,  $\dot{\Phi}_\nu(r) \equiv \partial u_l(r, E)/\partial E|_{E=E_\nu}$ .

The functions  $\Phi_\nu(r)$  are normalized to unity in the sphere of the radius  $S$ . The coefficient  $\omega(D)$ , like  $\Phi(r, D)$ , depends on the logarithmic derivative which is chosen by the requirement that  $\Phi(r, D)$  should have the logarithmic derivative on the sphere

$$\omega(D) = -\frac{\Phi_\nu D - D_\nu}{\dot{\Phi}_\nu D - D_{\dot{\nu}}}. \quad (2.75)$$

Here

$$D_\nu = S\Phi'_\nu(S)/\Phi_\nu(S), \quad (2.76)$$

$$D_{\dot{\nu}} = S\dot{\Phi}'_\nu(S)/\dot{\Phi}_\nu(S). \quad (2.77)$$

The amplitude of the function (2.74) on the sphere surface  $\Phi(S, D)$  is defined by

$$\Phi(D) \equiv \Phi(S, D) = \Phi_\nu \frac{D_\nu - D_{\dot{\nu}}}{D - D_{\dot{\nu}}}. \quad (2.78)$$

In the basis set of the functions  $\Phi_L(\mathbf{r}, D) = i^l \Phi_l(D, r) Y_L(\hat{\mathbf{r}})$  the Hamiltonian matrix elements and overlap matrices inside the sphere obviously have the form

$$\langle \Phi_{L'}(D') | \mathbf{H} - E_\nu | \Phi_L(D) \rangle = \delta_{L'L} \omega_l(D), \quad (2.79)$$

$$\langle \Phi_{L'}(D') | \Phi_L(D) \rangle = \delta_{L'L} (1 + \langle \dot{\Phi}_{\nu l}^2 \rangle \omega_l(D') \omega_l(D)). \quad (2.80)$$

Later on we shall use the notations  $\Phi_\nu \equiv \Phi_\nu(S)$ ,  $\dot{\Phi}_\nu \equiv \dot{\Phi}_\nu(S)$ .

Until now we have always considered a single sphere. Below, when we deal with crystals, the influence of each of the spheres on the energy spectrum will be defined by the combination of potential parameters, e.g.  $D_\nu$ ,  $S\Phi_\nu^2$ ,  $S\Phi_\nu\dot{\Phi}_\nu$  and  $\langle \dot{\Phi}_\nu^2 \rangle$ .

However, the first three parameters depend considerably on the selection of  $E_\nu$ . Therefore, in practice it is more convenient to use  $\omega(D_1)$ ,  $S\Phi^2(D_1)$  and  $\Phi(D_1)/\Phi(D_2)$ , where  $D_1 = -l - 1$ ,  $D_2 = l$ . Actually the transition from the first set of parameters to the second with such  $D_1$  and  $D_2$  means that we must use a secant of the energy rather than a tangent. This may bring about various results, but, in most cases the differences are minor. The second combination of parameters appears to be easier to use [see (2.90)]. Note that in this case (2.74), (2.75), (2.77) acquire the following forms, respectively,

$$\Phi_l(r, D) = \frac{\omega_l(D) - \omega_l(-l - 1)}{\omega_l(l) - \omega_l(-l - 1)} \Phi_l(r, l) + \frac{\omega_l(D) - \omega_l(l)}{\omega_l(-l - 1) - \omega_l(l)} \Phi_l(r, -l - 1), \quad (2.81)$$

$$\frac{\omega_l(D) - \omega_l(-l - 1)}{\omega_l(D) - \omega_l(l)} = \frac{\Phi_l(S, -l - 1)}{\Phi_l(S, l)} \frac{D + l + 1}{D - l}, \quad (2.82)$$

$$\Phi_l(S, D) = \frac{(2l + 1)\Phi_l(S, -l - 1)\Phi_l(S, l)}{(D + l + 1)\Phi_l(S, -l - 1) - (D - l)\Phi_l(S, l)}. \quad (2.83)$$

It can also be shown that the following are true

$$\frac{\omega_l(D) - \omega_l(-l - 1)}{\omega_l(l) - \omega_l(-l - 1)} = \frac{D + l + 1}{2l + 1} \frac{\Phi_l(S, D)}{\Phi_l(S, l)}, \quad (2.84)$$

$$\frac{\omega_l(l) - \omega_l(D)}{\omega_l(l) - \omega_l(-l - 1)} = \frac{l - D}{2l + 1} \frac{\Phi_l(S, D)}{\Phi_l(S, -l - 1)}. \quad (2.85)$$

Then, in the Andersen approximation, the MTO (2.46) is

$$\chi_L^k(\mathbf{r}, D) \simeq \frac{\omega_l(l) - \omega_l(D)}{\omega_l(l) - \omega_l(-l - 1)} \chi_L^k(\mathbf{r}) = \alpha_l(D) \chi_L^k(\mathbf{r}), \quad (2.86)$$

where the MTO  $\chi_L^k(\mathbf{r})$  does not depend on energy:

$$\chi_L^k(\mathbf{r}) = \Phi_L(\mathbf{r}, -l - 1) - \Phi_l(S, -l - 1) \sum_{L'} S_{L'L}^k \frac{\Phi_{L'}(\mathbf{r}, l')}{2(2l' + 1)\Phi_{l'}(S, l')} \quad (2.87)$$

Here,  $S_{L'L}^k$  are the structure constants (2.39) [159]  $S_{L'L}^k = g_{L'L}\Sigma_{\lambda\mu}^k$ , where  $\lambda = l' + l$ ,  $\mu = m' - m$ ,

$$g_{L'L} = 2(-1)^{m+1} \left( \frac{(2l' + 1)(2l + 1)(\lambda + \mu)!(\lambda - \mu)!}{(2\lambda + 1)(l' + m')!(l' - m')!(l + m)!(l - m)!} \right)^{1/2},$$

$$\Sigma_{\lambda\mu}^k = \sum_{\mathbf{R} \neq 0} e^{ik\mathbf{R}} \left( \frac{S}{R} \right)^{\lambda+1} \sqrt{4\pi} [i^\lambda Y_{\lambda\mu}(\hat{\mathbf{R}})]^*.$$

In (2.87), the second term is the sum of the tails coming from all remaining atoms of a crystal.

The representation of the MTOs as a product of  $\alpha_l(D)$  and the energy independent orbital is very convenient since it allows the use of  $\chi_L^k(\mathbf{r})$  instead of  $\chi_L^k(\mathbf{r}, D)$ . It may be easily shown that this does not cause a change in the energy eigenvalues, but affects only the normalization of the wave functions.

**Hamiltonian and overlap matrices.** A more general expression of the one-center expansion (2.87) may be written

$$\chi_L^k(\mathbf{r}, D_{l_2}) = \Phi_L(\mathbf{r}, D_{l_2}) - \sum_{L'} \frac{\Phi_{L'}(\mathbf{r}, l')}{\omega_{l'}(D_{l'_2}) - \omega_{l'}(l')} T_{L'L}^k. \quad (2.88)$$

Here,  $D_{l_2} \neq l$  is an arbitrary logarithmic derivative,  $T_{L'L}^k$  is the matrix

$$T_{L'L}^k = \sqrt{\frac{S}{2}} \Phi_{l'}(S, D_{l'_2}) \left\{ -2(2l + 1) \frac{D_{l_2} + l + 1}{D_{l_2} - 1} + S_{L'L}^k \right\} \sqrt{\frac{S}{2}} \Phi_l(S, D_{l_2}). \quad (2.89)$$

Usually, in practical calculations, the value  $D_{l_2} = -l - 1$  is used. In this case, the matrix (2.89) is simplified to

$$T_{L'L}^k = \sqrt{\frac{S}{2}} \Phi_{l'}(S, -l' - 1) S_{L'L}^k \sqrt{\frac{S}{2}} \Phi_l(S, -l - l). \quad (2.90)$$

The Hamiltonian and overlap matrix are then

$$\begin{aligned} H_{L'L}^{\mathbf{k}} = & \langle \chi_{L'}^{\mathbf{k}} | \mathbf{H} | \chi_L^{\mathbf{k}} \rangle = H_{l'}^{(1)} \delta_{L'L} + \sqrt{\frac{S}{2}} \Phi_{l'}(S, -l' - 1) [-(H_{l'}^{(2)} + \\ & + H_l^{(2)}) S_{L'L}^{\mathbf{k}} + \sum_{L''} S_{L'L''}^{\mathbf{k}} H_{L''}^{(3)} S_{L''L}^{\mathbf{k}}] \sqrt{\frac{S}{2}} \Phi_l(S, -l - 1), \end{aligned} \quad (2.91)$$

$$\begin{aligned} O_{L'L}^{\mathbf{k}} = & \langle \chi_{L'}^{\mathbf{k}} | \chi_L^{\mathbf{k}} \rangle = O_{l'}^{(1)} \delta_{L'L} + \sqrt{\frac{S}{2}} \Phi_{l'}(S, -l' - 1) [-(O_{l'}^{(2)} + \\ & + O_l^{(2)}) S_{L'L}^{\mathbf{k}} + \sum_{L''} S_{L'L''}^{\mathbf{k}} O_{l''}^{(3)} S_{L''L}^{\mathbf{k}}] \sqrt{\frac{S}{2}} \Phi_l(S, -l - 1), \end{aligned} \quad (2.92)$$

$$\begin{aligned} O_l^{(1)} &= 1 + \langle \dot{\Phi}_{\nu l}^2 \rangle \omega_l^2(-l - 1), \\ O_l^{(2)} &= \frac{1 + \langle \dot{\Phi}_{\nu l}^2 \rangle \omega_l(-l - 1) \omega_l(l)}{\omega_l(-l - 1) - \omega_l(l)}, \\ O_l^{(3)} &= \frac{1 + \langle \dot{\Phi}_{\nu l}^2 \rangle \omega_l^2(l)}{2S[(2l + 1)\Phi_l(S, l)]^2}, \\ H_l^{(1)} &= \omega_l(-l - 1) + E_{\nu l} O_l^{(1)}, \\ H_l^{(2)} &= \frac{1}{2} + \frac{\omega_l(l)}{\omega_l(-l - 1) - \omega_l(l)} + E_{\nu l} O_l^{(2)}, \\ H_l^{(3)} &= \frac{\omega_l(l)}{2S[(2l + 1)\Phi_l(S, l)]^2} + E_{\nu l} O_l^{(3)}. \end{aligned} \quad (2.93)$$

In these expressions, the components without  $S_{L'L}^{\mathbf{k}}$ , linear or bilinear in  $S_{L'L}^{\mathbf{k}}$  in (2.91)–(2.92) may be considered to be one-, two- and three-center integrals respectively. Equations (2.91)–(2.92) are the fundamental expressions of the LMTO method in the atomic sphere approximation (LMTO-ASA). In fact, it is similar to the linear combination of atomic orbitals (LCAO). However, the latter involves a significant difficulty in the calculation of multi-center integrals. The LMTO-ASA method, when the basis functions, i.e., energy independent MTOs are correctly chosen (they are easily expanded about any center) these integrals are easily calculated through the corresponding matrices.

**The LMTO method.** Now, if we reject the ASA and use instead touching spheres, like in APW and KKR, we shall arrive at the LMTO method.

We separate again the entire space into regions: the potential is spherically symmetric inside the touching, not overlapping, MT spheres with radius  $S$  (region I), while the electron kinetic energy,  $q_0^2 = E - V_c = 0$ , outside the spheres (region II). In this case,

the Hamiltonian and overlap matrix are

$$H_{L'L}^{\mathbf{k}} = \langle \chi_{L'}^{\mathbf{k}} | \mathbf{H} | \chi_L^{\mathbf{k}} \rangle - V_c \langle \tilde{\chi}_{L'}^{\mathbf{k}} | \tilde{\chi}_L^{\mathbf{k}} \rangle + V_c \{ \tilde{\chi}_{L'}^{\mathbf{k}} | \tilde{\chi}_L^{\mathbf{k}} \}, \quad (2.94)$$

$$O_{L'L}^{\mathbf{k}} = \langle \chi_{L'}^{\mathbf{k}} | \chi_L^{\mathbf{k}} \rangle - \langle \tilde{\chi}_{L'}^{\mathbf{k}} | \tilde{\chi}_L^{\mathbf{k}} \rangle + \{ \tilde{\chi}_{L'}^{\mathbf{k}} | \tilde{\chi}_L^{\mathbf{k}} \}, \quad (2.95)$$

where  $\langle \dots \rangle$  indicates the integral over the region I, while  $\{ \dots \}$  over the entire cell of the volume  $\Omega_0$ .  $\tilde{\chi}_L^{\mathbf{k}}$  is the MT orbital for free electrons defined in the entire space.

The exact energy dependent MTO for both regions is given by (2.46). In the Andersen approximation, it may be represented as in (2.86). Thus, the energy independent MTO has the form

$$\chi_L^{\mathbf{k}}(\mathbf{r}, -l - 1) = \begin{cases} \Phi_L(\mathbf{r}, -l - 1) - \Phi_l(S, -l - 1) \\ \times \sum_{L'} S_{L'L}^{\mathbf{k}} \Phi_{L'}(\mathbf{r}, l') \frac{1}{2(2l'+1)\Phi_l(S, l')}, & r \leq S, \\ i^l Y_L(\hat{\mathbf{r}}) \Phi_l(S, -l - 1) \left(\frac{r}{S}\right)^{-l-1} \\ - \Phi_l(S, -l - 1) \sum_{L'} S_{L'L}^{\mathbf{k}} \frac{i^l Y_{L'}(\hat{\mathbf{r}})}{2(2l'+1)} \left(\frac{r}{S}\right)^{l'}, & r > S. \end{cases} \quad (2.96)$$

Let us derive a similar function for free electrons for the condition when  $E = V_c$  over the entire space. This function has the form of (2.96), where, instead of  $\Phi_L$  and  $\Phi_l$ , the corresponding functions for free electrons  $\tilde{\Phi}_L$  and  $\tilde{\Phi}_l$  are substituted. Of course, the function  $\tilde{\chi}_L^{\mathbf{k}}(\mathbf{r}, -l - 1)$  should be equal to  $\chi_L^{\mathbf{k}}(\mathbf{r}, -l - 1)$  in the region II. In order to satisfy this, it is necessary to multiply  $\tilde{\chi}_L^{\mathbf{k}}$  by  $\Phi_l(S, -l - 1)/\tilde{\Phi}_l(S, -l - 1)$  in both regions. Now, we have the basis functions

$$\tilde{\chi}_L^{\mathbf{k}}(\mathbf{r}, -l - 1) = \begin{cases} \tilde{\Phi}_l(\mathbf{r}, -l - 1) \frac{\Phi_l(S, -l - 1)}{\tilde{\Phi}_l(S, -l - 1)} - \Phi_l(S, -l - 1) \\ \times \sum_{L'} S_{L'L}^{\mathbf{k}} \tilde{\Phi}_{L'}(\mathbf{r}, l') \frac{1}{2(2l'+1)\tilde{\Phi}_l(S, l')}, & r \leq S, \\ i^l Y_L(\hat{\mathbf{r}}) \Phi_l(S, -l - 1) \left(\frac{r}{S}\right)^{-l-1} - \Phi_l(S, -l - 1) \\ \times \sum_{L'} S_{L'L}^{\mathbf{k}} i^l Y_{L'}(\hat{\mathbf{r}}) \frac{1}{2(2l'+1)} \left(\frac{r}{S}\right)^{l'}, & r > S. \end{cases} \quad (2.97)$$

The LMTO-ASA method uses the approximation of (2.74),  $D = -l - 1$  is used to simplify the matrix elements. A similar approximation is used, also, for free electrons:

Table 2.1. Potential parameters for free electrons at  $\tilde{D}_{\nu l} = l$  calculated on the MT sphere [159].

Parameter	Value	Parameter	Value
$\tilde{D}_{0l}$	$l$	$\tilde{D}_{0l}$	$3l + 5$
$\tilde{\omega}_l(l)$	0	$\tilde{\omega}_l(-l - 1)$	$\frac{(2l + 1)(2l + 5)}{2S^2}$
$\tilde{\Phi}_l(l)$	$\sqrt{\frac{2l + 3}{S^3}}$	$\tilde{\Phi}_l(-l - 1)$	$\frac{2l + 5}{2\sqrt{(2l + 3)S^3}}$
$\langle \dot{\tilde{\Phi}}_{0l}   \dot{\tilde{\Phi}}_{0l} \rangle$	$\frac{S^4}{(2l + 3)(2l + 5)^2(2l + 7)}$		

$$\tilde{\Phi}_l(r, -l - 1) = \tilde{\Phi}_{l\nu}(r) + \tilde{\omega}_l(-l - 1)\dot{\tilde{\Phi}}_{l\nu}(r). \quad (2.98)$$

We write the radial Schrödinger equation and replace  $(V - E)$  by the infinitesimal  $-\varepsilon$  to obtain the wave function in the form  $\left(\frac{r}{S}\right)^l \left[1 + \left(\frac{r}{S}\right)^2 a_1 + \dots\right]$ . We get

$$\tilde{\Phi}_l(r, \varepsilon) = \sqrt{\frac{2l + 3}{S^3}} \left[1 + \frac{\varepsilon S^2}{2(2l + 5)}\right] \left(\frac{r}{S}\right)^l \left[1 - \frac{\varepsilon S^2}{2(2l + 3)} \left(\frac{r}{S}\right)^2\right], \quad (2.99)$$

$$\tilde{\Phi}_{l\nu}(r) = \sqrt{\frac{2l + 3}{S^3}} \left(\frac{r}{S}\right)^l, \quad \tilde{\Phi}_l(S, -l - 1) = \sqrt{\frac{2l + 3}{S^3}} \frac{2l + 5}{2(2l + 3)}. \quad (2.100)$$

$$\dot{\tilde{\Phi}}_{l\nu}(r) = \sqrt{\frac{2l + 3}{S^3}} \left(\frac{r}{S}\right)^l \left[\frac{S^2}{2(2l + 5)} - \frac{S^2}{2(2l + 3)} \left(\frac{r}{S}\right)^2\right]. \quad (2.101)$$

Using the reciprocal lattice representation one can write

$$\hat{\chi}_L^k(\mathbf{r}, -l - 1) = \Phi_l(S, -l - 1) \sum_{\mathbf{G}_n} e^{i\mathbf{k}_n \cdot \mathbf{r}} F_L(\hat{\mathbf{k}}_n), \quad (2.102)$$

where  $\mathbf{k}_n = \mathbf{k} + \mathbf{G}_n$ ,  $\mathbf{G}_n$  are the reciprocal lattice vectors,

$$F_L(\mathbf{k}_n) = (2l + 1)(2l + 3) \frac{4\pi S^3}{\Omega_0} \frac{j_{l+1}(k_n S)}{(k_n S)^3} Y_L(\hat{\mathbf{k}}_n). \quad (2.103)$$

Thus, the integral over the cell acquires the form

$$\{\tilde{\chi}_{L'}^{\mathbf{k}} \mid \tilde{\chi}_L^{\mathbf{k}}\} = \Omega_0 \Phi_{l'}(S, -l' - 1) \Phi_l(S, -l - 1) \sum_{\mathbf{G}_n} F_{L'}^*(\mathbf{k}_n) F_L(\mathbf{k}_n). \quad (2.104)$$

Now, we finally obtain for the matrix elements of the LMTO method

$$H_{L'L}^{\mathbf{k}} = \bar{H}_{L'L}^{\mathbf{k}} + V_c \{\tilde{\chi}_{L'}^{\mathbf{k}} \mid \tilde{\chi}_L^{\mathbf{k}}\}, \quad (2.105)$$

$$O_{L'L}^{\mathbf{k}} = \bar{O}_{L'L}^{\mathbf{k}} + \{\tilde{\chi}_{L'}^{\mathbf{k}} \mid \tilde{\chi}_L^{\mathbf{k}}\}. \quad (2.106)$$

$\bar{H}_{L'L}^{\mathbf{k}}$  and  $\bar{O}_{L'L}^{\mathbf{k}}$  are given in (2.91)–(2.92), in which the following matrix parameters are used to replace  $H_L^{(i)}$  and  $O_L^{(i)}$ :

$$\bar{H}_L^{(i)} = H_L^{(i)} - V_c C_L^{(i)}, \quad \bar{O}_L^{(i)} = O_L^{(i)} - C_L^{(i)}, \quad i = 1, 2, 3. \quad (2.107)$$

Here,

$$\begin{aligned} C_L^{(1)} &= \left[ 1 + \frac{(2l+1)^2}{4(2l+3)(2l+7)} \right] \frac{4(2l+3)S^3 \Phi_l^2(s, -l-1)}{(2l+5)^2}, \\ C_L^{(2)} &= \frac{2S^2}{2(2l+1)(2l+5)}, \quad C_L^{(3)} = \frac{S^2}{2(2l+1)^2(2l+3)}. \end{aligned} \quad (2.108)$$

**Valence electron wave function in a crystal.** The valence electron wave function in a crystal can be represented as a one-center expansion

$$\Psi_{\mathbf{k}}(\mathbf{r}, E_j) = \sum_{L'L} [\Phi_{vL}(\mathbf{r}) \pi_{LL'}^{\mathbf{k}} + \dot{\Phi}_{vL}(\mathbf{r}) \Omega_{LL'}^{\mathbf{k}}] C_{L'}^{\mathbf{k}}(E_j, -l - 1), \quad (2.109)$$

where

$$\pi_{LL'}^{\mathbf{k}} = \delta_{LL'} - T_{LL'}^{\mathbf{k}} / [\omega_l(D_l) - \omega_l(l)], \quad (2.110)$$

$$\Omega_{LL'}^{\mathbf{k}} = \omega_l(-l - 1) \delta_{LL'} - T_{LL'}^{\mathbf{k}} \frac{\omega_l(l)}{\omega_l(-l - 1) - \omega_l(l)}. \quad (2.111)$$

For our purposes, we can represent the valence electron wave function in a crystal

by writing the expression, in explicit form, for the energy independent MTO:

$$\begin{aligned}\Psi_{\mathbf{k}}(\mathbf{r}, E_j) &= \sum_L C_L^{\mathbf{k}}(E_j, -l-1) \chi_L^{\mathbf{k}}(\mathbf{r}, -l-1) \\ &= \sum_L \Phi_L(\mathbf{r}, -l-1) C_L^{\mathbf{k}}(E_j, -l-1) \\ &\quad - \sum_{L'L} \Phi_L(\mathbf{r}, l) S_{L'L}^{\mathbf{k}} \frac{\Phi_{L'}(S, -l'-1)}{2(2l+1)\Phi_l(S, l)} C_{L'}^{\mathbf{k}}(E_j, -l'-1).\end{aligned}\quad (2.112)$$

This expression for  $\Psi_{\mathbf{k}}(\mathbf{r}, E_j)$  is accurate up to terms in  $(E - E_v)$  [159], while the energy eigenvalues  $E_j(\mathbf{k})$  and the eigenvectors  $C_L^{\mathbf{k}}(E_j)$  are determined to within  $(E - E_v)^3$ . To be able to write  $\Psi_{\mathbf{k}}(\mathbf{r}, E_j)$  also to within  $(E - E_v)^3$  we have to use the exact MT orbitals (2.46) which depend on energy. Then the electron wave function in a crystal is

$$\Psi_{\mathbf{k}}(\mathbf{r}, E_j) = \sum_L \chi_L^{\mathbf{k}}(\mathbf{r}, D) \frac{(2l+1)\Phi_l(S, -l-1)}{(l-D)\Phi_l(S, D)} C_L^{\mathbf{k}}(E_j). \quad (2.113)$$

We rewrite (2.113) to get the explicit form of the MT orbital (2.46):

$$\begin{aligned}\Psi_{\mathbf{k}}(\mathbf{r}, E_j) &= \sum_L \left\{ \Phi_L(\mathbf{r}, D) \frac{(2l+1)\Phi_l(S, -l-1)}{(l-D)\Phi_l(S, D)} C_L^{\mathbf{k}}(E_j) - \frac{\Phi_L(\mathbf{r}, l)}{2(2l+1)\Phi_l(S, l)} \right. \\ &\quad \times \left. \sum_{L'} \Phi_{L'}(S, -l'-1) \left[ S_{L'L}^{\mathbf{k}} - 2(2l+1)\delta_{L'L} \frac{D+l+1}{l-D} \right] C_{L'}^{\mathbf{k}}(E_j) \right\}. \quad (2.114)\end{aligned}$$

In this form, the wave function is accurate to within  $(E - E_v)^3$ .

**Relativistic LMTO Method.** Andersen [159] derived the relativistic generalization of the LMTO method based on the Pauli Hamiltonian. Here, we proceed with a more general approach based on the solution of the Dirac equation [158]. The trial function with arbitrary logarithmic derivative  $D$  is written similarly to (2.74)

$$\Phi_K(D, \mathbf{r}) = i^l \begin{pmatrix} g_\kappa(D, r) & \chi_K(\hat{\mathbf{r}}) \\ if_\kappa(D, r) & \chi_{\bar{K}}(\hat{\mathbf{r}}) \end{pmatrix}, \quad (2.115)$$

$$g_\kappa(D, r) = g_{\nu\kappa}(r) + \omega_\kappa(D)\dot{g}_{\nu\kappa}(r),$$

$$f_\kappa(D, r) = f_{\nu\kappa}(r) + \omega_\kappa(D)\dot{f}_{\nu\kappa}(r), \quad (2.116)$$

where  $K = (\kappa, \mu)$ ,  $\bar{K} = (-\kappa, \mu)$ ,  $\dot{g}_{\nu\kappa} \equiv \partial g_\kappa / \partial E \mid_{E=E_\nu}$ . The radial wave functions are normalized according to the condition (2.55), the logarithmic derivative is defined in (2.56),  $\chi_K(\hat{\mathbf{r}})$  are the spin-angular functions defined in (2.53),

$$\omega_\kappa(D) = -\frac{g_{\nu\kappa}}{\dot{g}_{\nu\kappa}} \frac{D - D_{\nu\kappa}}{D - D_{\dot{\nu}\kappa}}, \quad (2.117)$$

$$g_\kappa(D) = g_{\nu\kappa} \frac{D_{\nu\kappa} - D_{\dot{\nu}\kappa}}{D - D_{\dot{\nu}\kappa}}. \quad (2.118)$$

The matrix elements of the Hamiltonian and overlap matrix in the basis set (2.115) for a single sphere of radius  $S$  have the form

$$\langle \Phi_{K'}(D', \mathbf{r}) \mid \mathbf{H} - E_{\nu\kappa} \mid \Phi_K(D, \mathbf{r}) \rangle = \omega_\kappa(D) \delta_{K'K}, \quad (2.119)$$

$$\langle \Phi_{K'}(D', \mathbf{r}) \mid \Phi_K(D, \mathbf{r}) \rangle = [1 + \omega_\kappa(D) \omega_\kappa(D') \langle |\dot{\Phi}_{\nu\kappa}|^2 \rangle] \delta_{K'K}. \quad (2.120)$$

We use the expression

$$\int_{\Omega} d\mathbf{r} X^\dagger \alpha \mathbf{p} Y = \int_{\Omega} d\mathbf{r} (Y^\dagger \alpha \cdot \mathbf{p} X)^* - i \int_{\partial\Omega} d\hat{\mathbf{r}} X^\dagger \alpha \mathbf{n} Y, \quad (2.121)$$

where  $\mathbf{n}$  is the vector normal to the surface, and obtain an important relation

$$S g_{\nu\kappa} \dot{g}_{\nu\kappa} (D_{\nu\kappa} - D_{\dot{\nu}\kappa}) = 1. \quad (2.122)$$

Let us select two arbitrary logarithmic derivatives  $D_1$  and  $D_2$  as the parameters. It can be easily shown that the following relation holds:

$$S g_\kappa(D_1) g_\kappa(D_2) = -\frac{\omega_\kappa(D_2) - \omega_\kappa(D_1)}{D_2 - D_1} \quad (2.123)$$

and, for the case  $D_1 = -l - 1$ ,  $D_2 = l$ ,

$$(2l+1)Sg_\kappa(-l-1)g_\kappa(l) = \omega_\kappa(-l-1) - \omega_\kappa(l). \quad (2.124)$$

The energy independent RMTD in the region outside the atomic sphere is a solution of the Dirac equation for  $E = V_c = 0$  possessing the logarithmic derivative  $\tilde{D}_\kappa(0) = \tilde{D}_{0\kappa}$  (the tilde indicates free electrons). The radial solutions of the Dirac equations for free electrons, singular and regular at the origin, have the forms of (2.61)–(2.62), respectively.

The RMTD  $\chi_K(\mathbf{r})$ , inside the central sphere equals  $\Phi_K(\mathbf{r}, -l-1)$ . In the interstitial region it is proportional to  $\tilde{\Phi}_K(\mathbf{r}, -l-1)$  and, inside any other sphere shifted by the lattice translation vector  $\mathbf{R}$ , it is the linear combination of  $\Phi_K(\mathbf{r}-\mathbf{R}, l')$  with coefficients that ensure continuity and differentiability of the RMTD over the entire space.

The Bloch sum of orbitals

$$\chi_K^{\mathbf{k}}(\mathbf{r}) = \sum_{\mathbf{R}} e^{i\mathbf{k}\cdot\mathbf{R}} \chi_K(\mathbf{r} - \mathbf{R}) \quad (2.125)$$

can be written using the generalized theorem of additivity (2.66) as

$$\chi_K^{\mathbf{k}}(\mathbf{r}) = \Phi_K(\mathbf{r}, -l-1) - \sum_{K'} \frac{\Phi_{K'}(\mathbf{r}, l')}{2(2l'+1)} \frac{g_\kappa(S, -l-1)}{g_{\kappa'}(S, l')} S_{K'K}^{\mathbf{k}}, \quad (2.126)$$

where  $S_{K'K}^{\mathbf{k}}$  is defined in (2.70). The second term in this expression is the sum of the RMTD tails coming from all other atoms in the crystal.

We use (2.124) to rewrite (2.126)

$$\begin{aligned} \chi_K^{\mathbf{k}}(\mathbf{r}) &= \Phi_K(\mathbf{r}, -l-1) - \sum_{K'} \frac{\Phi_{K'}(\mathbf{r}, l')}{\omega_{\kappa'}(-l'-1) - \omega_{\kappa'}(l')} \\ &\quad \times \sqrt{\frac{S}{2}} g_{\kappa'}(S, -l'-1) S_{K'K}^{\mathbf{k}} \sqrt{\frac{S}{2}} g_\kappa(S, -l-1). \end{aligned} \quad (2.127)$$

Taking (2.119)–(2.120) into account, we obtain the relativistic LMTO-ASA elements of the Hamiltonian and overlap matrices

$$H_{K'K}^{\mathbf{k}} = \langle \chi_{K'}^{\mathbf{k}} | \mathbf{H} | \chi_K^{\mathbf{k}} \rangle = H_{\kappa'}^{(1)} \delta_{K'K} - \sqrt{\frac{S}{2}} g_{\kappa'}(S, -l' - 1) \quad (2.128)$$

$$\begin{aligned} & \times \left[ \left( H_{\kappa'}^{(2)} + H_{\kappa}^{(2)} \right) S_{K'K}^{\mathbf{k}} - \sum_{K''} S_{K'K''}^{\mathbf{k}} H_{\kappa''}^{(3)} S_{K''K}^{\mathbf{k}} \right] \sqrt{\frac{S}{2}} g_{\kappa}(S, -l - 1), \\ O_{K'K}^{\mathbf{k}} &= \langle \chi_{K'}^{\mathbf{k}} | \chi_K^{\mathbf{k}} \rangle = O_{\kappa}^{(1)} \delta_{K'K} - \sqrt{\frac{S}{2}} g_{\kappa'}(S, -l' - 1) \end{aligned} \quad (2.129)$$

$$\begin{aligned} & \times \left[ \left( O_{\kappa'}^{(2)} + O_{\kappa}^{(2)} \right) S_{K'K}^{\mathbf{k}} - \sum_{K''} S_{K'K''}^{\mathbf{k}} O_{\kappa''}^{(3)} S_{K''K}^{\mathbf{k}} \right] \sqrt{\frac{S}{2}} g_{\kappa}(S, -l - 1), \end{aligned}$$

where

$$\begin{aligned} O_{\kappa}^{(1)} &= 1 + \langle |\dot{\Phi}_{\nu\kappa}|^2 \rangle \omega_{\kappa}^2(-l - 1), \\ O_{\kappa}^{(2)} &= \frac{1 + \langle |\dot{\Phi}_{\nu\kappa}|^2 \rangle \omega_{\kappa}(-l - 1) \omega_{\kappa}(l)}{\omega_{\kappa}(-l - 1) - \omega_{\kappa}(l)}, \\ O_{\kappa}^{(3)} &= \frac{1 + \langle |\dot{\Phi}_{\nu\kappa}|^2 \rangle \omega_{\kappa}^2(l)}{2S[(2l + 1)g_{\kappa}(l)]^2}, \\ H_{\kappa}^{(1)} &= \omega_{\kappa}(-l - 1) + E_{\nu\kappa} O_{\kappa}^{(1)}, \\ H_{\kappa}^{(2)} &= \frac{1}{2} + \frac{\omega_{\kappa}(l)}{\omega_{\kappa}(-l - 1) - \omega_{\kappa}(l)} + E_{\nu\kappa} O_{\kappa}^{(2)}, \\ H_{\kappa}^{(3)} &= \frac{\omega_{\kappa}(l)}{2S[(2l + 1)g_{\kappa}(l)]^2} + E_{\nu\kappa} O_{\kappa}^{(3)}. \end{aligned} \quad (2.130)$$

In (2.128)–(2.129), the terms with the indices 1, 2, and 3 are one-, two-, and three-center integrals, respectively.

The direct procedure to calculate the combined corrections is the following. The integrals over the unit cell  $\{\chi_{K'}^{\mathbf{k}}, \dots, \chi_K^{\mathbf{k}}\}$  are represented as the sum of two terms: integrals over the MT sphere  $\langle \chi_{K'}^{\mathbf{k}}, \dots, \chi_K^{\mathbf{k}} \rangle$  and those over the interstitial region. Note that in the latter, the orbitals  $\chi_K^{\mathbf{k}}(\mathbf{r})$  can be replaced with those for free electrons  $\tilde{\chi}_K^{\mathbf{k}}(\mathbf{r})$ :

$$O_{K'K}^{\mathbf{k}} = \langle \chi_{K'}^{\mathbf{k}} | \chi_K^{\mathbf{k}} \rangle + \langle \tilde{\chi}_{K'}^{\mathbf{k}} | \tilde{\chi}_K^{\mathbf{k}} \rangle - \langle \tilde{\chi}_{K'}^{\mathbf{k}} | \chi_K^{\mathbf{k}} \rangle. \quad (2.131)$$

Since in the interstitial region  $\mathbf{H}\tilde{\chi}_K^{\mathbf{k}}(\mathbf{r}) = V_c\tilde{\chi}_K^{\mathbf{k}}(\mathbf{r})$ , then

$$H_{K'K}^{\mathbf{k}} = \langle \chi_{K'}^{\mathbf{k}} | \mathbf{H} | \chi_K^{\mathbf{k}} \rangle + V_c \{ \tilde{\chi}_{K'}^{\mathbf{k}} | \tilde{\chi}_K^{\mathbf{k}} \} - V_c \langle \tilde{\chi}_{K'}^{\mathbf{k}} | \tilde{\chi}_K^{\mathbf{k}} \rangle. \quad (2.132)$$

The RMTD for free electrons  $\tilde{\chi}_K^{\mathbf{k}}(\mathbf{r})$  must match with  $\chi_K^{\mathbf{k}}(\mathbf{r})$  in the interstitial region. The behavior of  $\tilde{\chi}_K^{\mathbf{k}}(\mathbf{r})$  inside spheres is in principle arbitrary. However, for the integral  $\langle \tilde{\chi}_{K'}^{\mathbf{k}} | \tilde{\chi}_K^{\mathbf{k}} \rangle$  to have the form of (2.129), the orbital  $\tilde{\chi}_K^{\mathbf{k}}(\mathbf{r})$  must be similar to (2.115)–(2.116). The radial part of this normalized RMTD of free electrons for  $V(r) = 0$ ,  $E_v = 0$ , to within the  $1/c^2$  terms is

$$\tilde{\Phi}_{0\kappa}^N(r, D) = \tilde{\Phi}_{0\kappa}^N(r) + \tilde{\omega}_{\kappa}(D) \dot{\tilde{\Phi}}_{0\kappa}^N(r), \quad (2.133)$$

where

$$\begin{aligned} \tilde{\Phi}_{0\kappa}^N(r) &= \tilde{\Phi}_{\kappa}(r, l) \sqrt{\frac{2l+3}{S^3}}, \\ \dot{\tilde{\Phi}}_{0\kappa}^N(r) &= \sqrt{\frac{2l+3}{S^3}} \left( \frac{r}{S} \right)^l \left( \begin{array}{l} \frac{S^2}{2} \left[ \frac{-1}{2l+3} \left( \frac{r}{S} \right)^2 + \frac{1}{2l+5} \right] \\ i \frac{S}{c} \frac{-1}{2+l-\kappa} \left[ \frac{r}{S} - \frac{\kappa+l+1}{2l+5} \left( \frac{r}{S} \right)^{-1} \right] \end{array} \right). \end{aligned} \quad (2.134)$$

Therefore, the RMTD for free electrons are

$$\tilde{\chi}_K(\mathbf{r}) = \begin{cases} \frac{g_{\kappa}(-l-1)}{\tilde{g}_{\kappa}^N(-l-1)} \tilde{\Phi}_K^N(\mathbf{r}, -l-1), & r \leq S \\ g_{\kappa}(-l-1) \tilde{\Phi}_K(\mathbf{r}, -l-1), & r > S. \end{cases} \quad (2.135)$$

Expanding  $j_l(kr)$  at  $k = 0$  as a series, we may obtain the corresponding expressions for potential parameters for free electrons with accuracy of the  $1/c^2$  terms (Table 2.1).

In reciprocal space the Bloch sum of the orbitals of free electrons may be represented similarly to the nonrelativistic case (2.102):

$$\tilde{\chi}_K^{\mathbf{k}}(\mathbf{r}) = g_{\kappa}(S, -l-1) \sum_{\mathbf{G}_n} e^{i\mathbf{k}_n \cdot \mathbf{r}} F_K(\mathbf{k}_n), \quad (2.136)$$

where  $\mathbf{k}_n = \mathbf{k} + \mathbf{G}_n$ ,  $\mathbf{G}_n$  is the reciprocal lattice vector. Then the integral over the cell becomes

$$\{\tilde{\chi}_{K'}^{\mathbf{k}} \mid \tilde{\chi}_K^{\mathbf{k}}\} = \Omega_0 g_{\kappa'}(S, -l' - 1) g_{\kappa}(S, -l - 1) \sum_{\mathbf{G}_n} F_{K'}^{\dagger}(\mathbf{k}_n) F_K(\mathbf{k}_n). \quad (2.137)$$

We restrict ourselves to defining only the upper two larger components of the four-component vector  $F_K(\mathbf{k}_n)$ , since its smaller components are on the order of  $1/c$  and make a contribution into the integral over the cell of  $1/c^2$  order. Then, with the  $1/c^2$ -order terms we have

$$F_K(\mathbf{k}_n) = (2l+1)(2l+3) \frac{4\pi S^3}{\Omega_0} \frac{j_{l+1}(k_n S)}{(k_n S)^3} \begin{pmatrix} \chi_K(\hat{\mathbf{k}}_n) \\ 0 \end{pmatrix}. \quad (2.138)$$

As a result, we obtain for the relativistic LMTO matrix elements

$$H_{K'K}^{\mathbf{k}} = \bar{H}_{K'K}^{\mathbf{k}} + V_c \{\tilde{\chi}_{K'}^{\mathbf{k}} \mid \tilde{\chi}_K^{\mathbf{k}}\}, \quad (2.139)$$

$$O_{K'K}^{\mathbf{k}} = \bar{O}_{K'K}^{\mathbf{k}} + \{\tilde{\chi}_{K'}^{\mathbf{k}} \mid \tilde{\chi}_K^{\mathbf{k}}\}, \quad (2.140)$$

where  $\bar{H}_{K'K}^{\mathbf{k}}$  and  $\bar{O}_{K'K}^{\mathbf{k}}$  are defined in (2.128)–(2.129) and instead of  $H_{\kappa}^{(i)}$  and  $O_{\kappa}^{(i)}$ , the

$$\bar{H}_{\kappa}^{(i)} = H_{\kappa}^{(i)} - V_c C_{\kappa}^{(i)}, \quad \bar{O}_{\kappa}^{(i)} = O_{\kappa}^{(i)} - C_{\kappa}^{(i)}, \quad i = 1, 2, 3, \quad (2.141)$$

$$C_{\kappa}^{(1)} = \left[ 1 + \frac{(2l+1)^2}{4(2l+3)(2l+7)} \right] \frac{4(2l+3)S^3 g_{\kappa}^2(S, -l-1)}{(2l+5)^2},$$

$$C_{\kappa}^{(2)} = \frac{2S^2}{(2l+1)(2l+5)}, \quad C_{\kappa}^{(3)} = \frac{S^2}{2(2l+1)^2(2l+3)} \quad (2.142)$$

are included. Here, like in the nonrelativistic case, the potential parameters and structure constants are calculated on the MT spheres.

**Relativistic Spin-Polarized LMTO Method.** The most widely used approach to treat both relativistic and the effect of the magnetic field on electrons in a solids is based on a scheme proposed by MacDonald and Vosko [160]. In this approach the Dirac

equation for a spin-dependent potential has the form

$$[H(\mathbf{r}) - E]\Psi(\mathbf{r}) = 0, \quad (2.143)$$

$$H(\mathbf{r}) = H^0(\mathbf{r}) + H^M(\mathbf{r}), \quad (2.144)$$

where the Dirac operator  $H^0(\mathbf{r})$ , the spin-dependent part of the Hamiltonian  $H^M(\mathbf{r})$  and an effective magnetic field  $\mathbf{B}(\mathbf{r})$  are

$$H^0(\mathbf{r}) = c\alpha\mathbf{p} + \beta c^2/2 + \mathbf{IV}(\mathbf{r}), \quad (2.145)$$

$$H^M(\mathbf{r}) = \beta\sigma\mathbf{B}(\mathbf{r}), \quad (2.146)$$

$$\mathbf{B}(\mathbf{r}) = \mu_B (\mathbf{B}_{xc}(\mathbf{r}) + \mathbf{B}_{ext}(\mathbf{r})), \quad (2.147)$$

here  $\mathbf{B}_{ext}$  is an external field, the subscript xc refers to the exchange-correlation potential. If we denote the electron and the spin magnetization densities as  $n(\mathbf{r})$  and  $\mathbf{m}(\mathbf{r})$  respectively, then

$$V_{xc}(\mathbf{r}) = \frac{\delta}{\delta n} E_{xc}[n, \mathbf{m}], \quad \mathbf{B}_{xc}(\mathbf{r}) = \frac{\delta}{\delta \mathbf{m}} E_{xc}[n, \mathbf{m}]. \quad (2.148)$$

**Perturbational approach to the spin-polarized relativistic LMTO method.** The easiest way to deal with the full Hamiltonian operator for a spin-dependent potential is to apply perturbation theory or, in other words, take into account the spin-dependent part  $H^M(\mathbf{r})$  of  $H(\mathbf{r})$  only within the variational step [161]. This means that an approximate RLMTO Hamiltonian matrix  $H_{K'K}^{k0}$  is evaluated as for the non-spin-polarized case. The matrix elements  $H_{K'K}^k = \langle \chi_{K'}^k | H^M | \chi_K^k \rangle$  can be easily be expressed in terms of  $H^M(\mathbf{r})$  matrix elements on the functions  $\Phi_K(\mathbf{r}, D)$ . These, in turn, are given by [161]

$$\begin{aligned} \langle \Phi_{K'}(\mathbf{r}, D') | H^M(\mathbf{r}) | \Phi_K(\mathbf{r}, D) \rangle &= G(\kappa', \kappa, \mu) [B\{g_{\kappa'}, g_\kappa\} + \omega_\kappa(D)B\{g_{\kappa'}, \dot{g}_\kappa\}] \\ &+ \omega_{\kappa'}(D')B\{\dot{g}_{\kappa'}, g_\kappa\} + \omega_{\kappa'}(D')\omega_\kappa(D)B\{\dot{g}_{\kappa'}, \dot{g}_\kappa\}] + G(-\kappa', -\kappa, \mu) [B\{f_{\kappa'}, f_\kappa\}] \\ &+ \omega_\kappa(D)B\{f_{\kappa'}, \dot{f}_\kappa\} + \omega_{\kappa'}(D')B\{\dot{f}_{\kappa'}, f_\kappa\} + \omega_{\kappa'}(D')\omega_\kappa(D)B\{\dot{f}_{\kappa'}, \dot{f}_\kappa\}], \end{aligned} \quad (2.149)$$

with

$$G(\kappa', \kappa, \mu) = \delta_{\mu\mu'} \begin{cases} -\mu/(\kappa + 1/2), & \kappa = \kappa', \\ -\sqrt{1 - [\mu/(\kappa + 1/2)]^2}, & \kappa = -\kappa' - 1, \\ 0, & \text{otherwise,} \end{cases} \quad (2.150)$$

$$\langle \chi_{\kappa'}^{\mu'} | \sigma_z | \chi_{\kappa}^{\mu} \rangle = \delta_{\mu\mu'} G(\kappa', \kappa, \mu), \quad (2.151)$$

$$B\{\dot{g}_{\kappa'}, g_{\kappa}\} = \int dr r^2 B(r) \dot{g}_{\kappa'}(r) g_{\kappa}(r), \quad (2.152)$$

and analogously for all other functions  $B\{\alpha_{\kappa'}, \beta_{\kappa}\}$  with  $\alpha, \beta = (g, \dot{g}, f, \dot{f})$ .

Due to the properties of the angular part  $\langle \chi_{\kappa'}^{\mu'}(\hat{\mathbf{r}}) | \sigma_z | \chi_{\kappa}^{\mu}(\hat{\mathbf{r}}) \rangle$ , the matrix elements  $\langle \Phi_{K'}(\mathbf{r}, D') | H^M(\mathbf{r}) | \Phi_K(\mathbf{r}, D) \rangle$  are only diagonal in  $l$  and  $\mu$ , which means, apart from the coupling between functions with  $\kappa = \kappa'$ , there is a coupling for  $\kappa = -\kappa' - 1$ . However, this coupling produces no remarkable difficulties to setting up the matrix  $H_{K'K}^{\mathbf{k}}$ . Because all further steps within this perturbational approach are completely identical to a conventional RLMTO calculations, this method provides a very simple way to perform spin-polarized relativistic band structure calculations. In spite of this approximation used, this scheme nevertheless gives results in very good agreement with the SPR RLMTO one, while being very simple to be implemented [161].

**The SPR LMTO method.** A more accurate solution to the spin-polarized relativistic band structure problem than the perturbational methods will be obtained by setting up the RMTOs by using proper solutions to the single-site Dirac equation for a spin-dependent potential. Spin-polarized fully relativistic LMTO (SPR RLMTO) method have been developed by Ebert [161], Solovyev *et al.* [162] and Krasovskii [163].

As shown by Feder *et al.* [164], Strange *et al.* [165], and also Cortona *et al.* [166], the spin-dependent potential in the Dirac equation results in sets of an infinite number of coupled equations for the radial functions. The usual approximation is to neglect the weak spin-orbit coupling of the order of  $(1/c^2)(1/r)[dB(r)/dr]$  between the states with  $\Delta l = \pm 2$  and  $\Delta j = \pm \frac{1}{2}$  so that the infinite set decomposes into independent sets of four (for  $|\mu| \leq l - 1/2$ ) or two (for  $|\mu| = l + 1/2$ ) coupled equations for each  $l\mu$ . Therefore The solution of Eq. (2.143) inside the atomic sphere is chosen as

$$\Psi(\mathbf{r}, E) = \sum_{l\mu} \sum_{\eta=1,2} c_{l\mu}^{\eta} \varphi_{l\mu}^{s,\eta}(\mathbf{r}, E), \quad (2.153)$$

where the partial solution takes the form

$$\varphi_{l\mu}^{s,\eta}(\mathbf{r}, E) = i^l \begin{pmatrix} g_{l\mu}^{s,\eta}(r, E) & \chi_{l,\mu}^s(\hat{\mathbf{r}}) \\ if_{l\mu}^{s,\eta}(r, E) & \chi_{l+2s,\mu}^{-s}(\hat{\mathbf{r}}) \end{pmatrix}. \quad (2.154)$$

Similar to the conventional RLMTO method, the expression for the wave function with an arbitrary logarithmic derivative  $D$  reads [163]

$$\Phi_{l\mu}^s(\mathbf{r}, D) = \sum_{\eta} \left[ a_{l\mu}^{\eta}(D) \varphi_{l\mu}^{s,\eta}(\mathbf{r}, E_{\nu}) + b_{l\mu}^{\eta}(D) \dot{\varphi}_{l\mu}^{s,\eta}(\mathbf{r}, E_{\nu}) \right]. \quad (2.155)$$

In principle, one could go on completely analogously to the conventional LMTO method to construct SPR MTOs. This approach results, however, in a very inconvenient form of the Hamiltonian and overlap matrix elements. An alternative way [161] to set up the MTOs is simply to augmented smoothly the interstitial solutions  $n_{l\mu}(\mathbf{r})$  within the central cell by  $\Phi_{l\mu}(\mathbf{r}, -l - 1)$  and in all other spheres by linear combinations of  $\Phi_{l\mu}(\mathbf{r}, l')$ . These functions  $\Phi_{l\mu}(\mathbf{r}, D)$  are now found by smoothly matching linear combinations of the solutions  $\varphi_{l\mu}^{s,\eta}(\mathbf{r}, E_{\nu})$  and their energy derivatives  $\dot{\varphi}_{l\mu}^{s,\eta}(\mathbf{r}, E_{\nu})$  to the Neumann solutions  $n_{l\mu}(\mathbf{r})$  for  $D = -l - 1$  and to the Bessel solutions  $j_{l\mu}(\mathbf{r})$  for  $D = l$ , respectively. The corresponding matching conditions for  $r = S$  then reads

$$\sum_{\eta} \left[ a_{l\mu}^{\eta}(D) g_{l\mu}^{1/2,\eta}(S) + b_{l\mu}^{\eta}(D) \dot{g}_{l\mu}^{1/2,\eta}(S) \right] = 1, \quad (2.156)$$

$$\sum_{\eta} \left[ a_{l\mu}^{\eta}(D) f_{l\mu}^{1/2,\eta}(S) + b_{l\mu}^{\eta}(D) \dot{f}_{l\mu}^{1/2,\eta}(S) \right] = \begin{cases} -\frac{2l+1}{cS}, & D = -l - 1, \\ 0, & D = l, \end{cases} \quad (2.157)$$

$$\sum_{\eta} \left[ a_{l\mu}^{\eta}(D) g_{l\mu}^{-1/2,\eta}(S) + b_{l\mu}^{\eta}(D) \dot{g}_{l\mu}^{-1/2,\eta}(S) \right] = 1, \quad (2.158)$$

$$\sum_{\eta} \left[ a_{l\mu}^{\eta}(D) f_{l\mu}^{-1/2,\eta}(S) + b_{l\mu}^{\eta}(D) \dot{f}_{l\mu}^{-1/2,\eta}(S) \right] = \begin{cases} 0, & D = -l - 1, \\ -\frac{2l+1}{cS}, & D = l. \end{cases} \quad (2.159)$$

The Dirac equation (2.143) for free-electron states with  $E - V - \beta\sigma\mathbf{B} = 0$  has two singular and regular at the origin bispinor solutions [158, 163], respectively

$$\tilde{\phi}_{l\mu}^s(\mathbf{r}, -l - 1) = i^l \begin{pmatrix} (\frac{r}{S})^{-l-1} & \chi_{l,\mu}^s(\hat{\mathbf{r}}) \\ -i\Theta(s)\frac{2l+1}{cS}(\frac{r}{S})^{-l-2} & \chi_{l+2s,\mu}^{-s}(\hat{\mathbf{r}}) \end{pmatrix} \quad (2.160)$$

$$\tilde{\phi}_{l\mu}^s(\mathbf{r}, l) = i^l \begin{pmatrix} (\frac{r}{S})^l & \chi_{l,\mu}^s(\hat{\mathbf{r}}) \\ i\Theta(-s)\frac{2l+1}{cS}(\frac{r}{S})^{l-1} & \chi_{l+2s,\mu}^{-s}(\hat{\mathbf{r}}) \end{pmatrix}. \quad (2.161)$$

The one-center expansion of the Bloch sum of the free-electron relativistic muffin-tin orbitals  $\tilde{\chi}_{l\mu}^s(\mathbf{r})$  ( $s = \pm 1/2$ ) in the sphere at  $\mathbf{q}'$  has the form

$$\tilde{\chi}_{L\mu}^{\mathbf{k},s}(\mathbf{r} - \mathbf{q}') = \delta_{\mathbf{q}'\mathbf{q}} \tilde{\phi}_{L\mu}^s(\mathbf{r} - \mathbf{q}, -l - 1) - \sum_{l's'\mu'} \frac{\tilde{\phi}_{L'\mu'}^{s'}(\mathbf{r} - \mathbf{q}', l')}{2(2l' + 1)} \sqrt{\frac{S_q}{S_{q'}}} S_{L',s',\mu';L,s,\mu}^{\mathbf{k}}.$$

Here the subscript  $L$  denotes the set  $\{\mathbf{q}, l\}$ ,  $\mathbf{q}$  is the position of an atom in the unit cell. The relativistic structure constants  $S_{L',s',\mu';L,s,\mu}^{\mathbf{k}}$  are related to the non-relativistic constants by the expression (2.70).

Inside a sphere at the site  $\mathbf{q}$  the SPR MTO  $\chi_{L\mu}(\mathbf{r})$  is now given by  $\Phi_{L\mu}^s(\mathbf{r} - \mathbf{q}, -l - 1)$ . In the interstitial region we assume that  $E - V - \beta\sigma\mathbf{B} = 0$ , and the expression for the SPR LMTO is  $\tilde{\chi}_{L\mu}^s(\mathbf{r} - \mathbf{q}, -l - 1)$ . In a sphere centered at a different lattice site  $\mathbf{R} + \mathbf{q}'$  it is a linear combination of the functions  $\Phi_{L'\mu'}^{s'}(\mathbf{r} - \mathbf{R} - \mathbf{q}', l')$  such that the SPR LMTO  $\chi_{L\mu}(\mathbf{r})$  is continuous everywhere in the crystal. Then a one-center expansion of the Bloch sum of the SPR LMTOs can be constructed. In the sphere at  $\mathbf{q}'$  it reads

$$\chi_{L\mu}^{\mathbf{k},s}(\mathbf{r} - \mathbf{q}') = \delta_{\mathbf{q}'\mathbf{q}} \Phi_{L\mu}^s(-l - 1, \mathbf{r} - \mathbf{q}) - \sum_{l's'\mu'} \frac{\Phi_{L'\mu'}^{s'}(\mathbf{r} - \mathbf{q}', l')}{2(2l' + 1)} \sqrt{\frac{S_q}{S_{q'}}} S_{L',s',\mu';L,s,\mu}^{\mathbf{k}}. \quad (2.162)$$

In terms of the basic functions (2.162) the trial function is

$$\Psi_{\mathbf{k}}(\mathbf{r}, E_i^{\mathbf{k}}) = \sum_{L,s,\mu} C_{i,L\mu}^{\mathbf{k},s} \chi_{L\mu}^{\mathbf{k},s}(\mathbf{r}), \quad (2.163)$$

and the variational problem arising from the crystal Dirac equation leads to the generalized eigenvalue problem

$$\sum_{L,s,\mu} \left( H_{L'\mu',L\mu}^{\mathbf{k},s's} - E_i^{\mathbf{k}} O_{L'\mu',L\mu}^{\mathbf{k},s's} \right) C_{i,L\mu}^{\mathbf{k},s} = 0, \quad (2.164)$$

which is linear in energy since the basis functions do not depend on energy. The diagonalization of this set yields eigenvalues  $E_i^{\mathbf{k}}$  and eigenfunctions  $A_{i,L\mu}^{\mathbf{k},s}$  for a given Bloch vector  $\mathbf{k}$  ( $i$  is the band number).

The overlap and Hamiltonian matrixes now read [163]

$$\begin{aligned} O_{L'\mu',L\mu}^{\mathbf{k},s's} &= \sum_{\mathbf{q}''} \langle \chi_{L'\mu'}^{\mathbf{k},s'}(\mathbf{r}) | \chi_{L\mu}^{\mathbf{k},s}(\mathbf{r}) \rangle_{\mathbf{q}'} = \\ &\delta_{L'L} \delta_{\mu'\mu} \delta_{s's} \langle \Phi_{L\mu}^s(-l-1) | \Phi_{L\mu}^s(-l-1) \rangle \\ &- \left[ \frac{\langle \Phi_{L'\mu'}^{s'}(-l'-1) | \Phi_{L'\mu'}^{s'}(l') \rangle}{2(2l'+1)} \sqrt{\frac{S_{\mathbf{q}}}{S_{\mathbf{q}'}}} \right. \\ &+ \left. \frac{\langle \Phi_{L\mu}^s(-l-1) | \Phi_{L\mu}^s(l) \rangle}{2(2l+1)} \sqrt{\frac{S_{\mathbf{q}'}}{S_{\mathbf{q}}}} \right] S_{L',s',\mu';L,s,\mu}^{\mathbf{k}} \\ &+ \sqrt{S_{\mathbf{q}'} S_{\mathbf{q}}} \sum_{L''s''\mu''} \frac{\langle \Phi_{L''\mu''}^{s''}(l'') | \Phi_{L''\mu''}^{s''}(l'') \rangle}{S_{\mathbf{q}''} [2l''(l''+1)]^2} \\ &\times S_{L',s',\mu';L'',s'',\mu'';L,s,\mu}^{\mathbf{k}}, \end{aligned} \quad (2.165)$$

$$H_z^M = \beta \sigma_z B_z(\mathbf{r}), \quad (2.166)$$

$$\begin{aligned} H_{L'\mu',L\mu}^{\mathbf{k},s's} &= \sum_{\mathbf{q}''} \langle \chi_{L'\mu'}^{\mathbf{k},s'}(\mathbf{r}) | H | \chi_{L\mu}^{\mathbf{k},s}(\mathbf{r}) \rangle_{\mathbf{q}''} = \\ &\delta_{L'L} \delta_{\mu'\mu} \{ \delta_{s's} \langle \Phi_{L\mu}^s(-l-1) | H^0 + H_z^M | \Phi_{L\mu}^s(-l-1) \rangle \\ &+ (1 - \delta_{s's}) \langle \Phi_{L\mu}^{-s}(-l-1) | H_z^M | \Phi_{L\mu}^s(-l-1) \rangle \} \\ &- \left[ \frac{\langle \Phi_{L'\mu'}^{s'}(-l'-1) | H^0 + H_z^M | \Phi_{L'\mu'}^{s'}(l') \rangle}{2(2l'+1)} \sqrt{\frac{S_{\mathbf{q}}}{S_{\mathbf{q}'}}} \right. \\ &+ \left. \frac{\langle \Phi_{L\mu}^s(-l-1) | H^0 + H_z^M | \Phi_{L\mu}^s(l) \rangle}{2(2l+1)} \sqrt{\frac{S_{\mathbf{q}'}}{S_{\mathbf{q}}}} + \frac{S_{\mathbf{q}'} S_{\mathbf{q}}}{2} \right] \end{aligned}$$

$$\begin{aligned}
& \times S_{L',s',\mu';L,s,\mu}^{\mathbf{k}} + \frac{\langle \Phi_{L'\mu'}^{s'}(-l'-1) | H_z^M | \Phi_{L'\mu'}^{-s'}(l') \rangle}{2(2l'+1)} \\
& \times \sqrt{\frac{S_{\mathbf{q}}}{S_{\mathbf{q}'}}} S_{L',-s',\mu';L,s,\mu}^{\mathbf{k}} + \frac{\langle \Phi_{L\mu}^s(-l-1) | H_z^M | \Phi_{L\mu}^{-s}(l) \rangle}{2(2l+1)} \times \\
& \left. \times \sqrt{\frac{S_{\mathbf{q}'}}{S_{\mathbf{q}}}} S_{L',s',\mu';L,-s,\mu}^{\mathbf{k}} \right\} \\
& + \sqrt{S_{\mathbf{q}'} S_{\mathbf{q}}} \sum_{L''s''\mu''} \frac{\langle \Phi_{L''\mu''}^{s''}(l'') | H^0 + H_z^M | \Phi_{L''\mu''}^{s''}(l'') \rangle}{S_{\mathbf{q}''} [2l''(l''+1)]^2} \\
& \times \left[ S_{L',s',\mu';L'',s'',\mu''}^{\mathbf{k}} S_{L'',s'',\mu'';L,s,\mu}^{\mathbf{k}} \right. \\
& \left. + \langle \Phi_{L''\mu''}^{-s''}(l'') | H_z^M | \Phi_{L''\mu''}^{s''}(l'') \rangle S_{L',s',\mu';L,s,\mu}^{\mathbf{k}} S_{L'',-s'',\mu'';L,s,\mu}^{\mathbf{k}} \right]. \tag{2.167}
\end{aligned}$$

Radial matrix elements for an arbitrary wave function  $\bar{\varphi}_{L'\mu'}^{s'}(\mathbf{r})$ ,  $\varphi_{L\mu}^s(\mathbf{r})$ , which has the structure of  $\Phi_{l\mu}^s(\mathbf{r}, D)$  (2.155) are [163]

$$\langle \bar{\varphi}_{L'\mu'}^{s'} | \varphi_{L\mu}^s \rangle = \delta_{l'l} \delta_{s's} \delta_{\mu'\mu} \int_0^S dr r^2 (\bar{g}_{l\mu}^s g_{l\mu}^s + \bar{f}_{l\mu}^s f_{l\mu}^s), \tag{2.168}$$

$$\begin{aligned}
\langle \bar{\varphi}_{L'\mu'}^{s'} | H^0 | \varphi_{L\mu}^s \rangle &= \delta_{l'l} \delta_{s's} \delta_{\mu'\mu} \int_0^S dr r^2 \left\{ -\bar{g}_{l\mu}^s \left[ \frac{d}{dr} + \frac{1-\kappa}{r} \right] c f_{l\mu}^s \right. \\
&\quad \left. + c \bar{f}_{l\mu}^s \left[ \frac{d}{dr} + \frac{1+\kappa}{r} \right] g_{l\mu}^s + V(r) \bar{g}_{l\mu}^s g_{l\mu}^s \left[ \frac{V(r)}{c^2} - 1 \right] c^2 \bar{f}_{l\mu}^s f_{l\mu}^s \right\}, \tag{2.169}
\end{aligned}$$

$$\begin{aligned}
\langle \bar{\varphi}_{L'\mu'}^{s'} | \beta \sigma_z B_z | \varphi_{L\mu}^s \rangle &= -\delta_{l'l} \delta_{\mu'\mu} \left\{ \mu \delta_{s's} \int_0^S dr r^2 \left[ \frac{\bar{g}_{l\mu}^s g_{l\mu}^s}{\kappa+1/2} + \right. \right. \\
&\quad \left. \left. + \frac{\bar{f}_{l\mu}^s f_{l\mu}^s}{\kappa-1/2} \right] B_z(r) - (1 - \delta_{s's}) \int_0^S dr r^2 \sqrt{1 - \left( \frac{\mu}{l+1/2} \right)^2} \bar{g}_{l\mu}^{-s} g_{l\mu}^s B_z(r) \right\}, \tag{2.170}
\end{aligned}$$

$$\begin{aligned}
\langle \bar{\varphi}_{L'\mu'}^{s'} | \beta l_z | \varphi_{L\mu}^s \rangle &= \delta_{l'l} \delta_{\mu'\mu} \left\{ \mu \delta_{s's} \int_0^S dr r^2 \text{sgn}(\kappa) \left[ \frac{\kappa+1}{l+1/2} \bar{g}_{l\mu}^s g_{l\mu}^s \right. \right. \\
&\quad \left. \left. + \frac{\kappa-1}{\kappa-1/2} \bar{f}_{l\mu}^s f_{l\mu}^s \right] + \frac{1-\delta_{s's}}{2} \int_0^S dr r^2 \sqrt{1 - \left( \frac{\mu}{l+1/2} \right)^2} \bar{g}_{l\mu}^{-s} g_{l\mu}^s \right\}. \tag{2.171}
\end{aligned}$$

If one neglect  $H_z^M$  (2.166) while solving the set of coupled radial equations then the subscript  $\eta$  in Eq. (2.155) is lost and one comes to the perturbation approach to the SPR linear MTO described in previous section.

Finally, note that SPR LMTO formalism described above has two exact limits: the

non-spin-polarized relativistic limit and the spin-polarized nonrelativistic limit. The coupling between relativistic effects and intrinsic magnetic field is treated in SPR LMTO method “on equal footing” both inside the atomic sphere and in the interstitial region.

### 2.3 Magneto-optical effects

Magneto-optical (MO) effects refer to various changes in the polarization state of light upon interaction with materials possessing a net magnetic moment (spontaneous or induced) including rotation of the plane of linearly polarized light (Faraday, Kerr rotation), and the complementary differential absorption of left and right circularly polarized light (circular dichroism). In the near visible spectral range these effects result from excitation of electrons in the conduction band. Near XA edges, or resonances, magneto-optical effects can be enhanced by transitions from well-defined atomic core levels to transition symmetry selected valence states. There are at least two alternative formalisms for describing resonant X-ray MO properties. One approach uses the classical dielectric tensor [167]. Another one uses the resonant atomic scattering factor including charge and magnetic contributions [168–170]. The equivalence of these two descriptions (within dipole approximation) is demonstrated in Ref. [171]. Using straightforward symmetry considerations it can be shown that all MO phenomena are caused by the symmetry reduction, in comparison to the paramagnetic state, caused by magnetic ordering [172]. Concerning optical properties this symmetry reduction only has consequences when SO coupling is considered in addition. To calculate MO properties one therefore has to account for magnetism and SO coupling at the same time when dealing with the electronic structure of the material considered.

**MO effects in the x-ray region.** In recent years the investigation of magneto-optical effects in the soft x-ray range has gained great importance as a tool for the investigation of magnetic materials. In 1975 the theoretical work of Erskine and Stern showed that the XA could be used to determine the XMCD in transition metals when left- and right-circularly polarized x-ray beams are used [173]. In 1985 Thole *et al.* [174] predicted a strong magnetic dichroism in the  $M_{4,5}$  XA spectra of magnetic rare-earth materials, for which they calculated the temperature and polarization dependence. A year later

this MXD effect was confirmed experimentally by van der Laan *et al.* [175] at the Tb  $M_{4,5}$  XA edge of terbium iron garnet. The next year Schütz *et al.* [176] performed measurements using x-ray transition at the  $K$  edge of iron with circularly polarized x-rays, where the asymmetry in absorption was found to be of the order of  $10^{-4}$ . This was shortly followed by the observation of magnetic EXAFS [177]. A theoretical description for the XMCD at the Fe  $K$  XA edge was given by Ebert *et al.* [178] using a SPR version of multiple scattering theory. In 1990 Chen *et al.* [179] observed a large magnetic dichroism at the  $L_{2,3}$  edge of nickel. Also cobalt and iron showed huge effects, which rapidly brought forward the study of magnetic  $3d$  transition metals, which are of technological interest. Full multiplet calculations for  $3d$  transition metal  $L_{2,3}$  edges by Thole and van der Laan [180] were confirmed by several measurements on transition metal oxides. First considered as a rather exotic technique, MXD has now developed as an important measurement technique for local magnetic moments. XMCD enables a quantitative determination of spin and orbital magnetic moments [181], element-specific imaging of magnetic domains [182] or polarization analysis [183].

Magnetic circular dichroism is first order in  $\mathbf{M}$  (or  $\varepsilon_{xy}$ ) and is given by  $k_+ - k_-$  or  $n_+ - n_-$ , respectively, the later representing the magneto-optical rotation of the plane of polarization (Faraday effect). Magnetic linear dichroism (MLD)  $n_\perp - n_\parallel$  (also known as the Voigt effect) is quadratic in  $\mathbf{M}$ . The Voigt effect is present in both ferromagnets and antiferromagnets, while the first order MO effects in the forward scattering beam are absent with the net magnetization in antiferromagnets.

The alternative consideration of the MO effects is based on the atomic scattering factor  $f(\omega, \mathbf{q})$ , which provides a microscopic description of the interaction of x-ray photons with magnetic ions. For forward scattering ( $\mathbf{q} = 0$ )  $f(\omega) = Z + f'(\omega) + i f''(\omega)$ , where  $Z$  is the atomic number.  $f'(\omega)$  and  $f''(\omega)$  are the anomalous dispersion corrections related to each other by the Kramers-Kronig transformation. The general equivalence of these two formalisms can be seen by noting the one-to-one correspondence of terms describing the same polarization dependence for the same normal modes [171]. For a multicomponent sample they relate to  $n$  and  $k$  through

$$n(\omega) = \frac{2\pi c^2 r_e}{\omega^2} \sum_i Z_i f'_i(\omega) N_i, \quad (2.172)$$

$$k(\omega) = \frac{2\pi c^2 r_e}{\omega^2} \sum_i f''_i(\omega) N_i, \quad (2.173)$$

where the sum is over atomic spheres, each having number density  $N_i$ , and  $r_e$  is the classical electron radius. The x-ray absorption coefficient for polarization  $\lambda$  may be written in terms of  $f''_\lambda(\omega)$  as

$$\mu^\lambda(\omega) = \frac{4\pi r_e c}{\Omega \omega} f''_\lambda(\omega), \quad (2.174)$$

where  $\Omega$  is the atomic volume. x-ray MCD which is the difference in XA for right- and left-circularly polarized photons ( $\mu^+ - \mu^-$ ) can be presented by  $(f''_+ - f''_-)$ . Faraday rotation  $\theta_F(\omega)$  of linear polarization measures MCD in the real part  $f'_\lambda$  of the resonant magnetic x-ray scattering amplitude, i.e. [184]

$$\theta_F(\omega) = \frac{\omega l}{2c} \text{Re}[n_+ - n_-] = \frac{\pi l r_e}{\Omega \omega} (f'_-(\omega) - f'_+(\omega)). \quad (2.175)$$

Finally, the scattering x-ray intensity from an elemental magnet at the Bragg reflection measured in the resonant magnetic x-ray scattering experiments is just the squared modulus of the total scattering amplitude, which is a linear combination of  $(f'_\pm + i f''_\pm, f'_z + i f''_z)$  with the coefficients fully determined by the experimental geometry [185]. Multiple scattering theory is usually used to calculate the resonant magnetic x-ray scattering amplitude  $(f' + i f'')$  [167, 185, 186].

We should mentioned that the general equivalence of the dielectric tensor and scattering factor descriptions holds only in the case of dipole transitions contributing to atomic scattering factor  $f(\omega)$ . Higher-order multipole terms have different polarization dependence [168, 169].

Using straightforward symmetry considerations it can be shown that all magneto-optical phenomena (XMCD, MO Kerr and Faraday effects) is caused by the symmetry reduction, in comparison to the paramagnetic state, caused by magnetic ordering [172].

Concerning the XMCD properties this symmetry reduction only has consequences when SO coupling is considered in addition. To calculate the XMCD properties one has to account for magnetism and SO coupling at the same time when dealing with the electronic structure of the material considered. Theoretical description of magnetic dichroism can be cast into four categories. On the one hand, there are one-particle (ground-state) and many-body (excited-state) theories; on the other hand, there are theories for single atoms and those which take into account the solid state. For atomic one-particle theories we refer to Refs. [187] and [188], for atomic many-particle multiplet theory to Refs. [189–192], for solid many-particle theories to Ref. [193], and for solid one-particle theories (photoelectron diffraction) to Refs. [194–197]. A multiple-scattering approach to XMCD, a solid-state one-particle theory, has been proposed by Ebert *et al.* [198–200] and Tamura *et al.* [201].

Within the one-particle approximation, the absorption coefficient  $\mu$  for incident x-ray of polarization  $\lambda$  and photon energy  $\hbar\omega$  can be determined as the probability of electron transition from an initial core state (with wave function  $\Psi_j$  and energy  $E_j$ ) to a final unoccupied state (with wave function  $\Psi_{n\mathbf{k}}$  and energy  $E_{n\mathbf{k}}$ )

$$\mu_{\lambda j}(\omega) = \sum_{n\mathbf{k}} |\langle \Psi_{n\mathbf{k}} | \mathcal{J}_\lambda | \Psi_j \rangle|^2 \delta(E_{n\mathbf{k}} - E_j - \hbar\omega) \theta(E_{n\mathbf{k}} - E_F). \quad (2.176)$$

The  $\mathcal{J}_\lambda$  is the dipole electron-photon interaction operator  $\mathcal{J}_\lambda = -e\alpha\mathbf{a}_\lambda$ , where  $\mathbf{a}_\lambda$  is the  $\lambda$  polarization unit vector of the photon potential vector [ $\mathbf{a}_\pm = 1/\sqrt{2}(1, \pm i, 0)$ ,  $\mathbf{a}_z = (0, 0, 1)$ ]. Here  $+/-$  denotes, respectively, left and right circular photon polarizations with respect to the magnetization direction in the solid. The matrix elements of the magnetic dipole and electric quadrupole contributions are presented in Ref. [202].

While XMCD is calculated using equation (2.176), the main features can be understood already from a simplified expression for paramagnetic solids. With restriction to electric dipole transitions, keeping the integration only inside the atomic spheres (due to the highly localized core states) and averaging with respect to polarization of the light one obtains the following expression for the absorption coefficient of the core level with  $(l, j)$  quantum numbers [203]:

$$\mu_{lj}^0(\omega) = \sum_{l'j'} \frac{2j+1}{4} \left( \frac{\delta_{l',l+1}\delta_{j',j+1}}{j+1} + \frac{\delta_{l',l-1}\delta_{j',j-1}}{j} + \frac{\delta_{l',l+1}\delta_{j',j}}{j(j+1)(2j+1)} \right) N_{l'j'}(E) C_{lj}^{l'j'}(E), \quad (2.177)$$

where  $N_{l'j'}(E)$  is the partial density of empty states and the  $C_{lj}^{l'j'}(E)$  are the radial matrix elements

$$C_{lj}^{l'j'}(E) = \omega c^2 \left| \int_0^S dr r^2 [(\kappa' - \kappa + 1)g_{c\kappa}(r)f_{\kappa'}(r) + (\kappa' - \kappa - 1)f_{c\kappa}(r)g_{\kappa'}(r)] \right|^2, \quad (2.178)$$

with  $g_{c\kappa}(r)$  ( $f_{c\kappa}(r)$ ) and  $g_\kappa(r)$  ( $f_\kappa(r)$ ) big (small) radial wave functions of the core and valence states respectively.

It is well known that the dipole transition matrix element in (2.177) may be transformed into equivalent forms, and corresponding expressions for the radial matrix elements in the  $\mathbf{r}$ - and  $\nabla V(\mathbf{r})$ -forms can be found in Ref. [203]. Eq. (2.177) allows only transitions with  $\Delta l = \pm 1$ ,  $\Delta j = 0, \pm 1$  (dipole selection rules) which means that the absorption coefficient can be interpreted as a direct measure for the sum of  $(lj)$ -resolved DOS curves weighed by the square of the corresponding radial matrix element (which usually is a smooth function of energy). This simple interpretation is valid for the spin-polarized case [167].

**Sum rules.** Concurrent with the x-ray magnetic circular dichroism experimental developments, some important magneto-optical sum rules have been derived in recent years. Thole and van der Laan [204] developed a sum rule relating the integrated signals over the spin-orbit split core edges of the unpolarized XAS to the expectation value of the ground state spin-orbit operator. Later Thole *et al.* [205] and Carra *et al.* [206] derived sum rules to relate the integrated signals over the spin-orbit split core edges of the circular dichroism to ground state orbital and spin magnetic moments by using an ion model for atoms. In the case of solids the corresponding XMCD sum rules were proposed by Ankudinov and Rehr [207] and Guo [208]. Sum rules for x-ray magnetic

scattering were derived by Luo *et al.* [209].

For the  $L_{2,3}$  edges the  $l_z$  sum rule can be written as

$$\langle l_z \rangle = -\frac{4}{3} n_h \frac{\int_{L_3+L_2} d\omega (\mu_+ - \mu_-)}{\int_{L_3+L_2} d\omega (\mu_+ + \mu_-)}, \quad (2.179)$$

where  $n_h$  is the number of holes in the  $d$  band  $n_h = 10 - n_{3d}$ ,  $\langle l_z \rangle$  is the average of the magnetic quantum number of the orbital angular momentum. The integration is taken over the whole  $2p$  absorption region. The  $s_z$  sum rule is written as

$$\langle s_z \rangle + \frac{7}{2} \langle t_z \rangle = -n_h \frac{6 \int_{L_3} d\omega (\mu_+ - \mu_-) - 4 \int_{L_2} d\omega (\mu_+ - \mu_-)}{\int_{L_3+L_2} d\omega (\mu_+ + \mu_-)}, \quad (2.180)$$

where  $t_z$  is the  $z$  component of the magnetic dipole operator  $\mathbf{t} = \mathbf{s} - 3\mathbf{r}(\mathbf{r} \cdot \mathbf{s})/|\mathbf{r}|^2$  which accounts for the asphericity of the spin moment. It was shown that this term is negligible for cubic systems [167, 200]. The integration  $\int_{L_3}$  ( $\int_{L_2}$ ) is taken only over the  $2p_{3/2}$  ( $2p_{1/2}$ ) absorption region. In these equations, we have replaced the linear polarized spectra  $\mu_0$  by  $[\mu_+(\omega) + \mu_-(\omega)]/2$ .

Because of the significant implications of the sum rules, numerous experimental and theoretical studies aimed at investigating their validity for itinerant magnetic systems have been reported, but with widely different conclusions. The claimed adequacy of the sum rules varies from very good (within 5% agreement) to very poor (up to 50% discrepancy) [181, 205, 206, 210–212]. This lack of a consensus may have several origins. For example, on the theoretical side, it has been demonstrated by circularly polarized  $2p$  resonant photoemission measurements of Ni that both the band structure effects and electron-electron correlations are needed to satisfactorily account for the observed MCD spectra [213]. However, it is extremely difficult to include both of them in a single theoretical framework. Besides, the XA as well as XMCD spectra can be strongly affected (especially for the early transition metals) by the interaction of the excited electron with the created core hole [214].

On the experimental side, the indirect XA techniques, i.e., the total electron and

fluorescence yield methods, are known to suffer from saturation and self-absorption effects that are very difficult to correct for. The total electron yield method can be sensitive to the varying applied magnetic field, changing the electron detecting efficiency, or, equivalently, the sample photocurrent. The fluorescence yield method is insensitive to the applied field, but the yield is intrinsically not proportional to the absorption cross section, because the radiative to non-radiative relative core-hole decay probability depends strongly on the symmetry and spin polarization of the final states [181].

To derive the sum rules a great number of assumptions had to be made [167]. For  $L_{2,3}$ , they are: (1) ignore the exchange splitting for the core levels; (2) replace the interaction operator  $\alpha \cdot \mathbf{a}_\lambda$  in Eq. (2.176) by  $\nabla \cdot \mathbf{a}_\lambda$ ; (3) ignore the asphericity of the core states; (4) ignore  $p \rightarrow s$  transitions; (5) ignore the difference of  $d_{3/2}$  and  $d_{5/2}$  radial wave functions; (6) ignore of the inter-atomic hybridization, which is reflected on the nontreatment of any energy dependence of the radial matrix elements. The three last points are the most important. The problem of the ignoring of the  $p \rightarrow s$  transitions was considered by Wu and Freeman [212] in the case of pure Fe, Co, Ni and their surfaces. They demonstrate that the application of the spin sum rule results in an error up to 52% for the Ni(001) surface. On the other hand, the orbital sum rule is affected much less.

**Background intensity.** In order to simplify the comparison of the theoretical x-ray isotropic absorption  $L_{2,3}$  spectra to the experimental ones the background intensity which affects the high energy part of the spectra and is caused by different kind of inelastic scattering of the electron promoted to the conduction band above Fermi level due to XA (scattering on potentials of surrounding atoms, defects etc.) should be taken into account. Such kind of scattering is very difficult to describe theoretically from first principles, only few processes have adequate theoretical models. For the background spectra calculations the model proposed by Richtmyer *et al.* [215] has been used. The absorption coefficient for the background intensity is

$$\mu(\omega) = \frac{C\Gamma_c}{2\pi} \int_{E_{cf_0}}^{\infty} \frac{dE_{cf}}{(\Gamma_c/2)^2 + (\hbar\omega - E_{cf})^2}, \quad (2.181)$$

where  $E_{cf} = E_c - E_f$ ,  $E_c$  and  $\Gamma_c$  are the energy and the lifetimes broadening of the

Table 2.2. The widths  $\Gamma_c$  of core levels, in eV, taken from [216].

	O	V	Mn	Fe	Co	Zn	Ca
$K$	0.18	0.96	1.11	1.19	1.28	1.62	0.77
$L_2$	–	0.78	0.97	1.14	1.13	1.06	0.21
$L_3$	–	0.28	0.36	0.41	0.47	0.68	0.21

used in calculations are summarized in Table 2.2. It should be mentioned that the background intensity depends on type of the spectrum and atomic number, particularly it is rather small for the  $L_{2,3}$  spectra of  $3d$  metals.

**Details of calculations.** The calculations presented in this work were performed using SPR LMTO discussed above for the experimentally observed lattice constants. Results for DMSs (see Chapter 3) have been obtained using the Perdew-Wang [217, 218] and results for A-site ordered perovskites (see Chapter 4) – using GGA in the version of Perdew, Burke and Ernzerhof (PBE) [219, 220] parameterizations of the exchange-correlation potential. Brillouin zone (BZ) integrations were performed using the improved tetrahedron method [221] and charge self-consistently was obtained on a grid of  $\mathbf{k}$  points in the irreducible part of the BZ. To improve the potential we included additional interstitial “empty” spheres. The basis consisted of  $s, p, d, f$  for TM,  $s, p, d$  for O and Ca, and  $s, p$  for empty spheres’ LMTOs.

XA and XMCD spectra have been calculated taking into account the exchange splitting of core levels. The finite lifetime of a core hole is accounted for by folding the spectra with a Lorentzian of width  $\Gamma_c$  (see Table 2.2). The finite apparatus resolution of the spectrometer was accounted for by a Gaussian of width 0.6 eV.

The LDA fails to describe correctly strongly localized  $d$  state. To include the electron-electron correlations into the consideration, the “relativistic” generalization of the rotationally invariant version of the LSDA+ $U$  method [222] which takes into account SO coupling so that the occupation matrix of localized electrons becomes non-diagonal in spin indices is used.

The screened Coulomb  $U$  and exchange Hund coupling  $J$  integrals enter the LSDA+ $U$

core hole,  $E_f$  is the energy of empty continuum level,  $E_{f_0}$  is the energy of the lowest unoccupied continuum level, and  $C$  is a normalization constant which has been used as an adjustable parameter.  $\Gamma_c$  values

energy functional as an external parameters and have to be determined independently. These parameters can be determined from supercell LSDA calculations using Slater's transition state technique [148, 223], from constrained LSDA calculations (cLSDA) [223–227] or from the constrained random-phase approximation (cRPA) scheme [228]. Subsequently, a combined cLSDA and cRPA method was also proposed [229]. It is known, that the cRPA method underestimates values of  $U$  in some cases [230]. On the other hand, the cLSDA method produces too large values of  $U$  [231]. Therefore, in these calculations the Hubbard  $U$  is treated as an external parameter and varied it from 3.0 eV to 7.0 eV to achieve the best agreement with the experiment. The calculations themselves can be considered as *ab initio* calculations with one additional parameter  $U$ .

In the XA process, an electron is promoted from a core level to an unoccupied state, leaving a hole at core level. As a result, the electronic structure at this site differs from that of the ground state. In order to reproduce the experimental spectra, self-consistent calculations should be carried out including a core hole. In this study the core-hole effect is fully taken into account in the self-consistent iterations by removing an electron at the core orbital using the supercell approximation. The core state of the target atom in the ground state provides the initial state for the spectral calculations. The final states are the conduction band states obtained separately by calculations in which one of the core electrons of the target atom is placed at the lowest conduction band. The interaction and the screening of the electron-hole pair are fully accounted for by the self-consistent iterations of the final state Kohn-Sham equations. Such an approach simulates the experimental situation and allows for the symmetry breaking of the system in a natural way, and self-consistently describes the charge redistribution induced by the core hole. A similar approximation has been used by several authors [232–237]. The size of the supercell is important, and ultimately it should be large enough to inhibit interaction between excited atoms in neighboring supercells.

# CHAPTER 3

## ELECTRONIC BAND STRUCTURE AND X-RAY SPECTRA IN ZnO-BASED DILUTED MAGNETIC SEMICONDUCTORS

The original results discussed in this Chapter are published in [1–3].

### 3.1 Crystal structure and details of calculations

The elements in the  $(\text{Zn},\text{T})\text{O}$  compound have nominal atomic structures  $[\text{Ar}]3d^{10}4s^2$  for Zn,  $[\text{Ar}]3d^n s^2$  for T, where  $n = 3, 5, 6$ , and 7 for T = V, Mn, Fe, and Co respectively, and  $[\text{He}]2s^22p^4$  for O. The most stable and therefore most common position of T in the ZnO host lattice is on the Zn site where its two 4s electrons can participate in crystal bonding in much the same way as the two Zn 4s electrons.

The calculations of the electronic structure of the  $(\text{Zn}_{1-x}\text{T}_x)\text{O}$  DMSs have been performed for  $3a \times 3a \times 1c$ ,  $3a \times 3a \times 2c$ , and  $4a \times 4a \times 1c$  supercells of the wurtzite-type ZnO unit cell with the experimentally observed lattice constants  $a = 9.588 \text{ \AA}$ ,  $c = 5.16 \text{ \AA}$  [238]. The supercell is configured using the simple trigonal  $P3m1$  (No. 156)

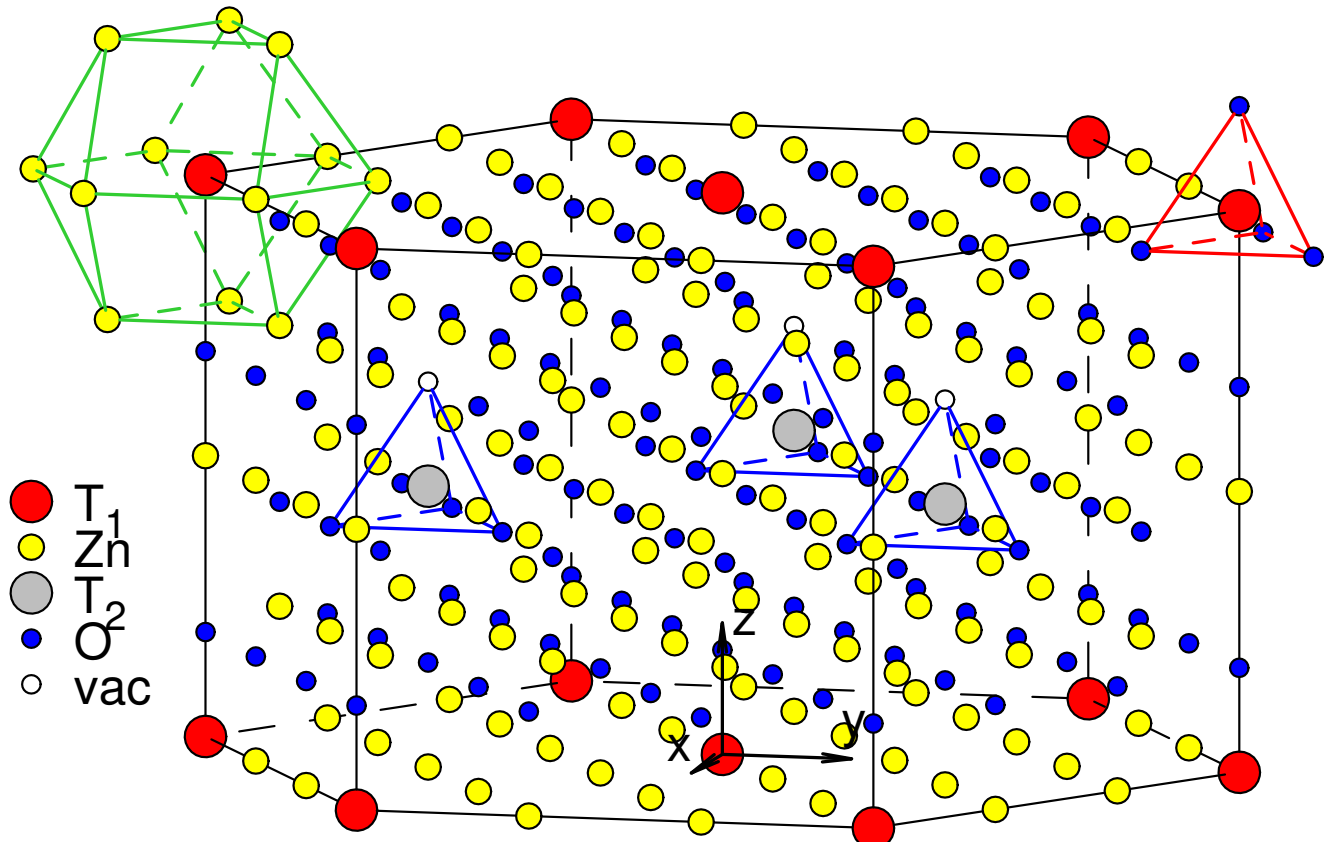


Figure 3.1. The representation of the  $3a \times 3a \times 2c$  supercell of the ZnO unit cell with some of the Zn ions replaced by T ones. The oxygen vacancy in close vicinity of the  $\text{T}_2$  atom is shown with the open circle.

space group, with one or two of the Zn ions are replaced by T and give the supercell compositions for  $x = 1/18, 1/32$ , and  $1/36$ . The substitutional positions are illustrated in Fig. 3.1 for a 72-atom ZnO unit cell containing two substitutional T atoms for  $x = 1/18$ . The T atom has four O nearest neighbors: three O atoms at a distance of  $1.956 \text{ \AA}$  and one O atom at  $1.962 \text{ \AA}$ . These O atoms form the tetrahedra. The second-neighbor shell consists of 12 Zn atoms: six at  $3.183 \text{ \AA}$  and six at  $3.209 \text{ \AA}$ . They form the polyhedrons.

As stated in section 1.1 a ZnO crystal always accommodates a lot of different native defects, with experiments have been inconclusive as to which of these is the predominant defect. That's why the atomic positions of Zn and O atoms as well as dopants T have been optimized using the Vienna *ab initio* simulation package (VASP) [219, 220, 239, 240]. In these calculations either lattice parameters or atomic positions have been relaxed. Results show that the electronic band structure and x-ray spectra depend mostly on atomic position of dopants T and its neighbors as shown in the Fig. 3.1. Additional calculations are required if one takes possible vacancies into account.

The LDA fails to describe correctly localized  $d$  states in ZnO, LDA+ $U$  approach is required to treat the strong  $d$ - $d$  correlations. For the exchange integral  $J$  the value of  $0.92 \text{ eV}$  estimated from constrained LSDA calculations is used. The application of the LSDA+ $U$  method leads to a shift of the Zn  $d$  states downward in energy and makes the band gap larger. Band gap equals  $E_g = 2.12 \text{ eV}$  within the LSDA+ $U$  for the  $U = 6 \text{ eV}$  vs.  $0.8 \text{ eV}$  within the LSDA in pure ZnO. The same effect can be achieved treating the Zn  $d$  states as core states. In LMTO calculations both approaches have been used and no significant difference in the XA and XMCD spectra has been found. The T  $d$  states were treated within the LSDA as well as the LSDA+ $U$  approach. Usually the failure of the LSDA method generally occurs toward the right end of the  $3d$  transition-metal series while for T = V, Mn, and Fe which are in the middle of  $3d$  series, no strong correlation interaction would be expected [241]. That's why the application of various  $U$  values within the LSDA+ $U$  approach for the description of the XA and XMCD spectra shows that the agreement between the theoretically calculated and experimental spectra does not significantly change in comparison with the LSDA method. It is worth to keep the LSDA approach in the calculations since in this case the first principle calculations are

performed without any adjustable parameter like the Hubbard  $U$  and the T  $d$  states are treated within the LSDA.

### 3.2 (Zn,V)O

**Energy band structure.** Figure 3.2 presents total and partial DOS for a 36-atom ZnO wurtzite unit cell containing one V substitution ( $x = 1/18$ ) in the LSDA. The O  $s$  states are located mostly between  $-21.0$  eV to  $-19.7$  eV below the  $E_F$  and the  $p$  states of the O are found between  $-9.6$  eV to  $-3.0$  eV. The spin splitting of the O  $p$  states is quite small.

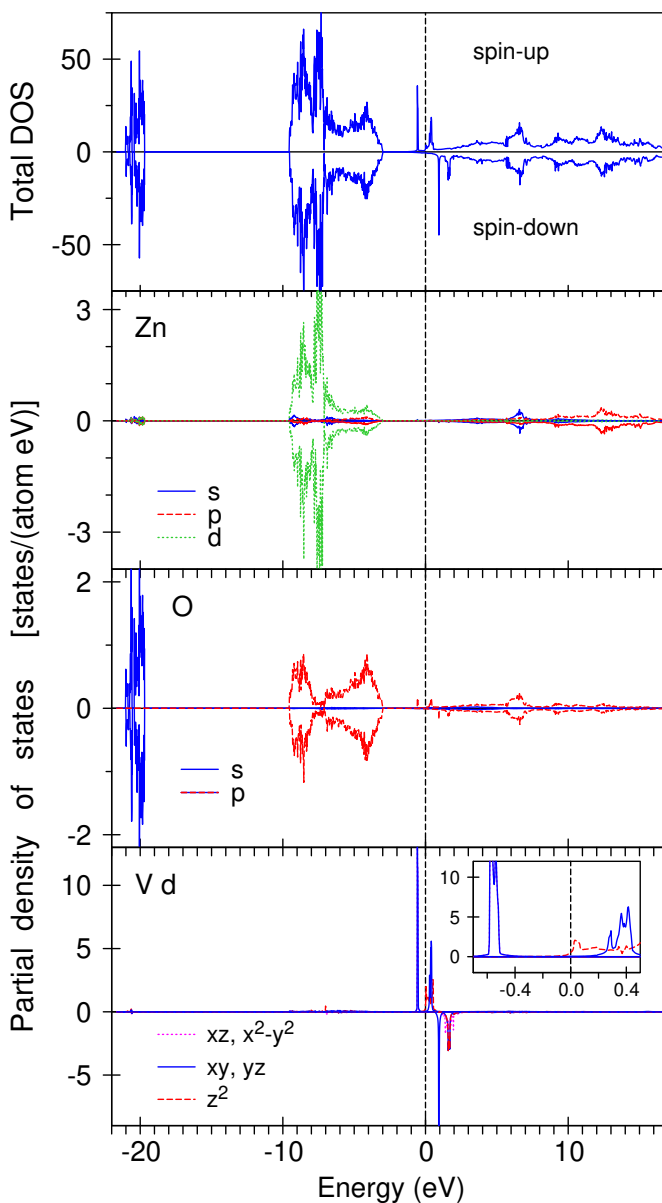


Figure 3.2. The LSDA total [in states/(cell eV)] and partial [in states/(atom eV)] DOS, calculated by the LMTO method, for the O, Zn and substituted V ions in  $\text{Zn}_{0.94}\text{V}_{0.06}\text{O}$  [3]. The insert is a blowup of the V  $d$  partial DOS close to the  $E_F$ . The  $E_F$  is at zero.

Zn  $d$  states occupy the energy interval between  $-9.6$  eV and  $-3.0$  eV and hybridize strongly with the O  $p$  states.

The majority-spin V  $d_{3z^2-1}$  structure is found in close vicinity to the  $E_F$  between  $-0.2$  eV and  $0.7$  eV (see the insert in the bottom panel of Fig. 3.2). Very strong and narrow peaks of the majority-spin V bonding  $d_{xy}$ , and  $d_{yz}$  states are located between  $-0.4$  eV and  $-0.8$  eV below the  $E_F$ . The corresponding anti-bonding states are at  $0.2$  eV to  $0.6$  eV. Narrow peaks of the  $d_{xy}$ , and  $d_{yz}$  symmetry occur in the minority-spin channel at around  $1$  eV above the  $E_F$ . The energy interval of  $1.4$  eV to  $2.2$  eV above the  $E_F$  is occupied by the  $d_{xz}$ ,  $d_{x^2-y^2}$ , and  $d_{3z^2-1}$  states with minority-spin.

The electronic and magnetic structures of the  $(\text{Zn}_{1-x}\text{V}_x)\text{O}$  DMSs with two of the Zn ions replaced by V have been investigated. The supercell calculations

have been performed for the compositions  $x = 2/18$ ,  $2/32$ , and  $2/36$ . As a result, the V atoms substituted at different Zn sites show very little selectivity of site occupancy. Different geometries with FM and AFM configurations are found to be energetically nearly degenerate, the difference in the total energies between FM and AFM solutions is found to be less than 3 meV/f.u. Still in most cases the FM solutions are lower in total energy in comparison with the AFM ones. However, for fully relaxed lattice it is found that the AFM ordering has lower total energy in comparison with the FM one.

**The XA and XMCD spectra at the V  $L_{2,3}$  edges.** The XA and XMCD spectra of the dilute magnetic semiconductor (Zn,V)O at the V  $L_{2,3}$  edges have been investigated by Ishida *et al.* [68]. They found that  $\sim 90\%$  of the V ions were presumably strongly

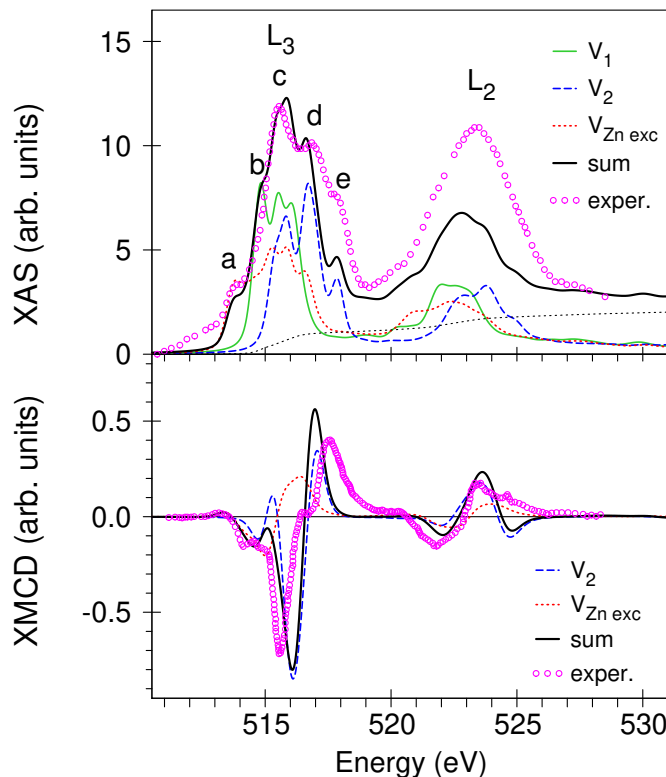


Figure 3.3. Top panel: theoretically calculated (thick full line) [3] and experimentally measured [68] (circles) XA spectra of (Zn,V)O at the V  $L_{2,3}$  edges. Full line presents the XA spectrum without any additional defects. Dashed and dotted lines present the XA spectra with the oxygen vacancy (the contribution of the  $V_2$  sublattice as in Fig. 3.1) and Zn excess atom, respectively. Bottom panel: theoretically calculated (thick full line) and experimentally measured [68] (circles) XMCD spectra at the V  $L_{2,3}$  edges. Dashed and dotted lines present the XMCD spectra with the oxygen vacancy and Zn excess atom, respectively.

AFM coupled, and the FM component was below the detection limit of XMCD.

Since the real structure and chemical composition of (Zn,V)O is not known, the numerous calculations fitting XA and XMCD spectra to the experimental results have been performed. The fitting parameters were positions of V atoms, Zn excess atoms, various oxygen vacancies and the magnetic order of V atoms. The best fit is shown in Fig. 3.3, which presents the calculated XA as well as XMCD spectra of the (Zn,V)O DMS at the V  $L_{2,3}$  edges compared with the experimental data [68]. In this model, V atoms substitute cations and are AFM-ordered. Thereby, they are positioned at the largest possible  $V_1-V_2$  distance of 5.53 Å. Relevant XMCD signal occurs only in the presence of an oxygen va-

cancy located in the first neighborhood of the second  $V_2$  atom along  $z$  direction. Adding Zn excess atoms also improves the agreement between the theory and the experiment.

The XA spectrum at the  $V L_3$  edge is rather complicated and consists of two major peaks  $c$  and  $d$  at 515.6 eV and 517 eV, respectively, with two additional low energy shoulders  $a$  and  $b$  at 513.8 eV and 514.6 eV and a high energy shoulder at 518 eV. As can be seen from the top panel of Fig. 3.3 the calculations for the ideal crystal structure with two substituted AFM ordered  $V_1$  atoms (full curve) provide the XA intensity only at peak  $c$  and shoulder  $b$ . The full explanation of the spectra is only possible by taking crystal imperfections into account.

The influence of two types of crystal defects on the XA and XMCD spectra, namely, oxygen deficiency and Zn excess is investigated. The oxygen vacancy strongly affects the shape of the XA spectra. As can be seen from Fig. 3.3 (top panel) the XA from the  $V_2$  atoms with the oxygen vacancy (dashed line) contributes to the major peak  $c$  and significantly determines the intensity of the peak  $d$  and the high energy shoulder  $e$ . To investigate the Zn excess on the XMCD spectra an extra Zn atom is placed into the tetrahedral interstitial position T 2.1916 Å apart from the  $V_2$  site. The XA from the  $V_{Zn\text{exc}}$  atoms with the Zn excess atom (dotted line) contributes to the major peaks  $c$  and  $d$  as well as to both the low energy shoulders  $a$  and  $b$ . Therefore, the simulation including oxygen deficiency and Zn excess reproduces the shape of the  $V L_3$  XA spectrum quite well (see thick curve in top panel of Fig. 3.3). The lattice relaxation is found to be very important in the presence of the oxygen vacancy as well as the Zn excess.

The XMCD spectrum at the  $V L_3$  edge is also rather complicated and consists of a small positive peak at 513.8 eV, a negative fine structure at 514.6 eV, a negative major peak at 515.6 eV, a positive major peak at 517.7 eV with a shoulder at 516.4 eV. The  $V L_2$  XMCD spectrum consists of two major fine structures, a negative peak at 521.8 eV and a positive one at 523.3 eV. The theory is not able to reproduce the shape and relative intensity of the  $V L_{2,3}$  XMCD spectra for the FM ordered V atoms, with one and two V substitutions per unit cell. The theory strongly overestimates (from one to two orders of magnitude) the dichroism signal and produces non-adequate shape of the spectra. On the other hand, the theory produces an almost vanishing XMCD signal for the AFM

ordering of vanadium substitutional V ions for the ideal crystal structure without any kind of defects due to cancellation of the XMCD spectra with opposite spin directions.

One has to mention that any shift from the AFM to the FM order will increase the intensity of the final XMCD spectra due to the reduction of the compensation of the XMCD spectra from V ions with opposite spin directions. Such a shift may be caused by an applied external magnetic field or different kinds of defects and imperfections in the lattice. The experimental measurements have been performed in an external magnetic field of 7 T [68]. The calculations with an external magnetic field applied along the  $z$  direction, indeed, show an increase in spectra intensity but only by approximately 10% to 20%. It has been found that only the defects cause a significant difference. As can be seen from the lower panel of Fig. 3.3 the theoretically calculated XMCD spectra with an oxygen vacancy (dashed line) resemble the experimental spectra quite well. An additional consideration of the Zn excess atoms (dotted curve) leads to further improvement between the theory and the experiment.

One should mention that we obtain better agreement between the theory and the experiment in the XA rather than in the XMCD spectra. The energy split between the two major peaks of the V  $L_3$  XMCD spectrum was found to be smaller than the experimentally measured one. The reproduction of the shape of the V  $L_{2,3}$  XMCD spectra is a quite difficult task because the rather weak final XMCD signal is derived from two large signals occurring from the V atoms with opposite spin directions. In this case, one has to take into account different crystal defects in a particular sample with quite precise relative concentration. However, the type and concentration of possible defects in the sample is not always well known. On the other hand, the extreme sensitivity of the XMCD signal may be considered as a useful tool to reveal the details of the composition, by modeling numerically different types of defects and comparing the theoretically calculated XMCD spectra with the experimentally measured ones.

### 3.3 (Zn,Mn)O

**Energy band structure.** Figure 3.4 presents the total and the partial DOSs for a 72-atom ZnO unit cell containing one Mn substitution ( $x = 0.03$ ) in the LSDA. The O  $s$  states

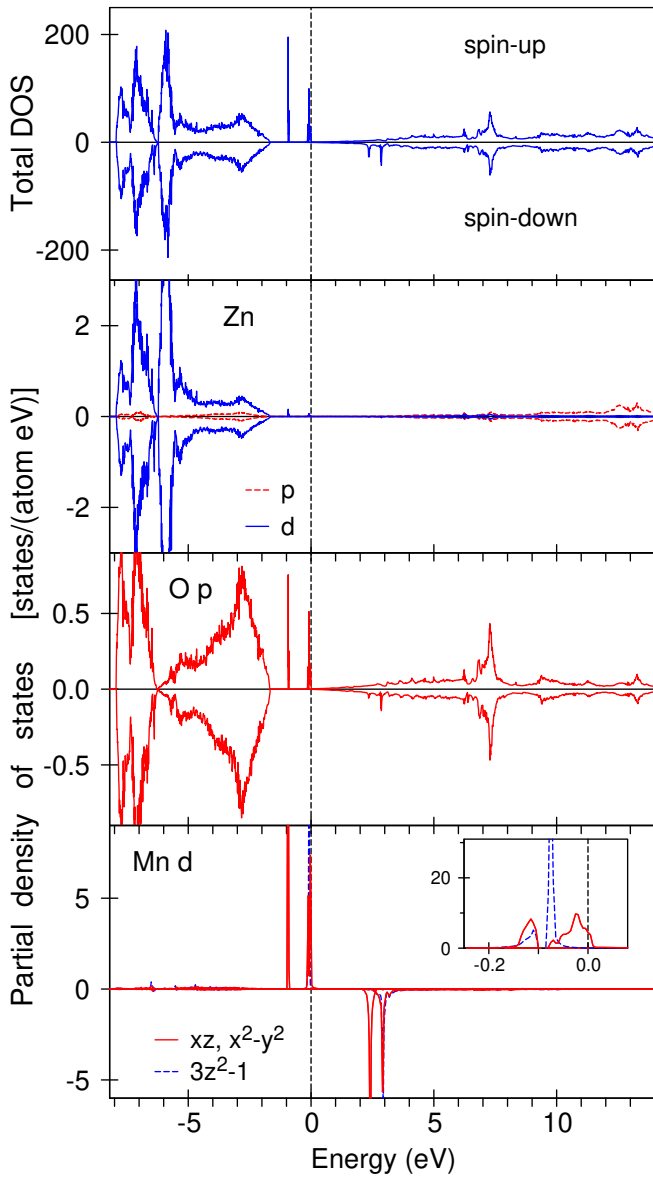


Figure 3.4. The LSDA total [in states/(cell eV)] and partial [in states/(atom eV)] DOS for the O, Zn and substituted Mn ions in  $(\text{Zn}_{0.97}\text{Mn}_{0.03})\text{O}$ . The insert is a blowup of the Mn  $d$  partial DOS close to the  $E_{\text{F}}$ . The  $E_{\text{F}}$  is at zero.

range of the valence bands and antibonding states above the valence bands. The crystal field at the Mn site ( $C_{3v}$  point symmetry) causes the splitting of Mn  $d$  states into a singlet  $a_1$  ( $d_{3z^2-1}$ ) and two doublets  $e$  ( $d_{yz}$  and  $d_{xz}$ ) and  $e_1$  ( $d_{xy}$  and  $d_{x^2-y^2}$ ). A very strong and narrow peak associated with the majority-spin Mn  $d_{3z^2-1}$  structure is found in close vicinity to the  $E_{\text{F}}$  around  $-0.08$  eV between the two peaks of the  $d_{xz}$  and the  $d_{x^2-y^2}$  states (see the insert in the bottom panel of Fig. 3.4). Another narrow peak associated with the majority-spin Mn bonding  $d_{xz}$  and  $d_{x^2-y^2}$  states is located between  $-0.90$  eV and  $-0.96$  eV below the  $E_{\text{F}}$ . Peaks of  $d_{xz}$  and  $d_{x^2-y^2}$  states in the minority-spin channel

(not shown) are located mostly between  $-19.7$  eV to  $-18.7$  eV below the  $E_{\text{F}}$ , and the  $p$  states of the O are found between  $-8.0$  eV to  $-1.7$  eV. The spin splitting of the O  $p$  states is quite small. Zn  $d$  states occupy the energy interval between  $-8.0$  eV and  $-1.8$  eV and hybridize strongly with the O  $p$  states.

The Mn  $3d$  shell is approximately half filled, and the exchange splitting between the centers of gravity of the occupied majority and unoccupied minority subbands is about  $3.5$  eV. The Mn  $3d$  impurity states are mainly located in the upper part of the ZnO gap and well hybridize with the O  $2p$  conduction band, which gives the solution a metallic character. The structure of the impurity bands is similar to that of GaN-based DMSs [242] because of their having the same symmetry at the substitutional tetrahedral site: there are bonding states in the energy

lie at 2.3 eV to 2.6 eV and at 2.85 eV to 3.0 eV above the  $E_F$  respectively. The energy range from 2.9 eV to 2.95 eV above the  $E_F$  is occupied by the  $d_{3z^2-1}$  minority-spin states.

The magnetic moment in the  $(\text{Zn}_{0.97}\text{Mn}_{0.03})\text{O}$  unit cell is  $4.800 \mu_B$ . The band structure calculations yield a spin magnetic moment of  $4.180 \mu_B$  for the Mn atoms. The induced spin magnetic moments at the O first neighbor sites are of  $0.060 \mu_B$  and  $-0.057 \mu_B$ , for longer and shorter distant O atoms, respectively. Twelve Zn ions in the second neighbor shell couple ferromagnetically to the substituted Mn ion with spin magnetic moments from  $0.005 \mu_B$  to  $0.007 \mu_B$ . The orbital moments at the Zn and the O sites are small, with the largest one being at the O first neighbor sites ( $0.005 \mu_B$ ). The orbital magnetic moment at the Mn site is  $-0.084 \mu_B$  and is antiparallel to the spin one.

**XMCD spectra at the Mn  $L_{2,3}$  edges.** The XA and the XMCD spectra at the Mn  $K$  and  $L_{2,3}$  edges in Mn-doped ZnO have been measured by several groups [69–77].

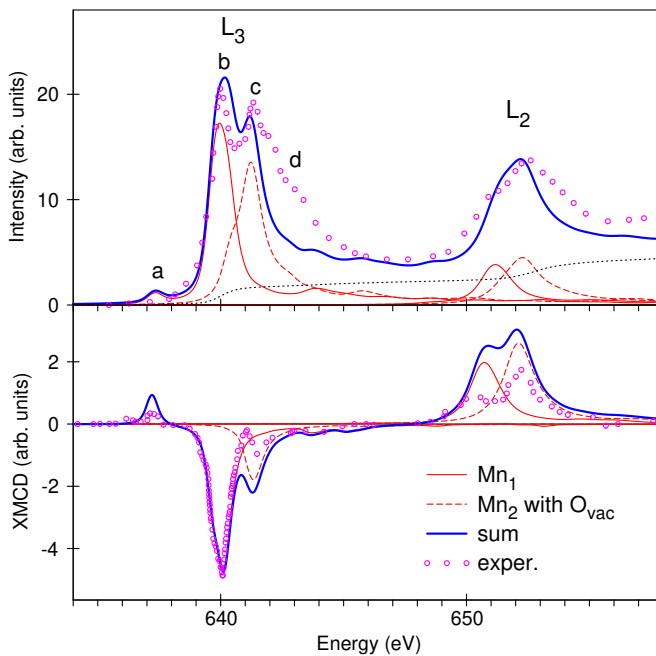


Figure 3.5. Top panel: Experimental [74] (circles) and theoretically calculated XA spectrum (thick full blue line) in  $(\text{Zn}_{0.97}\text{Mn}_{0.03})\text{O}$  at the Mn  $L_{2,3}$  edges. The full red line presents the XA spectrum without any additional defects. Dashed red line present the XA spectra with the oxygen vacancy (the contribution of the  $\text{Mn}_2$  sublattice as in Fig. 3.1). Bottom panel: theoretically calculated (thick full blue line) and experimentally measured [74] (circles) XMCD spectra at the Mn  $L_{2,3}$  edges. The full red line presents the XMCD spectrum without any additional defects. The dashed red lines present the XMCD spectrum with the oxygen vacancy.

Figure 3.5 presents experimental XA and XMCD spectra [74] for  $(\text{Zn},\text{Mn})\text{O}$  at the Mn  $L_{2,3}$  edges, together with the spectra calculated in the LSDA. The XA spectrum at the Mn  $L_3$  edge is rather complicated and consists of two major peaks  $b$  and  $c$  at 640 eV and 641.5 eV, respectively, with two additional fine structures: a low-energy small peak  $a$  at around 637.5 eV and a high energy shoulder at 643 eV. We found that the small low-energy peak  $a$  of the Mn  $L_3$  XA spectrum could be attributed to transitions from the  $2p$  core level to the empty majority-spin  $d$  states of  $d_{xz}$  and  $d_{x^2-y^2}$  symmetry (see the insert in the lower panel of Fig. 3.4).

As the valence changes from  $\text{Mn}^{2+}$

to Mn<sup>3+</sup> or Mn<sup>4+</sup>, the XA spectrum at  $L_3$ -edge is well known to show a shift toward higher energy, and the spectral shape changes with the number of 3d electrons [149]. The first major peak *b* at 640 eV is attributed to the Mn<sup>2+</sup> states and the second higher energy major feature *c* – to the mixed valence states of Mn<sup>2+</sup> with Mn<sup>3+</sup>/Mn<sup>4+</sup> [74]. The theoretical calculations support such a suggestion.

As can be seen from the top panel of Fig. 3.5, the calculations for the ideal crystal structure with one substituted Mn<sub>Zn</sub> atoms (full red curve) reproduce the XA intensity only at peaks *a* and *b*. The full explanation of the spectra is only possible by taking crystal imperfections into account. The influence of two types of crystal defects on the XA and the XMCD spectra, namely oxygen deficiencies and Zn excess, is investigated by creation an oxygen vacancy in the first neighborhood of the second Mn<sub>2</sub> atom along the *z* direction (see Fig. 3.1). The oxygen vacancy has four nearest neighbor atoms: three Zn atoms at the distance of 1.956 Å and one Mn at 1.962 Å. The lattice relaxation is found to be very important in the presence of the oxygen vacancy as well as the Zn excess. The relaxation causes a shift of the Mn<sub>2</sub> atom and the three Zn atoms toward the vacant site by 0.18 Å and 0.22 Å, respectively. The oxygen vacancy with lattice relaxation taken into account strongly affects the shape of the XA spectra. As can be seen from Fig. 3.5 (top panel), the XA from the Mn<sub>2</sub> atoms with the oxygen vacancy (red dashed line) contributes to the major peak *c* and the high energy shoulder *d*. Therefore, the calculations including the oxygen deficiency reproduce the shape of the Mn  $L_3$  XA spectrum quite well (see the thick blue curve in the top panel of Fig. 3.5). The valence in the Mn<sub>2</sub> site, with the oxygen deficiency taking into account, is not 3+ as was suggested in [74], but a non-integral one, approximately 2.6+ according to current estimates.

To investigate the Zn excess on the XMCD spectra, an extra Zn atom is placed into the tetrahedral interstitial position T, 1.694 Å away from the Mn<sub>2</sub> site. After lattice relaxation, the distance is increased by 0.38 Å. The Zn excess is found to have less influence upon the DOSs than the oxygen deficiency due to the smaller Mn *d* – Zn *d* hybridization in comparison with the corresponding O 2p – Mn *d* hybridization. The Zn excess only slightly increases the intensity of the high energy shoulder *d* of the  $L_3$  XA spectrum (not shown). However, the theoretical calculations still underestimates

the intensity of the high-energy fine structure  $d$ . This might indicate that an additional satellite structure may appear due to many-body effects and might affect the high energy tail of the Co  $L_3$  XA spectrum. This question needs an additional investigation.

The theoretically calculated Mn  $L_{2,3}$  XMCD spectra are in good agreement with the experiment (Fig. 3.5), although the calculated magnetic dichroism is somewhat too high at the  $L_2$  edge. The main reason for this discrepancy is the core-hole effect. This effect is not taken into account by the present electronic structure calculations, and it is likely to lead to the observed discrepancy [243]. The theory also overestimates the intensity of the fine structure near the high energy major peak  $c$  at around 641.5 eV.

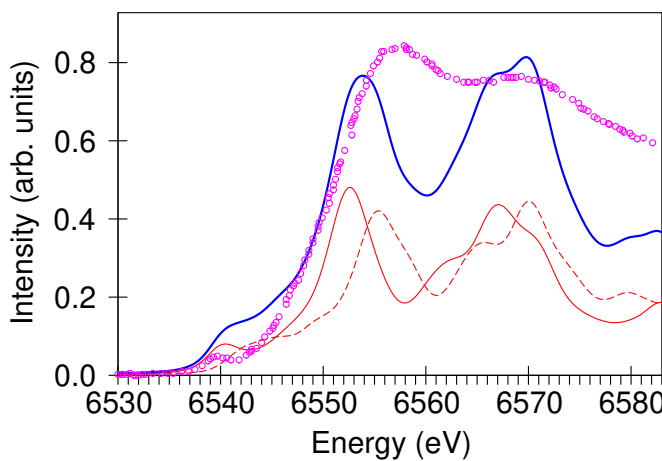


Figure 3.6. Experimental [69] (circles) and theoretically calculated spectra without any additional defects (dashed red line) and with the oxygen vacancy taking into account (full blue line) in  $(\text{Zn}_{0.97}\text{Mn}_{0.03})\text{O}$  at the Mn  $K$  edge.

core level [216]. Therefore,  $K$  XA spectrum occupies a larger energy interval and has less pronounced fine structures in comparison with the Mn  $L_3$  spectrum. As a result, the influence of lattice imperfections such as oxygen deficiencies or Zn excess is smaller in the Mn  $K$  XA spectrum. Although, taking the oxygen deficiencies into account slightly improves the agreement between the theory and the experiment (see Fig. 3.6).

**XA spectra at the Zn and O  $K$  edges.** Figure 3.7 shows their measurements in comparison with calculational results for two different Mn concentrations. The spectra for Mn-doped ZnO possess several fine structures, such as major peak  $b$  at 538 eV with a low-energy shoulder, double peak  $c$  in the 539–545 eV energy range, a wide high energy structure  $d$ , and a small near-edge peak  $a$  at about 529 eV. The theoretical

### XMCD spectra at the Mn $K$ edges.

Figure 3.6 presents the experimental [69] and calculated in the LSDA XA spectra of  $(\text{Zn},\text{Mn})\text{O}$  at the Mn  $K$  edge. The theory is in reasonable agreement with the experiment. The width of Mn  $2p$  energy bands in the  $(\text{Zn},\text{Mn})\text{O}$  DMS is much larger than the widths of the corresponding Mn  $3d$  bands. Besides, the width of the  $1s$  core level is almost three times larger than the width of the  $2p_{3/2}$

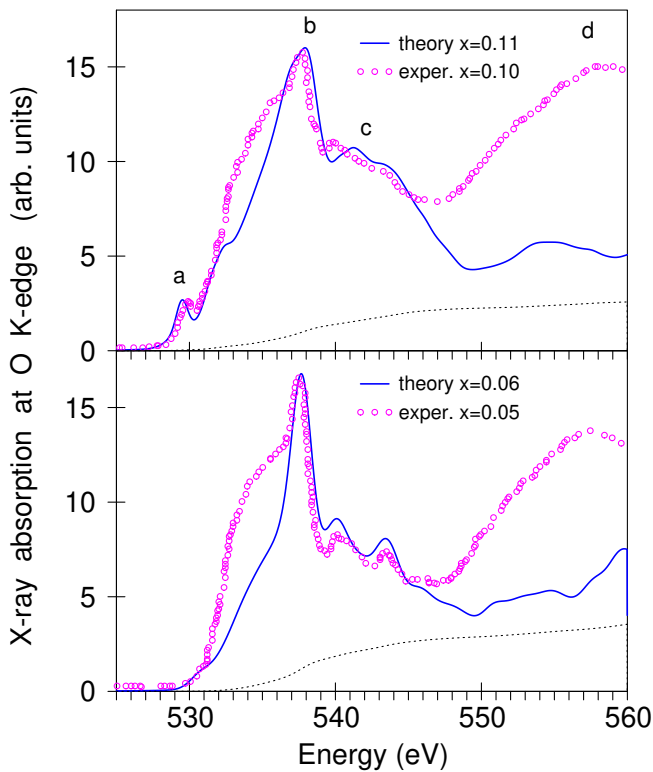


Figure 3.7. Experimentally measured [80] (circles) XA spectrum of  $(\text{Zn},\text{Mn})\text{O}$  at the O  $K$  edge and the theoretically calculated one (full line).

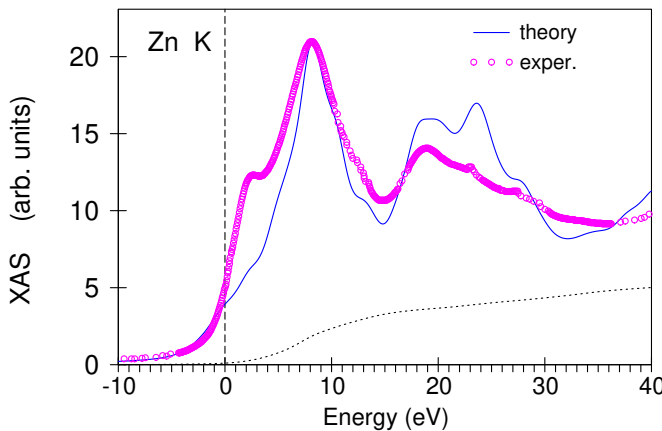


Figure 3.8. Experimentally measured [80] (circles) XA spectrum of  $(\text{Zn},\text{Mn})\text{O}$  at the Zn  $K$  edge and the theoretically calculated one (full line).

The oxygen vacancy has a minor influence on the shape of the O  $K$  XA spectrum. This is probably because of the relatively small number of oxygen ions that are influenced by the vacancy in comparison with the total number of oxygen ions in the unit cell. The low energy peak *a* originates from the Mn  $3d$  – O  $2p$  hybridization and becomes slightly broader when the oxygen vacancy is taking into account.

The theoretically calculated XA spectrum at the Zn  $K$  edge in  $(\text{Zn},\text{Mn})\text{O}$  in compar-

calculations reveal that the major peak *b* is due to transitions to non-dispersive O  $2p$  states located at 7–7.5 eV above the  $E_F$  (see Fig. 3.4). The spectral feature *c* can be attributed to the hybridization between O  $2p$  and Zn/Mn  $4p$  states. The structure *d* above 550 eV can be assigned to the hybridization between O  $2p$  and Zn and Mn  $4p/4f$  states. The spectral features above 550 eV are quite similar and are nearly independent of the Mn concentration [74]. The small peak at about 529 eV evolves with Mn doping in ZnO, and its intensity increases with increasing Mn concentrations [74] (see Fig. 3.7), suggesting a strong hybridization of O  $2p$  orbitals with Mn  $3d$  states. This feature originates from Mn doping and is ascribed to dipole transitions from O  $1s$  to O  $2p$  states that are hybridized with the unoccupied states of Mn  $3d$  (see Fig. 3.4). The increase of continuous this peak with increasing Mn doping indicates more unoccupied states at the Mn  $3d$  levels.

ison with the experimentally measured one [80] is shown in Fig. 3.8. Theory quite well reproduces the main peculiarities of the experimental spectrum, although the theory underestimates the intensity of the low energy shoulder at around 3 eV.

### 3.4 (Zn,Fe)O

**Energy band structure.** Figure 3.9 presents total and partial DOS for a 36-atom ZnO wurtzite unit cell containing one Fe substitution ( $x = 1/18$ ) in the LSDA. The O  $s$  states are located mostly between  $-21.0$  eV to  $-20.0$  eV below the  $E_F$  (not shown) and the  $p$

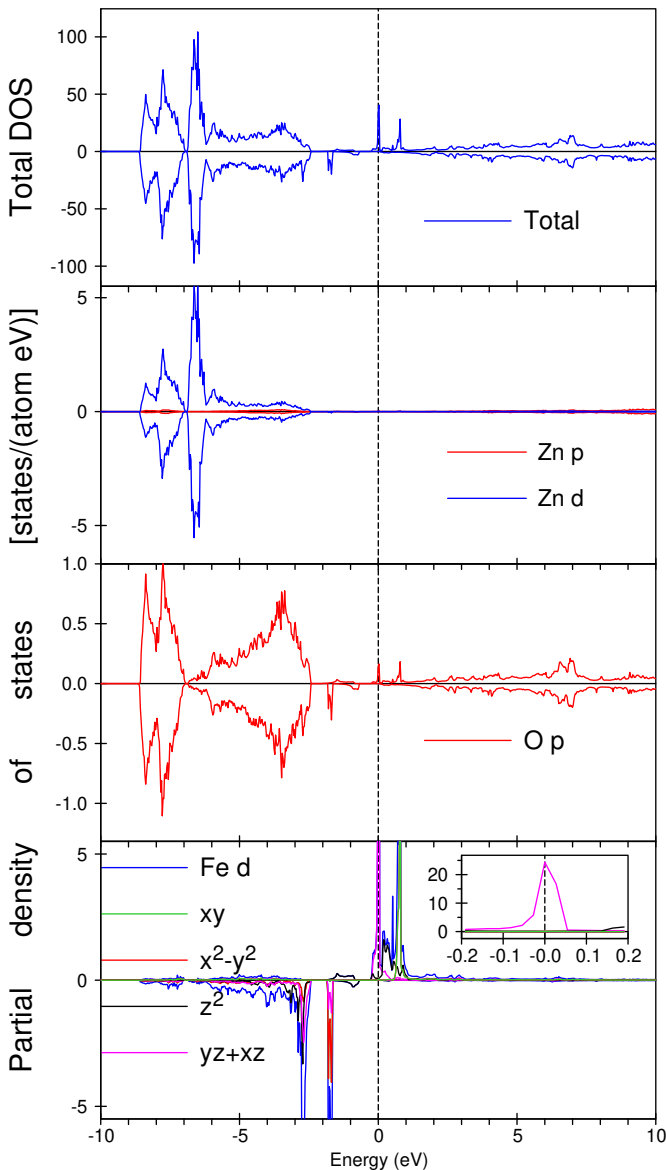


Figure 3.9. The LSDA total [in states/(cell eV)] and partial [in states/(atom eV)] DOS, calculated by the LMTO method, for the O, Zn and substituted Fe ions in  $Zn_{0.94}Fe_{0.06}O$  [3]. The insert is a blowup of the Fe  $d$  partial DOS close to the  $E_F$ . The  $E_F$  is at zero.

states of the O are found between  $-8.5$  eV to  $-2.5$  eV. The spin splitting of the O  $p$  states is quite small. Zn  $d$  states occupy the energy interval between  $-8.5$  eV and  $-2.5$  eV and hybridize strongly with the O  $p$  states.

The majority-spin Fe  $d_{yz} + d_{xz}$  structure is found at the  $E_F$  between  $-0.05$  eV and  $0.05$  eV (see the insert in the bottom panel of Fig. 3.9). Very strong and narrow peak of the minority-spin Fe bonding  $d_{x^2-y^2}$  states are located between  $-1.8$  eV and  $-1.6$  eV below the  $E_F$ . Narrow peak of the  $d_{xy}$  symmetry occurs in the majority-spin channel at around  $0.8$  eV above the  $E_F$ . DOS almost vanishes at  $1.0$  eV above  $E_F$ .

The Fe in LSDA stays in 2+ state. Often Fe ions exhibit charge order with alternating 2+-3+ valence. To calculate different Fe occupation number one has to use LSDA+ $U$  approach. The

LSDA+ $U$  calculations with  $U = 4.0$  eV and  $J = 0.8$  eV self-consistently converge to Fe  $d^5$  configuration (3+) so in order to get Fe  $d^6$  (2+ valence) configuration one has to perform constrained LSDA+ $U$  calculations. It turns out Fe  $d^5$  state is lower in energy.

**XA and XMCD spectra at the Fe  $L_{2,3}$  edges.** Fig. 3.10 presents experimental [82] and calculated XA and XMCD spectra of (Zn,Fe)O at the Fe  $L_{2,3}$  edges. The line shape of the XA spectrum at the Fe  $L_3$  edge in the (Zn,Fe)O DMS has a two-peak structure with major peak at 710 eV and smaller one at 708.5 eV. The major peak possesses an additional high energy shoulder.

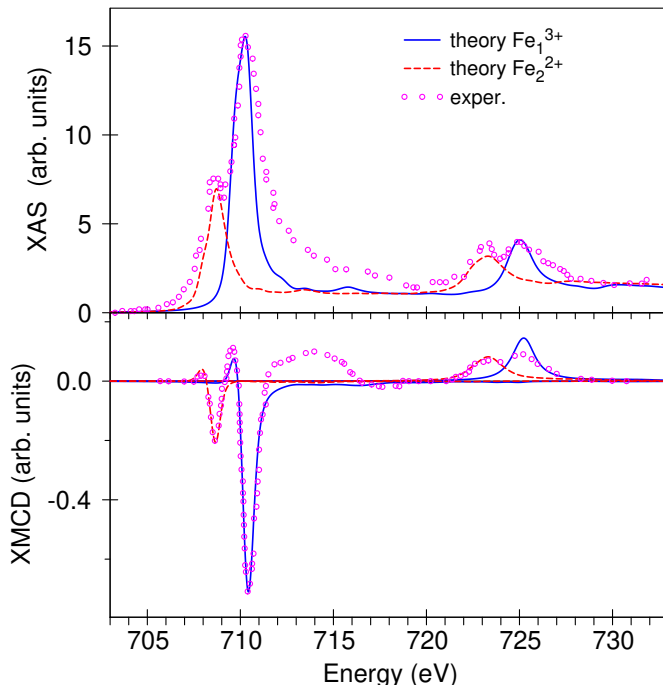


Figure 3.10. XA (top panel) and XMCD (lower panel) experimental spectra [82] (circles) of (Zn,Fe)O at the Fe  $L_{2,3}$  edges and theoretically calculated spectra for the  $\text{Fe}_1^{3+}$  without any additional defects (full lines) and  $\text{Fe}_2^{2+}$  with the oxygen vacancies (dashed lines).

$L_3$  XA spectrum quite well except for high energy structure at 711–714 eV which is not reproduced by the theoretical calculations. It might be that the additional satellite structure at the high energy tail of the Fe  $L_3$  XA spectrum appear due to many-body effects. The theoretically calculated Fe  $L_{2,3}$  XMCD spectra are in good agreement with the experiment (see lower panel in Fig. 3.10). The low energy minimum at around 708.5 eV is found to be due to oxygen vacancy in the (Zn,Fe)O DMS. The theory does not produce the fine structure corresponding to the high energy satellite structure at around 711–714 eV.

As may be seen from the top panel of Fig. 3.10 the calculations for the ideal crystal structure with one substituted  $\text{Fe}_1^{3+}$  atoms (full curve) reproduce the XA intensity only at the major peaks only. The oxygen vacancy strongly affects the shape of the XA spectra. As may be seen from Fig. 3.10 (top panel) the XA from the  $\text{Fe}_2^{2+}$  atoms with the oxygen vacancy (dashed line) mostly determined the shape of the low energy peak at 708.5 eV. Therefore, the calculations taking into account oxygen deficiency reproduce the shape of the Fe

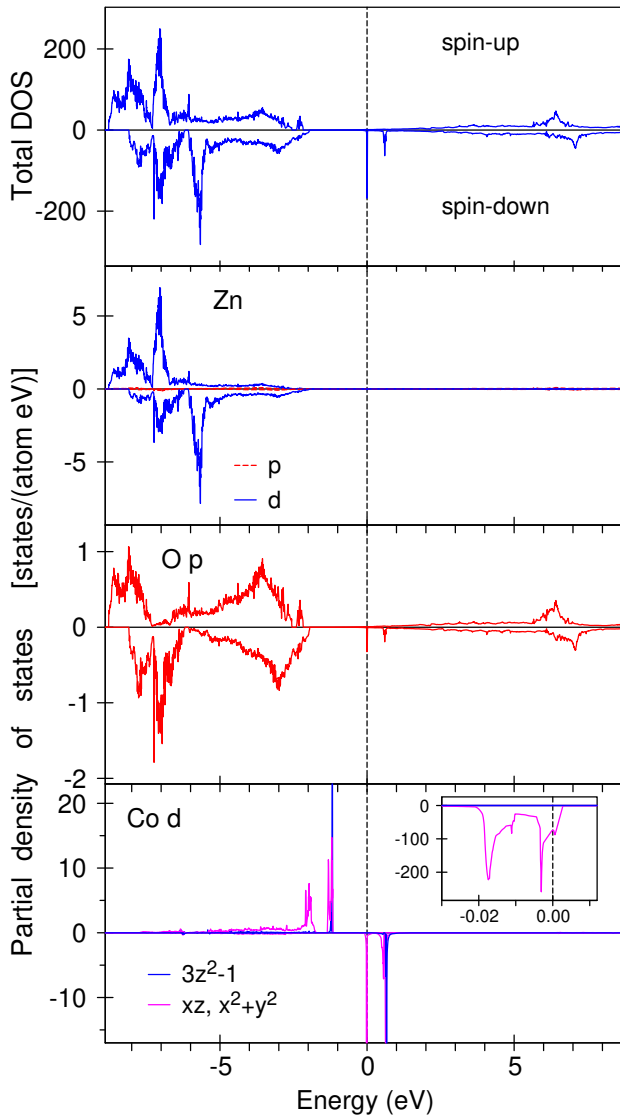


Figure 3.11. The LSDA total [in states/(cell eV)] and partial [in states/(atom eV)] DOSs for the O, Zn and substituted Co ions in  $(\text{Zn}_{0.03}\text{Co}_{0.03})\text{O}$ . The insert is a blowup of the Co  $d$  partial DOS close to the  $E_{\text{F}}$ . The  $E_{\text{F}}$  is at zero.

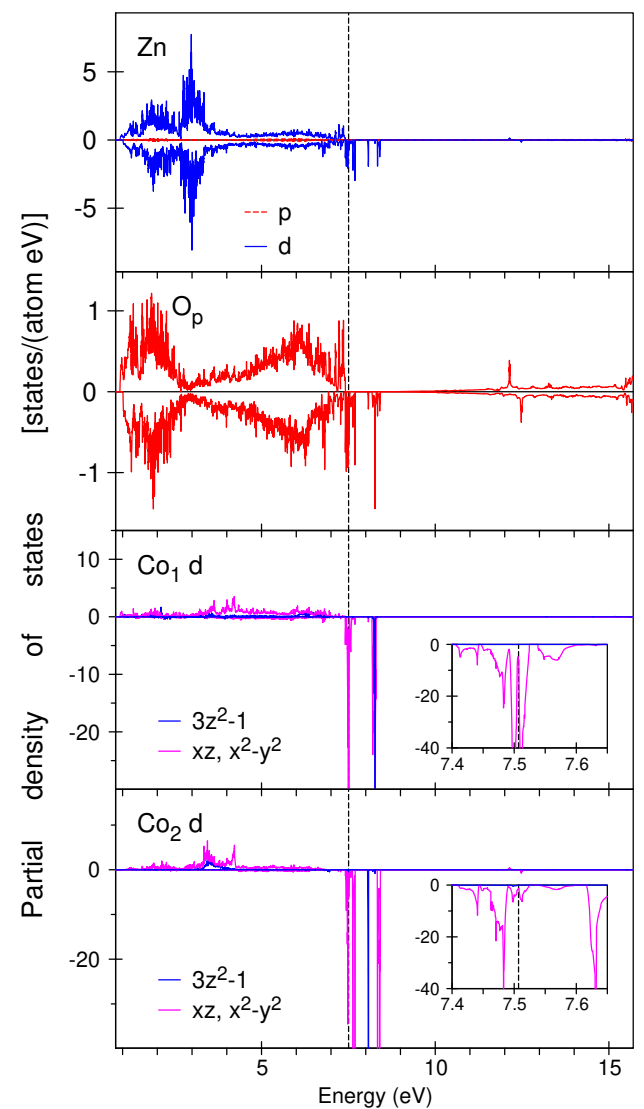


Figure 3.12. The partial DOS [in states/(atom eV)] for the O, Zn and substituted  $\text{Co}_1$  and  $\text{Co}_2$  ions in the  $(\text{Zn}_{0.94}\text{Co}_{0.06})\text{O}$  as shown in Fig. 3.1 calculated in LSDA. The insert is a blowup of the  $\text{Co}_1$  and  $\text{Co}_2$   $d$  partial DOS close to the  $E_{\text{F}}$ .

### 3.5 $(\text{Zn}, \text{Co})\text{O}$

**Energy band structure.** Figure 3.11 presents total and partial DOS for a 72-atom  $\text{ZnO}$  wurtzite unit cell containing one Co substitution ( $x = 0.03$ ) in the LSDA and a FM arrangement of the Co moments. The O  $2s$  states are located mostly between  $-19.7$  eV to  $-18.7$  eV below the  $E_{\text{F}}$  (not shown) and the  $p$  states of the O are found between  $-8.7$  eV to  $-1.8$  eV. The spin splitting of the O  $p$  states is quite small. Zn  $d$  states occupy the energy interval between  $-8.8$  eV and  $-1.8$  eV and hybridize strongly with the O  $p$  states.

The Co 3d impurity states well hybridize with the O 2p conduction band, which gives the solution a metallic character. The crystal field at the Co substitutional site ( $C_{3v}$  point symmetry) causes the splitting of Co  $d$  orbitals into a singlet  $a_1$  ( $d_{3z^2-1}$ ) and two doublets  $e$  ( $d_{yz}$  and  $d_{xz}$ ) and  $e_1$  ( $d_{xy}$  and  $d_{x^2-y^2}$ ). Very strong and narrow two-peak structure of the minority-spin Co  $d_{xz}$  and  $d_{x^2-y^2}$  symmetry is found in close vicinity to the  $E_F$  (see the insert in the bottom panel of Fig. 3.11). The energy split between the two peaks are around 14 meV. The  $E_F$  is situated at the shoulder of the second high energy peak. Peaks of the  $d_{xz}$  and  $d_{x^2-y^2}$  symmetry occur in the minority-spin channel at the 0.45 eV to 0.67 eV above the  $E_F$ . The energy interval of 0.6 eV to 0.7 eV above the  $E_F$  is occupied by the  $d_{3z^2-1}$  states with minority-spin.

The magnetic moment in the  $(Zn_{0.97}Co_{0.03})O$  unit cell is  $3.947 \mu_B$ . The band structure calculations yield the spin magnetic moment of  $3.412 \mu_B$  for the Co atoms. The induced spin magnetic moments at the O first neighbor sites are of  $0.048 \mu_B$ , and  $0.173 \mu_B$ , for longer and shorter distant O atoms, respectively. Twelve Zn ions in the second neighbor shell couple ferromagnetically to the substituted Co ion with spin magnetic moments from  $0.014 \mu_B$  to  $0.043 \mu_B$ . The orbital moments at the Zn and O sites are small with the largest one at the O first neighbor sites ( $-0.011 \mu_B$ ). The orbital magnetic moment at the Co site is  $0.353 \mu_B$  and is parallel to the spin one.

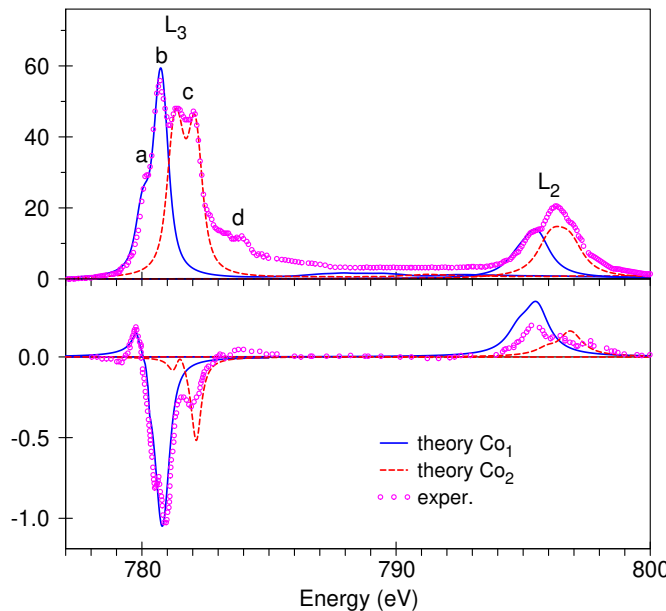


Figure 3.13. XA (top panel) and XMCD (lower panel) experimental spectra (circles) [99] of  $(Zn_{0.93}Co_{0.07})O$  at the Co  $L_{2,3}$  edges and theoretically calculated spectra for the  $Co_1$  without any additional defects (full blue lines) and  $Co_2$  with the oxygen vacancy (see Fig. 3.1) (dashed red lines) ions.

To investigate the influence of possible oxygen vacancies on the electronic structure of the  $(Zn,Co)O$  DMSs the LMTO band structure calculations with two of the Zn ions replaced by Co with different environments for the composition  $x = 2/36$  have been performed. An oxygen vacancy in the first neighborhood of the  $Co_2$  along the  $z$  direction (see Fig. 3.1) has been created. Fig-

ure 3.12 presents the LSDA partial DOSs for the O, Zn and substituted Co<sub>1</sub> and Co<sub>2</sub> ions in the (Zn,Co)O. The oxygen vacancy has four nearest neighbors atoms: three Zn atoms at the distance of 1.9496 Å and one Co atom at the 1.9505 Å. The lattice relaxation is found to be very important in the presence of the oxygen vacancy. The lattice relaxation causes the shift of the Co<sub>2</sub> atom and the three Zn atoms toward the

vacancy by 0.13 Å and 0.24 Å, respectively. The oxygen vacancy strongly affects the energy distribution of the partial DOSs in close vicinity to the  $E_F$  for the relaxed lattice.

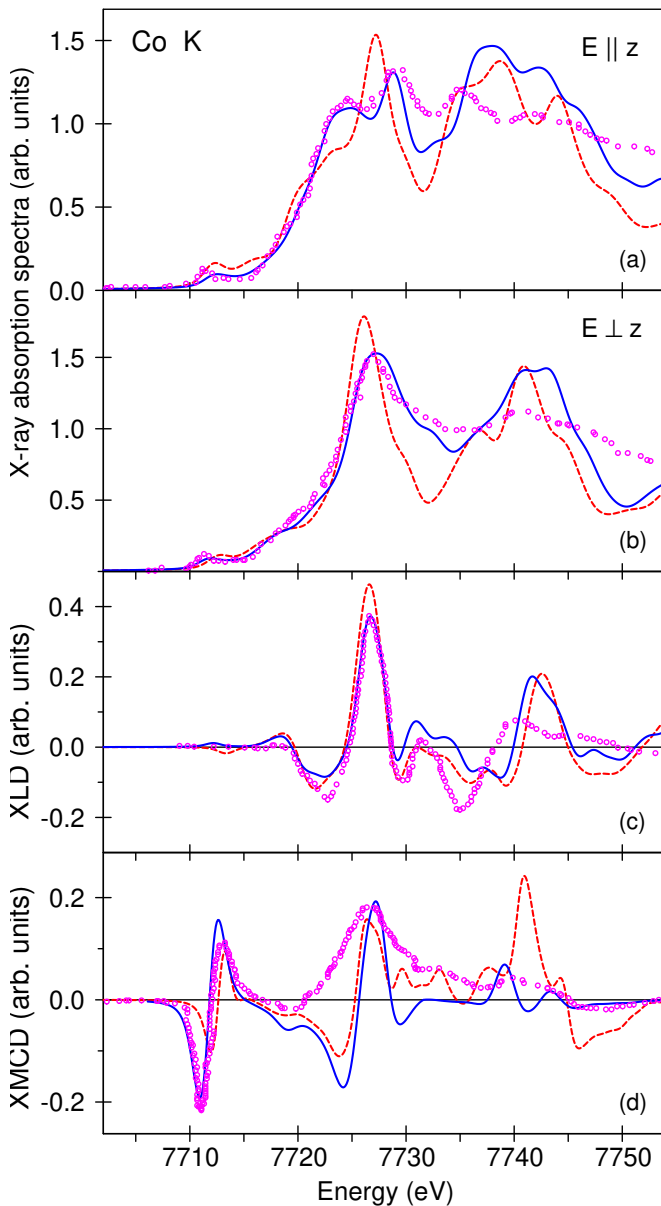


Figure 3.14. The experimentally measured [87] (circles) XA spectra of (Zn<sub>0.9</sub>Co<sub>0.1</sub>)O at the Co  $K$  edge with the electric field vector of the x-rays parallel (a) and perpendicular (b) to the  $z$ -axis in comparison with the theoretically calculated spectra without (red dashed line) and with (full blue line) oxygen vacancy; (c) theoretically calculated and experimental [87] XLD spectra at the Co  $K$  edge; (d) the theoretically calculated and the experimental [87] XMCD spectra at the Co  $K$  edge.

**XA and XMCD spectra at the Co  $K$  and  $L_{2,3}$  edges.** Fig. 3.13 presents experimental XA and XMCD spectra [99] at the Co  $L_{2,3}$  edges and the spectra calculated in the LSDA. The XA spectrum at the Co  $L_3$  edge is rather complicated and consists of two major structures: peak *b* at around 780.9 eV with a low energy shoulders *a* at 780 eV and double peak *c* at 781.6–782.4 eV with high energy fine structure *d* at 784 eV.

As may be seen from the top panel of Fig. 3.13 the calculations for the ideal crystal structure with one substituted Co<sub>1</sub> atoms (full blue curve) reproduce the XA intensity only at the peaks *a* and *b*. The full explanation of the spectra is only possible by taking crystal imperfections such as oxygen deficiency into account. The oxygen vacancy (with lat-

tice relaxation taken into account) strongly affects the shape of the XA spectra. As may be seen from Fig. 3.13 (top panel) the XA from the Co<sub>2</sub> atoms with the oxygen vacancy (red dashed line) mostly determined the shape of the major double peak *c*. Therefore, our calculations including oxygen deficiency reproduces the shape of the Co *L*<sub>3</sub> XA spectrum quite well except for high energy structure *d* which is not reproduced by the theoretical calculations. It might be that the additional satellite structure at the high energy tail of the Co *L*<sub>3</sub> XA spectrum appear due to many-body effects. This question needs an additional theoretical investigation using an appropriate many-body treatment.

The theoretically calculated Co *L*<sub>2,3</sub> XMCD spectra are in good agreement with the experiment (lower panel in Fig. 3.13). The high energy minimum at around 782 eV is found to be due to oxygen vacancy in the (Zn,Co)O DMS. The theory does not produce the fine structure corresponding to the high energy satellite structure *d* at around 784 eV.

Fig. 3.14 shows the experimental XA spectra at the Co *K* edge in (Zn<sub>0.9</sub>Co<sub>0.1</sub>)O [87]. The associated XLD signal, obtained by taking the difference of the XA spectra for the two polarizations, is given in the panel (c) of Fig. 3.14. Two theoretical results are presented: without any additional defects (red dashed lines) and with the oxygen vacancy (full blue lines). Clearly latter results are in better agreement with the experimental measurements of the XA spectra for both polarizations. The agreement between the theory and the experiment for the XLD spectrum at the Co *K* edge is also quite good (Fig. 3.14 (c)). Although, there are the systematical energy shifts of the major peaks in the

calculated spectra above 735 eV toward higher energy for both the calculations in comparison with the experiment.

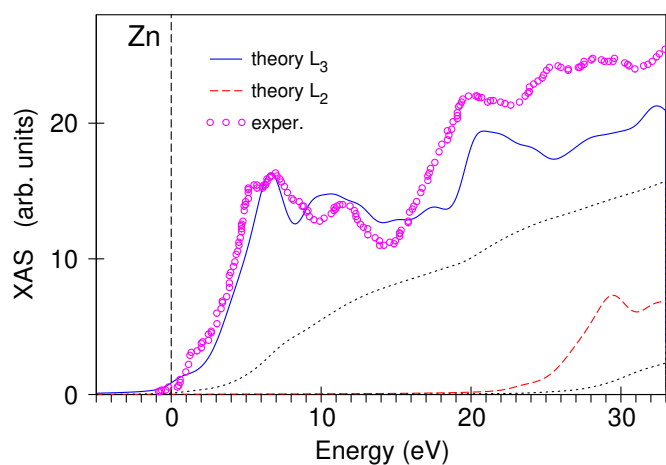


Figure 3.15. The experimentally measured [86] (circles) XA spectra of (Zn,Co)O at the Zn *L*<sub>2,3</sub> edges and the theoretically calculated ones (full line).

The experimentally measured Co *K* XMCD spectrum (Fig. 3.14 (d)) has a very intense signal in close vicinity to the edge [87]. The theory reproduces the major negative and positive peaks near the edge well but shows an additional negative peak at around 7724 eV which

is absent in the experiment. The oscillatory behavior of the high energy part of the theoretical XLD and XMCD spectra at the Co  $K$  edge could possibly be damped by quasiparticle life-time effects not taken into account in calculations.

**XA and XLD spectra at the Zn  $L_{2,3}$  edges.** Figure 3.15 shows the theoretically calculated XA spectra at the Zn  $L_{2,3}$  edges in (Zn,Co)O DMS in comparison with the experimentally measured ones [86]. Theory reproduces reasonably well the main peculiarities of the experimental spectrum, although the theory underestimate the intensity of high energy peaks above 20 eV relative to  $E_F$ .

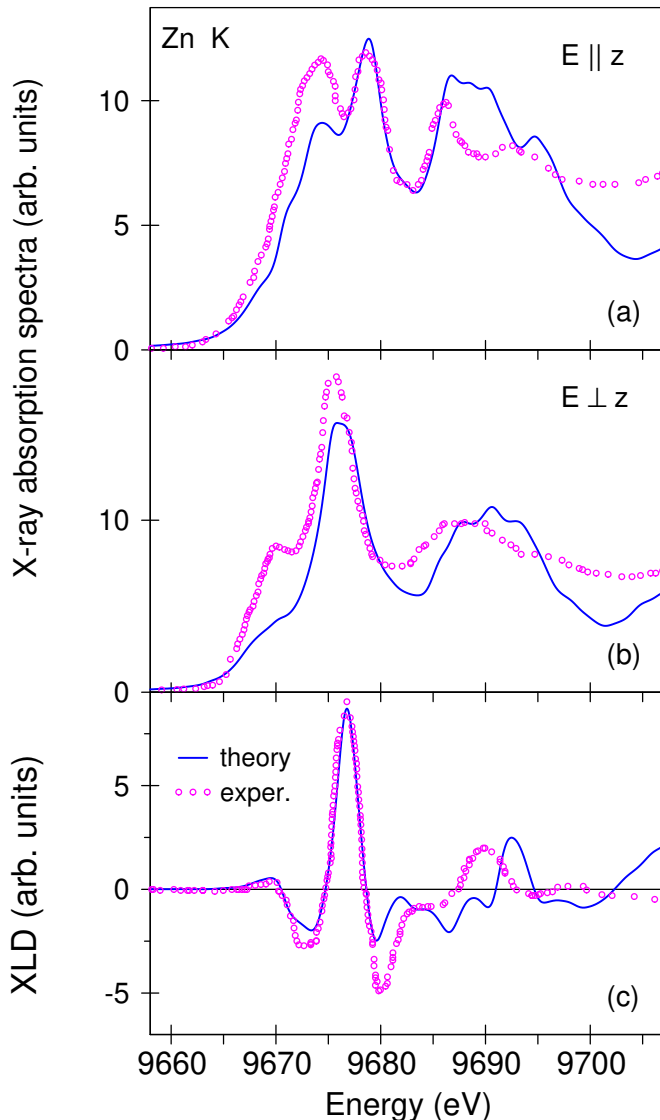


Figure 3.16. Theoretically calculated (full line) and experimentally measured [87] (circles) XA spectra of (Zn,Co)O at the Zn  $K$  edge with the electric field vector of the x-rays parallel (a) and perpendicular (b) to the  $c$ -axis; (c) theoretically calculated (full line) and experimental [87] (circles) XLD spectra at the Zn  $K$  edge.

**XA and XLD spectra at the Zn  $K$  edges.** Figure 3.16 shows the experimental XA spectra recorded at the Zn  $K$  edge at room temperature in a  $(\text{Zn}_{0.9}\text{Co}_{0.1})\text{O}$  epitaxial film with the electric field vector of the x-rays parallel (upper panel) and perpendicular (middle panel) to the  $c$  axis [87]. The associated XLD spectra, obtained by taking the difference of the XA spectra for the two polarizations, is given in the lower panel of Fig. 3.16. Because of the uniaxial crystal symmetry of the wurtzite lattice, the final states are split by the crystal field. Hence, the XLD is purely a result of the structure. The LSDA theory reproduces the shape of XA and XLD spectra quite well (Fig. 3.16).

There is a small disagreement between the theory and the experiment in the relative intensities of the low energy peak of the XA spectra in both the po-

larizations. Also, the theoretically calculated high energy peak in the XLD spectrum at around 9690 eV is slightly shifted to higher energies as compared with the experiment.

**XA spectra at the O K edge.** XA spectra at the oxygen *K* edge were measured by Kumar *et al.* [93] in the  $(\text{Zn}_{1-x}\text{Co}_x)\text{O}$  ( $x = 0, 0.01, 0.03$ , and  $0.05$ ). The O *K* edge spectra fundamentally reveal a transition from the O *1s* core state to the unoccupied O *2p* derived states, which are hybridized with the relatively narrow *3d* band and broader *4sp* bands of the Co ions. Fig. 3.17 presents experimentally measured [93] O *K* XA spectra of  $(\text{Zn}_{1-x}\text{Co}_x)\text{O}$  ( $x = 0, 0.01$ ) in comparison with the calculations. The spectra for Co-doped ZnO possess several fine structures such as the major peak *b* at 535 eV with a low energy shoulder, a double peak *c* occurring in the 538–542 eV energy range, a wide high energy structure *d* and a small near-edge peak *a* at about 528 eV. In the theoretical calculations it is found the major peak *b* is due to transition to non-dispersive O *2p* states located at 5–7 eV above  $E_F$  (see Fig. 3.11). The spectral feature *c* is attributed to the hybridization between O *2p* and Zn/Co *4p* states. The structure *d*

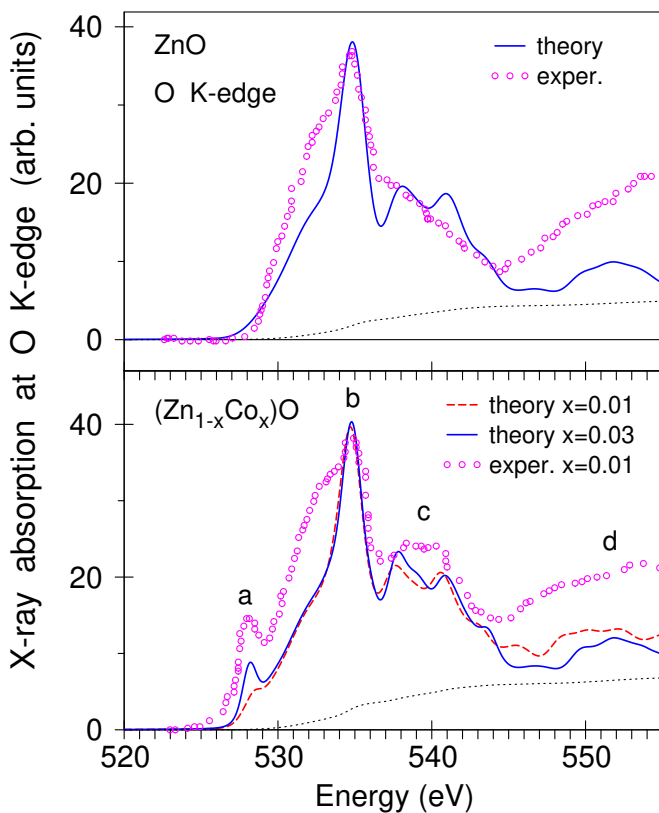


Figure 3.17. The experimentally measured [93] (circles) XA spectra at the O *K* edge in the ZnO (upper panel) and  $(\text{Zn}_{1-x}\text{Co}_x)\text{O}$  ( $x=0.01$ ) (lower panel) in comparison with the theoretically calculated ones (full lines).

above 550 eV is assigned to the hybridization between O *2p* and Zn and Co *4p/4f* states. By comparing the O *K* XA spectra of Co-doped ZnO (lower panel of Fig. 3.17) with that of undoped ZnO (upper panel of Fig. 3.17), one observes that an extra spectral feature evolve at 528 eV (marked by *a*) and that the intensity of this feature increases with Co doping [93], suggesting a strong hybridization of O *2p* orbitals with Co *3d* states. This feature originates in Co doping, and it is ascribed to dipole transitions from O *1s* to O *2p* states that are hybridized with the unoccupied states of Co *3d* just above the  $E_F$  at the 0 to 0.7 eV energy

range (see Fig. 3.11). Thus, the intensity of this peak represents the Co 3d DOS. A continuous increase of this peak with Co doping indicates more unoccupied states at the Co 3d levels.

The intensity of the peak *a* is much smaller in our theoretical calculations in comparison with the experiment [93]. On the other hand, Thakur *et al.* [74] measured the XA spectra at the oxygen *K* edge in the  $(\text{Zn}_{1-x}\text{Mn}_x)\text{O}$  for  $x = 0.03, 0.05, 0.07, 0.10$ , and 0.15. They also found that the low energy peak near the *K* edge increases with increasing Mn concentration. Although, the intensity of the peak is much smaller in their measurements in comparison with the corresponding peak intensity in the  $(\text{Zn},\text{Co})\text{O}$  in Ref. [93]. The measurement of Kumar *et al.* [93] in the  $(\text{Zn}_{1-x}\text{Co}_x)\text{O}$  for  $x = 0.01$  corresponds approximately to those of Thakur *et al.* [74] in  $(\text{Zn}_{1-x}\text{Mn}_x)\text{O}$  for  $x = 0.15$ . The calculations almost perfectly reproduce the concentration dependence of the peak *a* observed in the Ref. [74] for the  $(\text{Zn},\text{Mn})\text{O}$  DMSs. The authors of Ref. [244] also measured the XA spectrum at the oxygen *K* edge in  $(\text{Zn}_{1-x}\text{Cu}_x)\text{O}$  for various  $x$  and found relatively low intensity of the corresponding near-edge XA fine structure, similar to the measurements on the  $(\text{Zn},\text{Mn})\text{O}$  DMSs [74] and these calculations. The nature of such a very intense low energy peak in  $(\text{Zn},\text{Co})\text{O}$  observed experimentally in the Ref. [93] is still not clear and needs an additional experimental study.

Possible reasons for the increase of the intensity of this peak might be sought in surface effects. To investigate the influence of the surface on the XA and XMCD spectra one may apply two different methods, namely, total fluorescent yield (TFY) and total electron yield (TEY) spectroscopy. The TFY method can be considered as mostly a bulk method because it has the probing depth of  $\sim 10\text{--}100\text{ nm}$ , while TEY gives increased sensitivity to the surface of the layers with probing depth of  $\sim 3\text{ nm}$ . Thakur *et al.* [244] measured the XA at the O *K* edge in the  $(\text{Zn},\text{Cu})\text{O}$  using both the TFY and TEY detection modes. They found noticeable increase of XA at the low energy shoulder of the peak *b* around 532 eV using the TEY detection mode in comparison with the TFY one. On the other hand, Kumar *et al.* [93] claimed that the spectra in the two modes turned are nearly identical in the case of the  $(\text{Zn},\text{Co})\text{O}$ .

The oxygen vacancies have minor influence on the shape of the O *K* XA spectrum.

This is probably because there are a relatively small number of the oxygen ions which are influenced by the vacancies in comparison with a total number of the oxygen ions in the unit cell. The low energy peak *a* which due to Co 3d – O 2p hybridization only became slightly broader when oxygen vacancies are introduced.

### 3.6 Conclusions for Chapter 3

The electronic band structure and x-ray spectra of (Zn,T)O diluted magnetic semiconductors (T = V, Mn, Fe, and Co) have been investigated theoretically within a LSDA in the framework of the SPR LMTO band structure method.

The shape of the V  $L_{2,3}$  XMCD spectra is explained only by suggesting the AFM ordering between the V ions situated at the largest possible distance between V atoms with different spins and only in the presence of an oxygen vacancy located in the first neighborhood of the second V atom. Adding extra Zn atoms improves the agreement between the theory and the experiment as well. The lattice relaxation is found to be very important in the presence of the oxygen vacancy as well as Zn excess.

The oxygen deficiency is responsible for the double-peak structure of the dopant  $L_3$  XA spectrum of the (Zn,T)O DMS for T = Mn and Co. The oxygen vacancy has minor influence on the shape of the O and Zn  $K$  XA spectra. Zn excess only slightly improved the agreement with the experiment by increasing the intensity of the high-energy features of x-ray spectra. The intensity of small pre-peak structure in the O  $K$  XA spectrum appears with increasing T concentration, suggesting a strong hybridization of O 2p orbitals with T 3d states. This peak is a fingerprint of the T 3d states. Because of the uniaxial crystal symmetry of the wurtzite lattice, the final states are split by the crystal field. The XLD is purely a result of this symmetry and reproduced in the calculations.

The main peaks of Fe x-ray spectra of (Zn,Fe)O DMS are reproduced in the ideal crystal structure with one substituted  $\text{Fe}^{3+}$  atom. The substituted  $\text{Fe}^{2+}$  atom and the oxygen vacancy mostly form the low energy peaks of the double-peak Fe x-ray spectra.

# CHAPTER 4

## ELECTRONIC BAND STRUCTURE AND X-RAY SPECTRA IN A-SITE ORDERED DOUBLE PEROVSKITES

### 4.1 CaMnTi<sub>2</sub>O<sub>6</sub>

The original results discussed in this Section are published in [4].

#### 4.1.1 Crystal structure and details of calculations

CaMnTi<sub>2</sub>O<sub>6</sub> possesses the noncentrosymmetric space group *P4<sub>2</sub>mc* (No. 105), which is a subgroup of *P4<sub>2</sub>/mmc* [129]. The crystal structure of CaMnTi<sub>2</sub>O<sub>6</sub> is shown in Fig. 4.1. There are two Mn<sup>2+</sup> sites, two Ca<sup>2+</sup> sites, one Ti<sup>4+</sup> site, and five O<sup>2-</sup> sites in this tetragonal structure. Each cation is completely ordering in their site. The crystal parameters of CaMnTi<sub>2</sub>O<sub>6</sub> are presented in Table 4.1.

The octahedral B positions are occupied by Ti<sup>4+</sup> ions. In the A-site, Ca<sup>2+</sup> alternate with Mn<sup>2+</sup> ions along *a* and *b* axes forming a columnar ordered structure. In addition, the two Mn positions exhibit different coordination: tetrahedral at Mn<sub>1</sub> sites

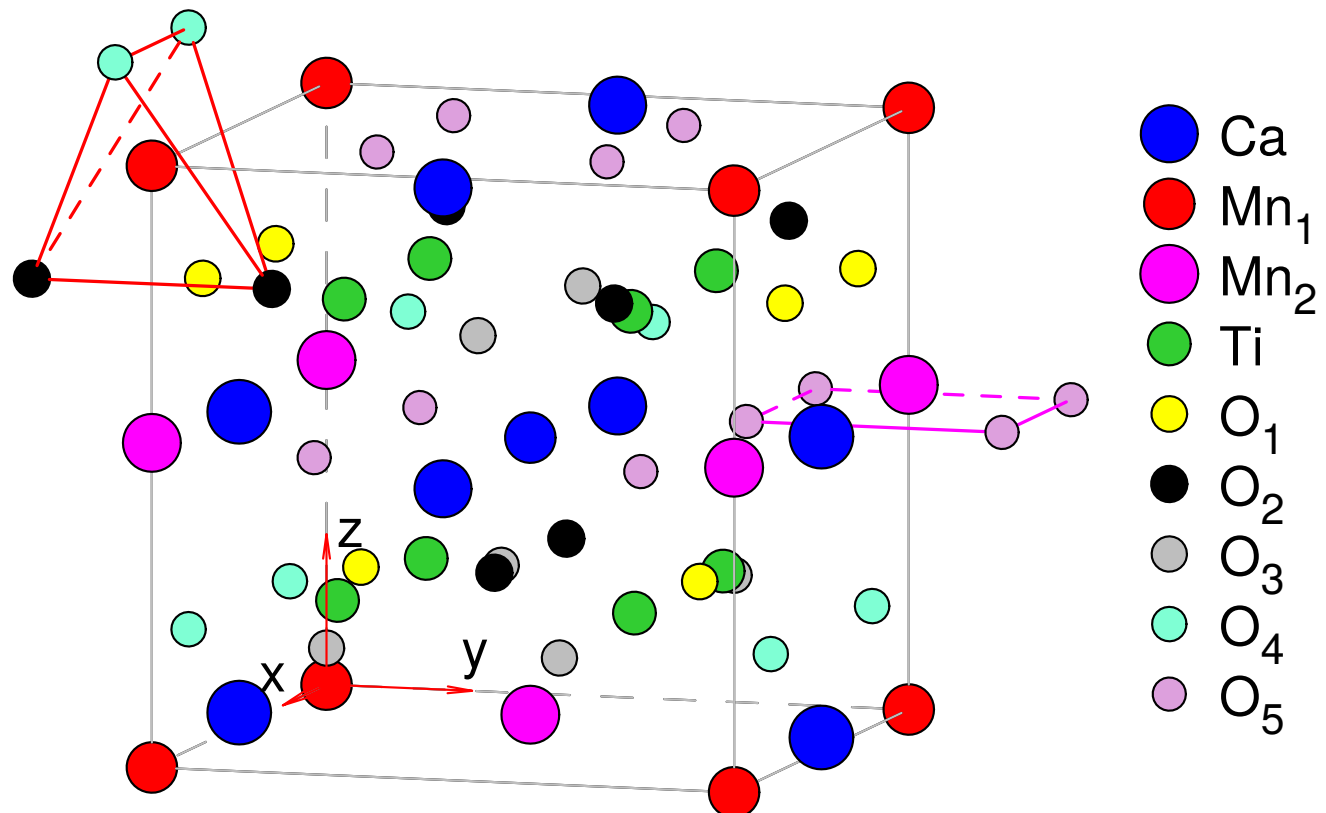


Figure 4.1. Crystal structure of the ferroelectric CaMnTi<sub>2</sub>O<sub>6</sub>.

Table 4.1. The atomic positions of  $\text{CaMnTi}_2\text{O}_6$  at room temperature. The lattice parameters are  $a = 7.5376 \text{ \AA}$ , and  $c = 7.6002 \text{ \AA}$  [110].

Atom	Site	$x$	$y$	$z$
Ca <sub>1</sub>	2a	0	0	0
Ca <sub>2</sub>	2b	0.5	0.5	0.0385
Mn <sub>1</sub>	2c	0	0.5	0.5162
Mn <sub>2</sub>	2c	0	0.5	0.0557
Ti	8f	0.255	0.2461	0.270
O <sub>1</sub>	4e	0.291	0.5	0.289
O <sub>2</sub>	4d	0.294	0	0.820
O <sub>3</sub>	4d	0.202	0	0.227
O <sub>4</sub>	4e	0.210	0.5	0.717
O <sub>5</sub>	8f	0.1976	0.2805	0.013

and pseudosquare planar at  $\text{Mn}_2$  (Fig. 4.1). In contrast to the centrosymmetric double perovskite structure adopted by  $\text{CaFeTi}_2\text{O}_6$  ( $P4_2/nmc$ ) [245],  $\text{Ti}^{4+}$  ions in  $\text{CaMnTi}_2\text{O}_6$  are shifted from the basal plane of the octahedron along the  $c$  axis, losing spatial inversion [129]. These distortions result in a polar structure. Similar to that of  $\text{CaFeTi}_2\text{O}_6$ , the structure of  $\text{CaMnTi}_2\text{O}_6$  is based on a framework of corner-sharing of  $\text{TiO}_6$  octahedra with  $a^+a^+c^-$  tilting in Glazer's notation [116] and the  $\text{Mn}^{2+}$  and  $\text{Ca}^{2+}$  are ordered into columns directed along the  $c$ -axis. For its part,  $\text{Mn}^{2+}$  ions with square-planar coordination suffer a similar displacement (see the shift of  $\text{Mn}_2$  atoms along  $z$  direction in Fig. 4.1). Indeed, the reduced crystal field energy provided by their  $d^5$  valence band configuration allows high coordination symmetry freedom. As a consequence, a remnant polarization of  $3.5 \text{ mC/cm}^2$  gets measured at room temperature [110].

The agreement between the theoretically calculated and experimentally measured x-ray spectra becomes much better with taking into account strong Coulomb correlations, so the LSDA+ $U$  method (see the end of Chapter 2). The constrained LSDA calculations for  $\text{CaMnTi}_2\text{O}_6$  give  $J = 0.9 \text{ eV}$  and  $0.85 \text{ eV}$  for the Mn and Ti, respectively. The Hubbard  $U$  is treated as an external parameter and varied from  $3.0 \text{ eV}$  to  $7.0 \text{ eV}$  to achieve the best agreement with the experiment. The value of  $U_{\text{eff}} = U - J = 3.1 \text{ eV}$  and  $3.15 \text{ eV}$  for Mn and Ti, respectively, gives the best agreement between the calculated and experimental XMCD spectra in  $\text{CaMnTi}_2\text{O}_6$ .

The calculations have been carried out including a hole at the core orbital using the supercell approximation. The supercell used is as large as  $2 \times 2 \times 2$  of initial unit cell. At one of the Ti (Mn) atoms a hole at the  $2p_{1/2}$  or  $2p_{3/2}$  levels is created separately for the self-consistent GGA+ $U$  calculations of the  $L_2$  and  $L_3$  spectra, respectively.

### 4.1.2 Electronic band structure

**Electronic band structure and DOSs.** Usually ferroelectric oxides, such as BaTiO<sub>3</sub> and KNbO<sub>3</sub>, are wide-gap ( $E_g > 3.0$  eV) insulators. On the other hand, multiferroics BiFeO<sub>3</sub> ( $E_g = 2.7$  eV) and Bi<sub>2</sub>FeCrO<sub>6</sub> ( $E_g = 1.4\text{--}2.7$  eV) have lower band gaps suitable for absorption of visible light [130].

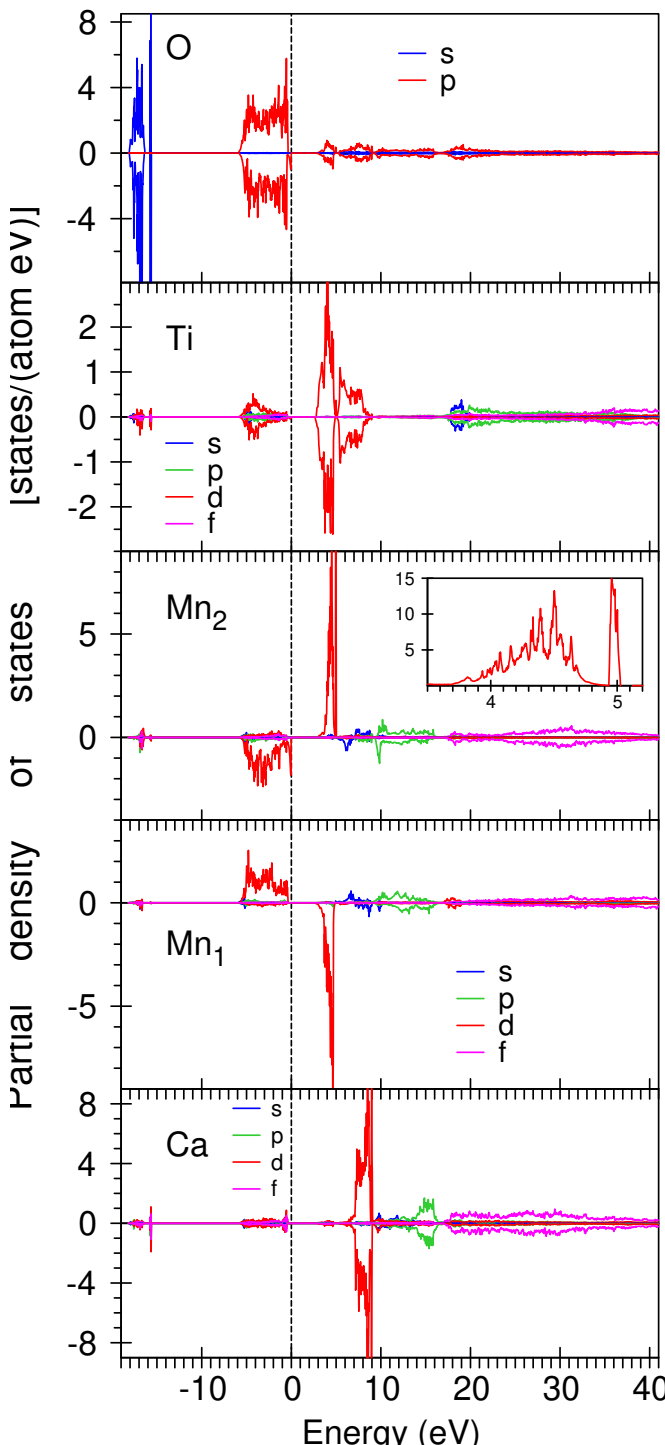


Figure 4.2. Partial DOS [in states/(atom eV)] of CaMnTi<sub>2</sub>O<sub>6</sub> in the GGA+U.

The self-consistent calculations reveal a semiconducting electronic structure in the CaMnTi<sub>2</sub>O<sub>6</sub> with energy gap of 2.52 eV in  $\Gamma$  symmetry point. One should mention Gou *et al.* [130] have got slightly larger energy gap of 2.88 eV for the C type AFM order in CaMnTi<sub>2</sub>O<sub>6</sub> using Vienna *Ab initio* Simulation Package code (VASP) [219, 220, 239, 240].

Figure 4.2 presents partial DOS for CaMnTi<sub>2</sub>O<sub>6</sub>. The O 2s states are located mostly between -15.7 eV to -18.2 eV below the  $E_F$ . Very narrow oxygen peak situated apart of the major 2p PDOS at -15.7 eV belongs to the O<sub>1</sub> site. The 2p states of the oxygen are found between -5.9 eV to -0.3 eV in CaMnTi<sub>2</sub>O<sub>6</sub>, however, small amount of empty 2p oxygen states are appeared from 3 eV to 16 eV above the  $E_F$  due to hybridization with 3d transition metal states. The spin splitting of the oxygen 2p states is quite small around 0.1 eV. The Ti 3d states are situated at -5.8 eV to -0.4 eV below the  $E_F$  and at 2.8 eV to 9 eV above the  $E_F$ . The

Ca  $3d$  empty states occupy the 6.8–9.2 eV energy interval, Ca  $4p$  empty states are at the 12 eV to 16 eV and Ca  $4f$  states are occupied the 17.5 eV to 40 eV above the  $E_F$ .

Mn  $3d$  states occupy the energy interval between –5.7 eV and the  $E_F$  and between 3.0 eV and 5.0 eV. They hybridize strongly with the O  $2p$  states. The self-consistent calculations reveal an C type AFM arrangement of Mn magnetic moments in CaMnTi<sub>2</sub>O<sub>6</sub>. The two Mn positions exhibit different coordination (see Fig. 4.1): tetrahedral (two O<sub>2</sub> and two O<sub>4</sub> types) at Mn<sub>1</sub> site and pseudosquare planar at Mn<sub>2</sub> site (four O<sub>4</sub> types). Due to different types of O atoms surrounding the Mn ions and different Mn-O inter-site distances Mn<sub>1</sub> and Mn<sub>2</sub> possess different valence and different magnetic moments. The Mn<sub>1</sub> and Mn<sub>2</sub> ions possess valence of 1.9+ and 2.2+, respectively. Spin magnetic moments are equal to  $4.527 \mu_B$  and  $-4.628 \mu_B$  for the Mn<sub>1</sub> and Mn<sub>2</sub>, respectively (see Table 4.2). The shapes of the  $3d$  partial DOSs are also differ from each other. There is a small energy gap of 0.25 eV between occupied  $3d$  PDOS and the  $E_F$  for the Mn<sub>1</sub> site. On the other hand, there is a strong peak at –0.1 eV in the  $3d$  PDOS without energy gap at the Mn<sub>2</sub> site. Besides, the Mn<sub>2</sub> empty  $3d$  PDOS possesses strong narrow peak at 5 eV above the  $E_F$  (see insert in Fig. 4.2), which is absent at the Mn<sub>1</sub> site. Similar peaks at –0.1 eV and 5 eV can be finding in the oxygen  $2p$  PDOS at the the O<sub>5</sub>. Therefore, such features in the  $3d$  PDOS at the Mn<sub>2</sub> site can be explained by strong hybridization between Mn<sub>2</sub>  $3d$  states and oxygen  $2p$  states of O<sub>5</sub> near-neighbors.

The crystal field at both the Mn sites ( $C_{2v}$  point symmetry) causes the splitting of Mn  $3d$  orbitals into one doublet  $a_1$  ( $d_{3z^2-1}$  and  $d_{x^2-y^2}$ ) and three singlets  $b_1$  ( $d_{xz}$ ),  $a_2$  ( $d_{xy}$ ), and  $b_2$  ( $d_{yz}$ ). Ti site possesses  $C_1$  point symmetry and Ti  $3d$  states split into five  $a$  singlets  $d_{xz}$ ,  $d_{xy}$ ,  $d_{yz}$ ,  $d_{3z^2-1}$ , and  $d_{x^2-y^2}$ .

**Magnetic moments.** Estimation of the magnetic moment values using the sum rules for experimentally measured at 5 K and external magnetic field of 6 T XA and XMCD spectra [110] gives for Ti  $m_S = 0.018 \mu_B$  and  $m_L = -0.013 \mu_B$ . The band structure calculations yield the magnetic moments for the Ti atoms  $m_S = 0.018 \mu_B$  and  $m_L = -0.001 \mu_B$  (see Table 4.2). It shows excellent agreement with experiment for the spin moment, however, the theory produces much smaller Ti orbital moment. The explanation such the disagreement is in the nature of the sum rules. XMCD sum rules

are derived within an ionic model using a number of approximations [167, 246]. The applying of the sum rules (Eq. 2.179) for the theoretically calculated XA and XMCD spectra produces the orbital magnetic moment  $m_L = -0.017 \mu_B$  at the Ti site with much better agreement with the experimental estimations.

Current band structure calculations give the values for the  $Mn_1$  ion  $m_S = 4.527 \mu_B$ ,  $m_L = 0.002 \mu_B$ , for the  $Mn_2$  ion  $m_S = -4.628 \mu_B$  and  $m_L = -0.003 \mu_B$ . The Mn spin moment are in good agreement with the result of VASP calculations  $m_S = 4.57 \mu_B$  [130].

The sum rules yield much smaller Mn spin moments  $m_S = 0.733 \mu_B$  at 5 K and  $m_S = 0.558 \mu_B$  at 25 K (above  $T_N$ ) [110]. One should mention that XMCD technique are not able to measure the separate contributions from different Mn sites. Therefore, the sum rules provide averaged Mn spin magnetic moment. For the AFM ordering and equivalent Mn sites one would expect zero averaged Mn spin moment. The imbalance in the Mn spin moments might be from several reasons: crystal imperfections (mostly due to the oxygen vacancies), nonequivalent  $Mn_1$  and  $Mn_2$  sites due to different coordinations (tetrahedral at  $Mn_1$  sites and pseudosquare planar at  $Mn_2$ ), and influence of the external magnetic field used in the experimental measurements

Table 4.2. The theoretically calculated spin  $m_S$ , orbital  $m_L$ , and total magnetic moments (in  $\mu_B$ ) of  $CaMnTi_2O_6$ .

Atom	$m_S$	$m_L$	$m_{tot}$
$Ca_1$	-0.003	0.0	-0.003
$Ca_2$	0.002	0.0	0.002
$Mn_1$	4.527	0.002	4.597
$Mn_2$	-4.628	-0.003	-4.631
Ti	0.018	-0.001	0.017
$O_1$	0.010	0.0	0.010
$O_2$	0.013	0.0	0.013
$O_3$	0.005	0.0	0.005
$O_4$	0.015	0.0	0.015
$O_5$	-0.017	0.0	-0.017

(6 T) [110]. Current theoretical calculations produce smaller magnetic imbalance of  $0.101 \mu_B$  because we take into account only non-equivalency of the  $Mn_1$  and  $Mn_2$  sites.

The experimentally estimated Mn orbital moment  $m_L$  was found to be equal to  $0.026 \mu_B$  at 5 K and  $0.003 \mu_B$  at 25 K. Both of these values are larger than the theoretical results (see Table 4.2). Again, this discrepancy is due to the imperfection of sum rules. The application of the sum rules for the theoretically calculated XA and XMCD spectra produces much larger orbital magnetic moments ( $-0.033 \mu_B$  and  $0.007 \mu_B$  at the  $Mn_1$

and Mn<sub>2</sub> sites, respectively) with better agreement with the experimental data.

The induced spin magnetic moments at the O<sub>1</sub> to O<sub>4</sub> sites are aligned along the *c* axis and are varied from 0.005  $\mu_B$  for the O<sub>3</sub> site to 0.015  $\mu_B$  for O<sub>4</sub>. Spin magnetic moments at the O<sub>5</sub> sites (which are the first neighbors for the Mn<sub>2</sub> ions) are AF ordered to other oxygens and possess largest spin magnetic moment of -0.017  $\mu_B$ . The orbital moments at the oxygen sites and are not excited 0.001  $\mu_B$ .

#### 4.1.3 XA and XMCD spectra

**Ti L<sub>2,3</sub> XA and XMCD spectra.** Figure 4.3 (upper panel) shows the XA spectra (open circles) at the Ti L<sub>2,3</sub> edges in CaMnTi<sub>2</sub>O<sub>6</sub> measured at 5 K [110] with a 6 T magnetic field applied along the *c* axis compared with the theoretically calculated ones in the GGA+*U*. The experimentally measured Ti L<sub>2,3</sub> XA spectra consist of four major peaks in

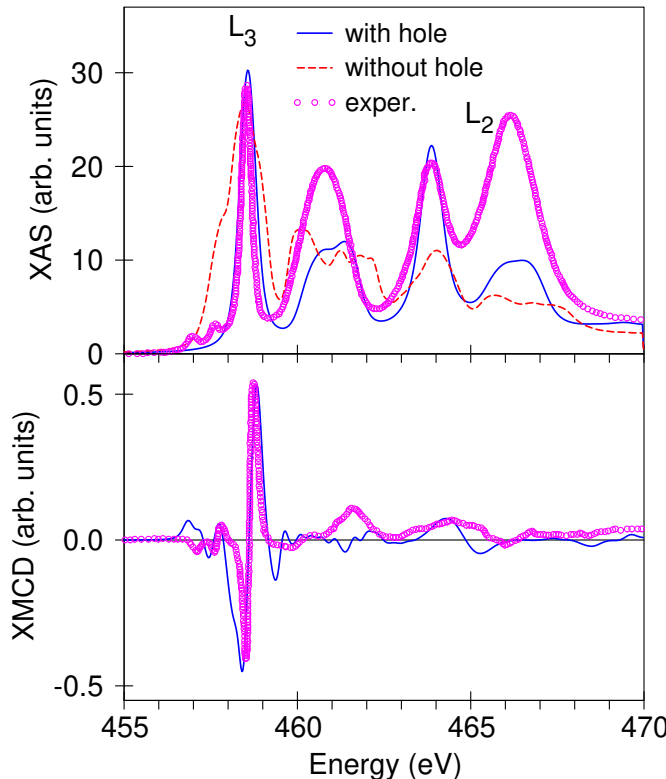


Figure 4.3. Top panel: the XA spectra (open circles) at Ti L<sub>2,3</sub> edges in CaMnTi<sub>2</sub>O<sub>6</sub> measured at 5 K [110] with a 6 T magnetic compared with the theoretically calculated ones with taking into account of core-hole effect (full blue curves) or the without core-hole effect (dashed red curves). Lower panel: the XMCD experimental spectra (open circles) of CaMnTi<sub>2</sub>O<sub>6</sub> at the Ti L<sub>2,3</sub> edges and the theoretically calculated one (full blue line) with taking into account core-hole effect.

the range of 457–469 eV. The two peaks with lower energy are Ti L<sub>3</sub> edge while the two peaks with higher energy are Ti L<sub>2</sub> edges. The Ti<sup>4+</sup> cation is in octahedral coordination with oxygen where the local octahedron gets elongated along the *c* axis in CaMnTi<sub>2</sub>O<sub>6</sub>. It is well known that when the Ti ion is octahedrally coordinated, the two peaks of Ti L<sub>3</sub> and L<sub>2</sub> will split into two main separate peaks *e*<sub>g</sub> and *t*<sub>2g</sub> [247]. The separation between these two main peaks is associated with the crystal-field splitting modified by the exchange interaction. Because the SO splitting of the core Ti 2p level ( $\Delta E_{SO} = 5.74$  eV) and the Ti 3d crystal-field splitting modified by the exchange interaction ( $\Delta E_{CF} = 3.3$  eV) are

of the same order of magnitude the  $L_3$  and  $L_2$  XA spectra are strongly overlapped. The four experimentally observed intense peaks from 457 eV to 469 eV can be, to a first approximation, assigned to  $2p_{3/2} \rightarrow e_g$ ,  $2p_{3/2} \rightarrow t_{2g}$ ,  $2p_{1/2} \rightarrow e_g$ , and  $2p_{1/2} \rightarrow t_{2g}$  transitions, respectively. However, the  $2p_{1/2} \rightarrow e_g$  and  $2p_{1/2} \rightarrow t_{2g}$  transitions ( $L_2$  spectrum) contribute also to the two low energy peaks. The theory reproduces the energy position of all the fine structures quite well, however, does not reproduce the experimentally observed  $L_3/L_2$  XA ratio. It is well known that the  $L_2$  and  $L_3$  XA channels in early  $3d$  transition metals with nearly empty  $d$  bands are strongly coupled through the photoelectron-core-hole Coulomb and exchange interactions [214, 243, 248, 249]. This leads to a branching ratio close to 1:1, far from the statistical ratio 2:1, which is obtained in the single-particle theory, unless the SO interaction in the final  $3d$  band is considered. From the band structure calculations the  $L_3/L_2$  branching ratio equals to 1.65 which is far from the experimentally observed. The core hole interactions significantly improve the agreement between theoretically calculated and experimentally measured Ti  $L_{2,3}$  XA spectra in CaMnTi<sub>2</sub>O<sub>6</sub> [see Fig. 4.3 (upper panel)]. Taking into account the core-hole effect the  $L_3/L_2$  branching ratio equals 1.2 with much better agreement with the experiment.

In spite of the nominally nonmagnetic character of Ti<sup>4+</sup> ( $d^0$ ), there are induced spin and orbital magnetic moments at the Ti sites due to the hybridization between Ti  $d$  states and Mn  $d$  states in CaMnTi<sub>2</sub>O<sub>6</sub> (see Table 4.2). The experimental measurements recorded a tiny XMCD signal under the application of a large magnetic field [110]. The XMCD spectra at the Ti  $L_3$  and  $L_2$  edges show quite complicated shapes with several negative and positive peaks. The GGA+ $U$  approach with taking into account core-hole effect reasonably well reproduces the shape of two major peaks at the  $L_3$  edge in the 457–459 eV energy interval as well as at the  $L_2$  at 464.5 eV. Other features are reproduced with less accuracy, however, it is hard to achieve ideal agreement with the experimental measurements with such tiny detected XMCD signal.

**Mn  $L_{2,3}$  XA and XMCD spectra.** Figure 4.4 (upper panel) shows the XA spectra (open circles) at Mn  $L_{2,3}$  edges in CaMnTi<sub>2</sub>O<sub>6</sub> measured at 5 K [110] with a 6 T magnetic field applied along the  $c$  axis compared with the theoretically calculated ones in the

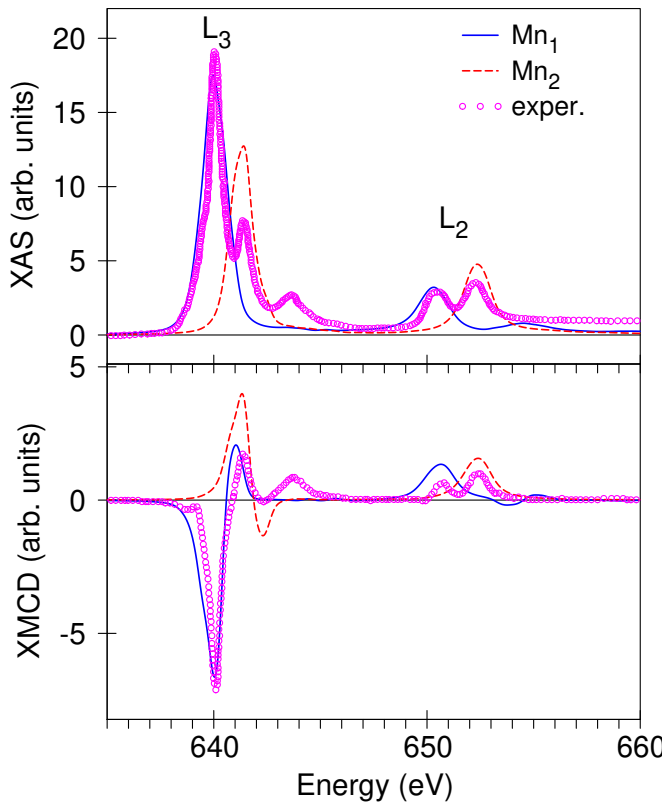


Figure 4.4. Top panel: the XA spectra (open circles) at Mn  $L_{2,3}$  edges in  $\text{CaMnTi}_2\text{O}_6$  [110] compared with the theoretically calculated ones for the  $\text{Mn}_1$  site (full blue line) and for the  $\text{Mn}_2$  site (dashed red line); lower panel: the XMCD experimental spectra (open circles) of  $\text{CaMnTi}_2\text{O}_6$  at the Mn  $L_{2,3}$  edges and the theoretically calculated ones for the  $\text{Mn}_1$  site (full blue line) and for the  $\text{Mn}_2$  site (dashed red line).

Therefore, the contribution from the substitutional  $\text{Mn}_2$  ions with higher ionicity are situated at higher energies and responsible for the high energy shoulder at 641.5 eV.

The lower panel of Fig. 4.4 presents the XMCD experimental spectra (open circles) of  $\text{CaMnTi}_2\text{O}_6$  at the Mn  $L_{2,3}$  edges and the theoretically calculated one for the  $\text{Mn}_1$  site (full blue line) and for the  $\text{Mn}_2$  site (dashed red line). The GGA+ $U$  calculations reproduce all the fine structures of the experimental Mn  $L_{2,3}$  XMCD spectra quite well except for the high-energy positive peak at around 644 eV, which probably has satellite nature (Fig. 4.4). The theory also overestimates the intensity of the positive and negative peaks at 641.5 eV and 642.5 eV. These structures are due to transitions from the  $2p$  core level to partially filled majority-spin  $3d$  states at the  $\text{Mn}_2$  site. Such the disagreements may be explained by the fact that our calculations presented in Fig. 4.4 have been done

GGA+SO+ $U$ . The Mn  $L_3$  XA spectrum possesses four fine structures: major peak at 640 eV, tiny low energy shoulder at 637.8 eV, and two high energy peaks at 641.5 eV and 644 eV. The theory reproduces the energy position and intensity of the major peak and shoulder at 637.8 eV quite well but fails to describe the high energy peak at 644 eV, which likely has satellite nature.

As was mentioned above, the  $\text{Mn}_1$  and  $\text{Mn}_2$  ions possess valence of 1.9+ and 2.2+, respectively. It is well known that as the valence changes from  $\text{Mn}^{2+}$  to  $\text{Mn}^{3+}$  and to  $\text{Mn}^{4+}$  states, the  $L_3$  XA spectrum shows a shift toward higher energy, and the spectral shape changes with the number of  $3d$  electrons [149].

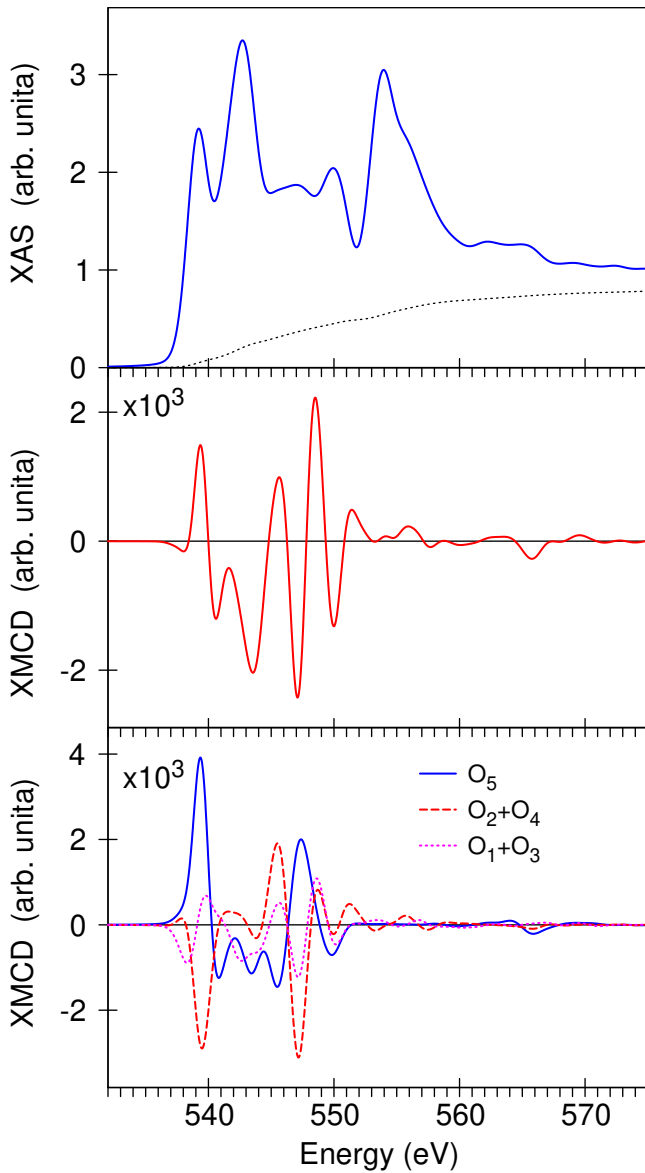


Figure 4.5. The theoretically calculated XA (top panel) and XMCD spectra (middle panel) together with contributions from different oxygen sites (lower panel) at the O *K* edge in  $\text{CaMnTi}_2\text{O}_6$ .

edge in various transition metal oxides [246]. The O *K* XMCD spectrum possesses quite complicated structure with several minima and maxima. The lower panel shows the partial contributions from different oxygen sites to the O *K* XMCD spectrum. The largest contribution comes from the first neighbors for the  $\text{Mn}_2$  ions, namely,  $\text{O}_5$  ions which possess largest spin and orbital moments. The  $\text{Mn}_2$  ions are surrounded by two  $\text{O}_2$  and two  $\text{O}_4$  ions. The induced spin magnetic moments at the  $\text{O}_2$  and  $\text{O}_4$  sites are aligned opposite to the  $\text{O}_5$  spin momenta (see Table 4.2). As a result, the XMCD signal from the  $\text{O}_2$  and  $\text{O}_4$  sites has an opposite sign to the  $\text{O}_5$  ones reducing significantly sum x-ray dichroism at the O *K* edge.

for ideal crystal structure without possible lattice imperfections and without external magnetic field. The external magnetic field (6 T in Ref. [110]) might change the spin orientation of some part of  $\text{Mn}_2$  ions, as result, the sum XMCD signal from the  $\text{Mn}_2$  sites will be reduced. This is in consistent with strong imbalance of spin magnetic moments between nonequivalent  $\text{Mn}_1$  and  $\text{Mn}_2$  sites observed experimentally [110].

We found that the core-hole effect has a small influence on the shape of the XA and XMCD spectra at the Mn  $L_{2,3}$  edges.

#### XA and XMCD spectra at O *K* edge.

Figure 4.5 presents the theoretically calculated XA (top panel) and XMCD (middle panel) spectra for  $\text{CaMnTi}_2\text{O}_6$  at the O *K* edge. The O *K* XA spectrum extends on more than 40 eV and has the fine structures typical for the oxygen *K* XA

. The dichroism at the O *K* edge is very small. The O *K* XMCD spectrum has the fine structure with several minima and maxima. The lower panel shows the partial contributions from different oxygen sites to the O *K* XMCD spectrum. The largest contribution comes from the first neighbors for the  $\text{Mn}_2$  ions, namely,  $\text{O}_5$  ions which possess largest spin and orbital moments. The  $\text{Mn}_2$  ions are surrounded by two  $\text{O}_2$  and two  $\text{O}_4$  ions. The induced spin magnetic moments at the  $\text{O}_2$  and  $\text{O}_4$  sites are aligned opposite to the  $\text{O}_5$  spin momenta (see Table 4.2). As a result, the XMCD signal from the  $\text{O}_2$  and  $\text{O}_4$  sites has an opposite sign to the  $\text{O}_5$  ones reducing significantly sum x-ray dichroism at the O *K* edge.

## 4.2 CaCo<sub>3</sub>V<sub>4</sub>O<sub>12</sub>

The original results discussed in this Section are published in [5].

### 4.2.1 Crystal structure and details of calculations

The crystal structure of CaCo<sub>3</sub>V<sub>4</sub>O<sub>12</sub> (Fig. 4.6) can be considered as a variant of the cubic perovskite oxide ABO<sub>3</sub>. The superstructure AA'<sub>3</sub>B<sub>4</sub>O<sub>12</sub>, with space group  $Im\bar{3}$  (No. 204), is formed by quadrupling the parent unit cell and replacing 3/4 of the element A with A'. Due to the introduction of A', the symmetry of the structure is lowered by a large rotation of the BO<sub>6</sub> octahedra, which brings four oxygen ions closer to the A' (Co) site to form a seemingly nearly square-planar environment. This particular quadruple perovskite houses VO<sub>6</sub> octahedra that are virtually regular: all V-O distances are identical, and the O-V-O angles deviate from 90° by only 0.04° [131]. The CoO<sub>4</sub> plaquettes are not as regular, with the O-Co-O angles being 93.6°

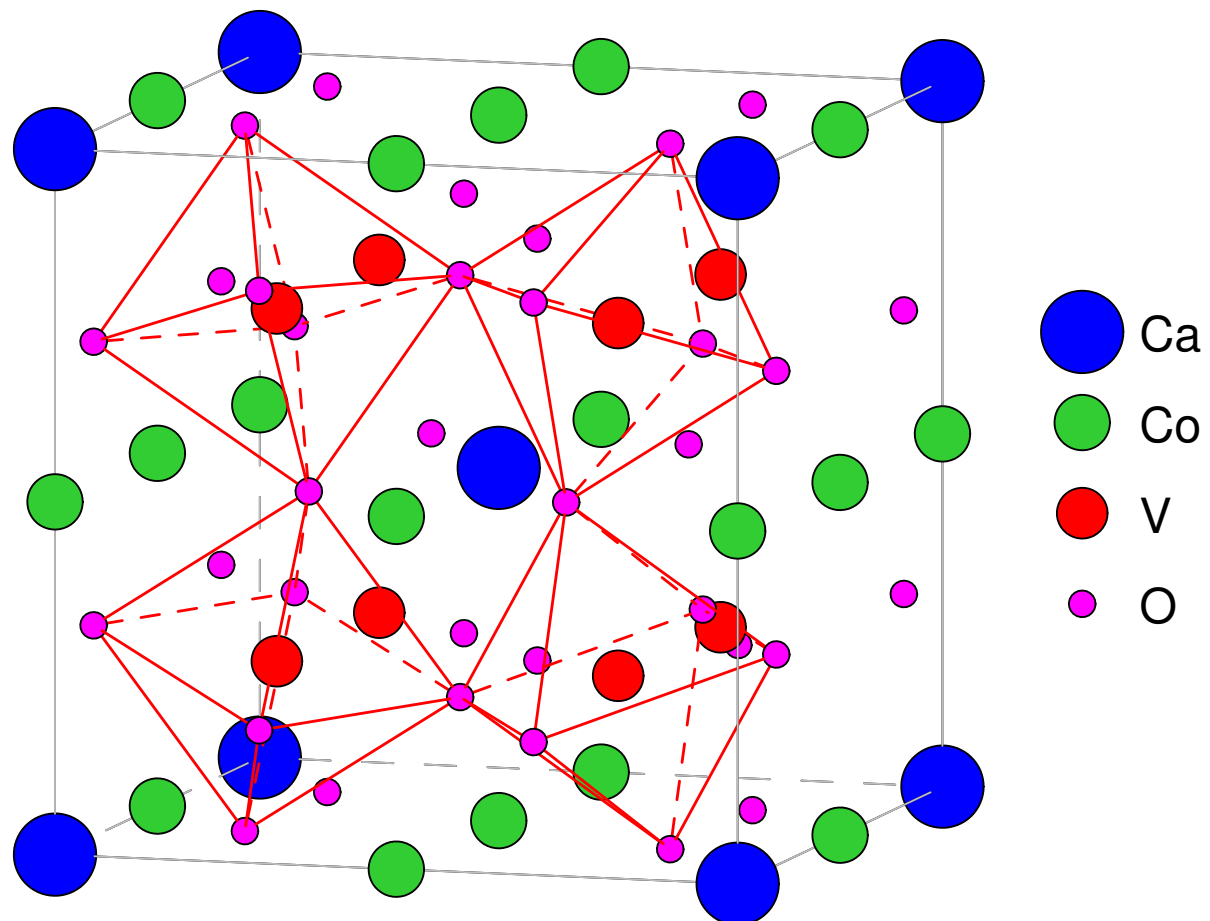


Figure 4.6. The crystal structure of CaCo<sub>3</sub>V<sub>4</sub>O<sub>12</sub>. There is square-planar oxygen coordination of the Co<sup>2+</sup> ions occupying the A' sites and the octahedral network of V<sup>4+</sup> ions.

Table 4.3. Atomic positions of  $\text{CaCo}_3\text{V}_4\text{O}_{12}$  used in the band structure calculations. Lattice parameter is  $a = 7.3428 \text{ \AA}$  [131].

Atom	Site	<i>x</i>	<i>y</i>	<i>z</i>
Ca	$2a$	0	0	0
Co	$6b$	0	0.5	0.5
V	$8c$	0.25	0.25	0.25
O	$24g$	0	0.299	0.8115

The crystal structure parameters of  $\text{CaCo}_3\text{V}_4\text{O}_{12}$  are presented in Table 4.3.

In the calculations the intrashell Coulomb repulsion  $U$  and interorbital Hund magnetic coupling  $J$  are applied to both Co and V sites:  $U_{\text{Co}} = 5 \text{ eV}$ ,  $J_{\text{Co}} = 1 \text{ eV}$ ,  $U_{\text{V}} = 3.4 \text{ eV}$ ,  $J_{\text{V}} = 0.7 \text{ eV}$ . Similar parameters were used by Rhee and Pickett [250].

#### 4.2.2 Electronic band structure

Since the experimental evidence suggests the AFM order in  $\text{CaCo}_3\text{V}_4\text{O}_{12}$  [131], the energy band structure of this double perovskite is obtained in the AFM state with and without taking into account the SOC. The results are shown in Fig. 4.7. The collinear AFM  $\text{CaCo}_3\text{V}_4\text{O}_{12}$  ground state within GGA [Fig. 4.7 (a, b)] as well as GGA+SO [Fig. 4.7 (c)] is metallic. This contradicts with the electrical resistivity data which suggest semiconducting behavior in the temperature range of 1.6–370 K [131]. Adding an on-site Coulomb repulsion on each of the Co and V ions results in a Mott insulator electronic structure of  $\text{CaCo}_3\text{V}_4\text{O}_{12}$  (see the lower panel of Fig. 4.7). The energy band gap is rather small and equal to 0.109 eV at the  $\Gamma$  symmetry point.

The crystal field at the Co sites ( $D_{2h}$  point symmetry) causes the splitting of Co  $3d$  orbitals into five singlets ( $d_{xz}$ ,  $d_{xy}$ ,  $d_{yz}$ ,  $d_{3z^2-1}$ , and  $d_{x^2-y^2}$ ). The V site possesses the  $C_3$  point symmetry and V  $3d$  states split into one singlet  $a$  (the combination of  $d_{xz}$ ,  $d_{xy}$ ,  $d_{yz}$  orbitals) and two doublets ( $d_{3z^2-1}$ ,  $d_{x^2-y^2}$ , and combination of  $d_{xz}$ ,  $d_{xy}$ ,  $d_{yz}$ ).

Both the  $\text{Co}^{2+}$  and  $\text{V}^{4+}$  ions in  $\text{CaCo}_3\text{V}_4\text{O}_{12}$  are expected to be magnetic and Mott insulating, and carry a substantial orbital moment to account for the observed Curie-Weiss moments. The calculations reveal that the Mott insulating character of

and  $86.4^\circ$ . The V ions separated by  $a/2$  lie on a simple cubic sublattice, while the Co ions lie on a *bcc* sublattice with the same nearest-neighbor Co-Co distance. The two perovskite A and B sublattices form a CsCl configuration, making it likely that nearest-neighbor Co-V exchange interactions (versus Co-Co or V-V) are the driving force for the magnetic order [250].

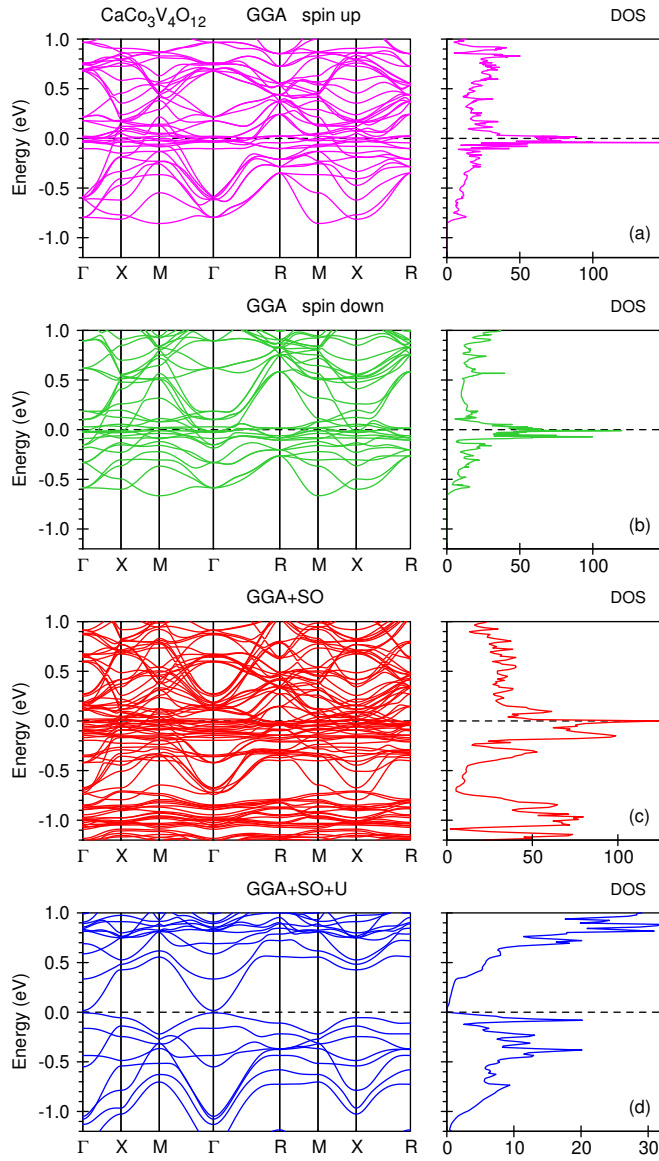


Figure 4.7. The energy band structure and total DOS [in states/(cell eV)] of AFM  $\text{CaCo}_3\text{V}_4\text{O}_{12}$  calculated in GGA (a and b), GGA+SO (c), and GGA+SO+ $U$  (d).

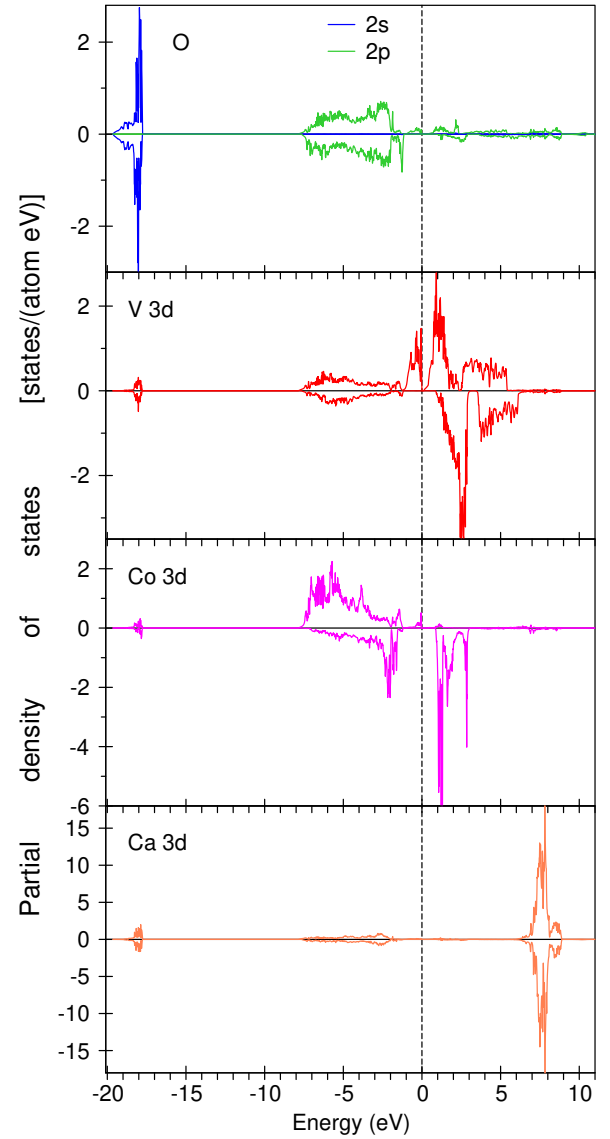


Figure 4.8. The partial DOS [in states/(atom eV)] of AFM  $\text{CaCo}_3\text{V}_4\text{O}_{12}$  calculated in GGA+SO+ $U$ .

the open-shell Co ions arises mostly through the  $d_{3z^2-1}$  orbital with a small amount of  $d_{x^2-y^2}$  (see Fig. 4.9). The partial DOS of V ions is relatively small at the  $E_F$ .

The  $\text{Co}^{2+}$  ions in the electronic configuration  $t_{2g}^5 e_g^2$  are situated in the rectangular  $\text{CoO}_4$  plaquettes, so one would expect a large Co orbital moment. From magnetic susceptibility [131] and neutron diffraction measurements of  $\text{CaCo}_3\text{V}_4\text{O}_{12}$  the authors of Ref. [127] suggest that the Co orbital moment has to exceed  $1 \mu_B$ . The band structure calculations confirm this suggestion. The spin and orbital magnetic moments for the  $\text{Co}_1$  atom are  $m_S = 2.606 \mu_B$ ,  $m_L = 1.227 \mu_B$ , for the  $\text{Co}_2$  they are  $m_S = -2.524 \mu_B$  and

Table 4.4. The theoretically calculated (in  $\mu_B$ ) spin  $m_S$ , orbital  $m_L$ , and total  $m_{\text{tot}}$  magnetic moments in  $\text{CaCo}_3\text{V}_4\text{O}_{12}$ .

Atom	$m_S$	$m_L$	$m_{\text{tot}}$
Ca <sub>1</sub>	0.009	0.018	0.027
Ca <sub>2</sub>	0.004	0.021	0.025
Co <sub>1</sub>	2.606	1.227	3.833
Co <sub>2</sub>	-2.524	-1.189	-3.713
V	1.037	-0.309	0.728
O <sub>1</sub>	0.010	-0.007	0.003
O <sub>2</sub>	-0.065	-0.008	-0.073

be equal to  $-0.007 \mu_B$  and  $-0.008 \mu_B$  for the O<sub>1</sub> and O<sub>2</sub> sites, respectively (see Table 4.4).

Figure 4.8 presents the partial DOS for  $\text{CaCo}_3\text{V}_4\text{O}_{12}$ . The O 2s states are located mostly between  $-19.6 \text{ eV}$  and  $-17.8 \text{ eV}$ . The O 2p states are situated from  $-7.9 \text{ eV}$  to  $-1.9 \text{ eV}$ , however, a small amount of them appears between  $-1.9 \text{ eV}$  and  $-1.1 \text{ eV}$  as well as from  $-1.0 \text{ eV}$  to  $E_F$  due to their hybridization with the Co and V 3d valence states, respectively. The spin splitting of the oxygen 2p states is quite small (around 0.2 eV). The V 3d states are situated from  $-1.2 \text{ eV}$  to 0 and from  $0.1 \text{ eV}$  to  $5.4 \text{ eV}$  above  $E_F$  in the majority spin channel. The spin-down V states are mostly empty and occupy the energy interval from  $0.9 \text{ eV}$  up to  $6.3 \text{ eV}$ . There are some V 3d occupied states from  $-7.8 \text{ eV}$  to  $-1.2 \text{ eV}$  due to their hybridization with the oxygen 2p valence states. The spin-up

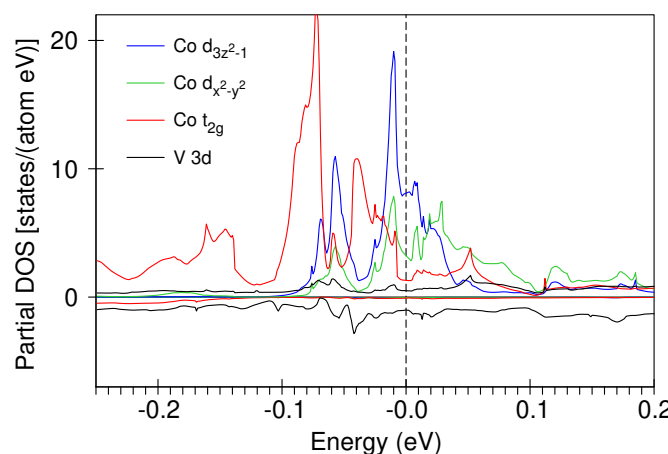


Figure 4.9. The symmetry resolved partial DOS [in states/(atom eV)] of AFM  $\text{CaCo}_3\text{V}_4\text{O}_{12}$  calculated in GGA.

$m_L = -1.189 \mu_B$ . The spin and orbital magnetic moments at the V site are equal to  $m_S = 1.036 \mu_B$  and  $m_L = -0.308 \mu_B$ . The Co spin and orbital moments are parallel and the magnetic moments of V are antiparallel that agrees with Hund's third rule.

The Ca spin and orbital magnetic moments are small for both sites. The induced spin magnetic moments at the O<sub>1</sub> and O<sub>2</sub> sites equal  $0.010 \mu_B$  and  $-0.065 \mu_B$ , respectively. The orbital magnetic moments are found to

be equal to  $-0.007 \mu_B$  and  $-0.008 \mu_B$  for the O<sub>1</sub> and O<sub>2</sub> sites, respectively (see Table 4.4).

Co 3d states are situated between  $-7.8 \text{ eV}$  and  $-1.2 \text{ eV}$  below  $E_F$ . There is a small peak in the close vicinity of the  $E_F$  in the Co 3d states due to their hybridization with V 3d states. The Co 3d spin-down states occupy the energy interval from  $-7.1 \text{ eV}$  to  $-1.5 \text{ eV}$  and from  $0.8 \text{ eV}$  up to  $3 \text{ eV}$ . The Ca 3d empty states occupy the  $6.2\text{--}8.9 \text{ eV}$  energy interval.

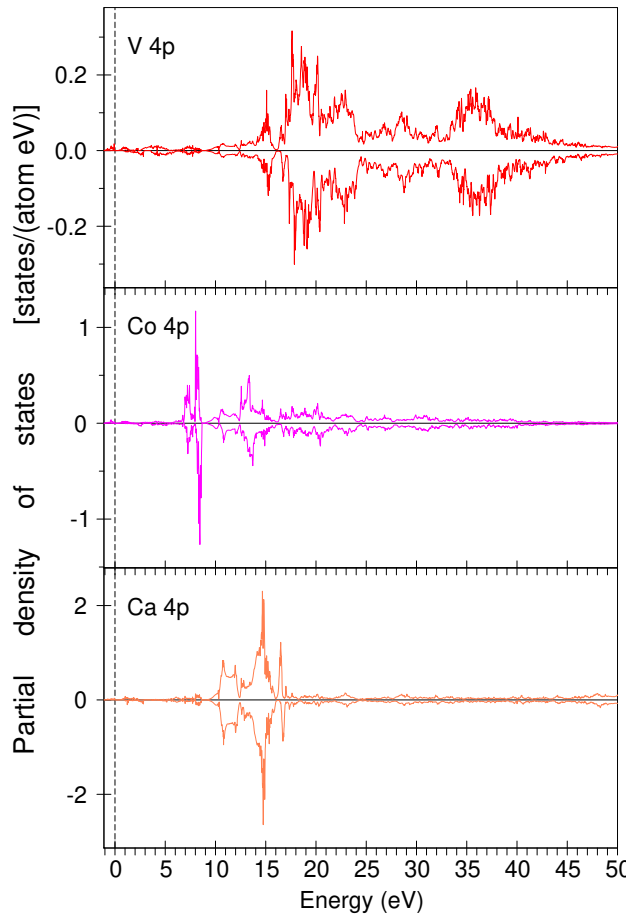


Figure 4.10. The partial  $4p$  DOS [in states / (atom eV)] of AFM  $\text{CaCo}_3\text{V}_4\text{O}_{12}$  calculated in GGA+SO+ $U$ .

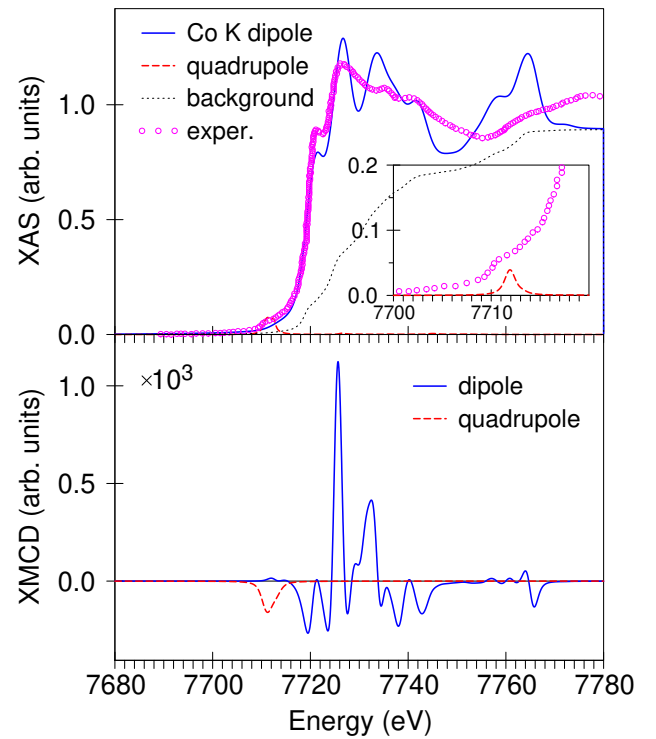


Figure 4.11. Top panel: the experimental XA spectrum (open circles) at the  $\text{Co } K$  edge in  $\text{CaCo}_3\text{V}_4\text{O}_{12}$  measured at 70 K [127] in comparison with the theoretically calculated one. The dotted black curve shows the background spectrum. Lower panel: the theoretically calculated XMCD of  $\text{CaCo}_3\text{V}_4\text{O}_{12}$  at the  $\text{Co } K$  edge. The dashed red curve shows the quadrupole contributions to the spectra.

#### 4.2.3 XA and XMCD spectra

XA and XMCD spectra in metals and alloys at the  $K$  edge when the  $1s$  core electrons are excited to empty  $p$  states in the dipole transitions are important since they are sensitive to the electronic states at neighboring sites because of the delocalized nature of  $p$  states.

Figure 4.10 presents the partial  $4p$  DOSs of Ca, Co, and V ions in  $\text{CaCo}_3\text{V}_4\text{O}_{12}$  above the  $E_F$  calculated in the GGA+SO+ $U$  for the AFM ordering. The  $4p$  DOS in the close vicinity of the  $E_F$  are quite small. The first peak of  $4p$  DOS starts at 6.8 eV, 10.2 eV, and 12.5 eV for Co, Ca, and V, respectively. The V  $4p$  DOS is the smallest and the one for Ca  $4p$  is the largest. All the partial DOSs are extended far above the  $E_F$ .

The upper panels of Fig. 4.11, 4.12, and 4.13 show the XA spectra (open circles) at the Co, V, and Ca  $K$  edges in  $\text{CaCo}_3\text{V}_4\text{O}_{12}$  measured at 70 K [127] in comparison with the theoretically calculated ones (full blue lines) in the GGA+SO+ $U$ . The Co  $K$  XA

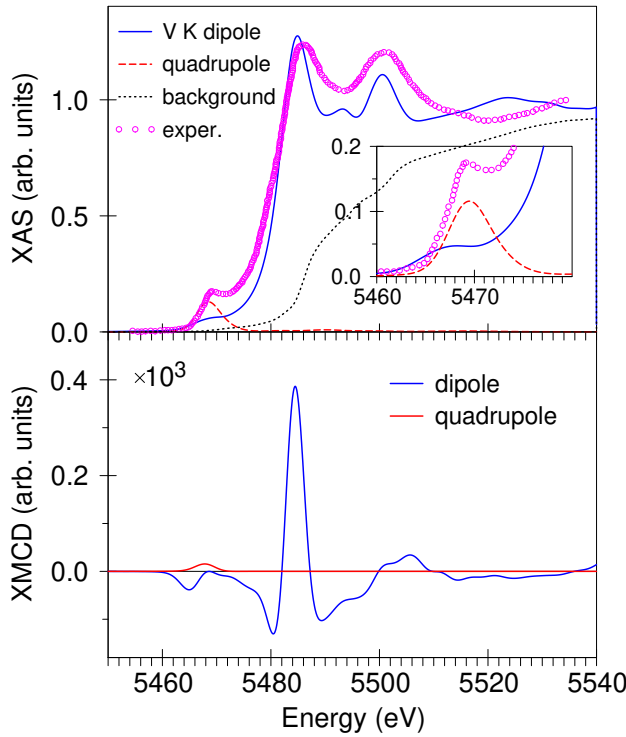


Figure 4.12. Top panel: the experimental XA spectrum (open circles) at the  $V\ K$  edge in  $\text{CaCo}_3\text{V}_4\text{O}_{12}$  measured at 70 K [127] in comparison with the theoretically calculated one. The dotted black curve shows the background spectrum. Lower panel: the theoretically calculated XMCD of  $\text{CaCo}_3\text{V}_4\text{O}_{12}$  at the  $V\ K$  edge. The dashed red curve shows the quadrupole contributions to the spectra.

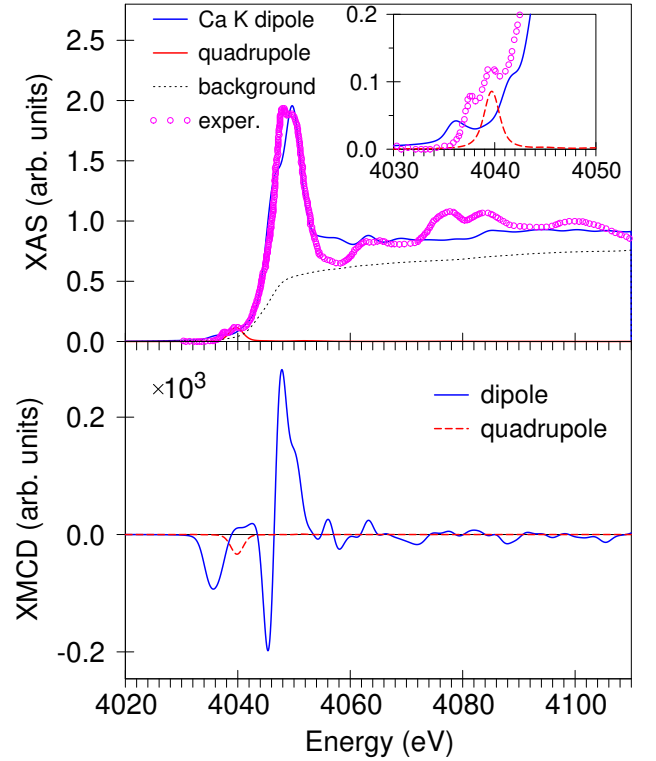


Figure 4.13. Top panel: the experimental XA spectrum (open circles) at the  $\text{Ca}\ K$  edge in  $\text{CaCo}_3\text{V}_4\text{O}_{12}$  measured at 70 K [127] in comparison with the theoretically calculated one. The dotted black curve shows the background spectrum. Lower panel: the theoretically calculated XMCD of  $\text{CaCo}_3\text{V}_4\text{O}_{12}$  at the  $\text{Ca}\ K$  edge. The dashed red curve shows the quadrupole contributions to the spectra.

spectrum possesses a major peak at 7726 eV with a low energy shoulder at 7721 eV, two small high energy shoulders at 7735 eV and 7742 eV, and a high energy fine structure at 7778 eV (see Fig. 4.11). The theory reproduces the energy position of the major peak and the low and high energy shoulders quite well but fails to describe correctly the position of the high energy peak at 7778 eV. The Co  $K$  XA spectrum is extended over a very large interval up to 75 eV above the edge, and it is difficult to expect that a linear energy band structure method can describe the spectrum in such a large interval.

The  $V\ K$  XA spectrum possesses two major peaks at 5485 eV and 5502 eV and a low energy prepeak at 5470 eV being discussed later (see Fig. 4.12). The theory reproduces well the energy position of two major peaks. Like in the case of Co  $K$  XA spectrum, the theory does not reproduce the energy position of the fine structure above 5530 eV.

The  $\text{Ca}\ K$  XA spectrum possesses a two-peak fine structure at around 4049 eV and

several small peaks between 4060 eV and 4120 eV (see Fig. 4.13). The theory reproduces well the energy position of this two-peak structure, however, with inverse intensities of the peaks. The calculations give the larger intensity for the high energy peak but the experiment shows the larger intensity for the low energy peak. The structure of Ca  $K$  XA spectrum reflects the energy distribution of the corresponding Ca  $4p$  partial DOS (see the lower panel of Fig. 4.10). There are two peaks at the partial DOS at 12 eV and 15 eV above the  $E_F$  which produce the major two-peak structure in Ca  $K$  XA spectrum.

The effect of the electric quadrupole  $E_2$  and magnetic dipole  $M_1$  transitions on the XA and XMCD spectra at the transition metal  $K$  edges is also investigated. The  $M_1$  transitions are extremely small in comparison with the  $E_2$  transitions and can be neglected. The  $E_2$  transitions indeed contribute to the low energy XA spectra. Such transitions are responsible for the pre-peak structures of all three  $K$  XA spectra shown in the inserts of Figs. 4.11, 4.12, and 4.13. The smallest  $E_2$  contribution is found for the Co  $K$  XA spectrum and the largest one for V  $K$  XA one. The pre-peak in the Ca  $K$  XA spectrum has a two-peak structure with the lower energy peak due to the dipole  $E_1$  transitions and the higher energy one due to the quadrupole  $E_2$  transitions (see the insert of Fig. 4.13).

The lower panels of Fig. 4.11, 4.12, and 4.13 the XMCD spectra at the Co, V, and Ca  $K$  edges are shown, respectively. The exchange splitting of the initial  $1s$ -core state is extremely small [251], therefore only the exchange and spin-orbit splitting of the final  $2p$  states is responsible for the observed dichroism at the transition metal  $K$  edge. For this reason the dichroism is found to be very small, at least three orders of magnitude smaller than the maximum of XA spectrum. The Co, V, and Ca  $K$  XMCD spectra possess quite complicated structures with several minima and maxima. The largest contributions are found to come from the energy regions of the corresponding  $3d$  states. The contributions of the quadrupole  $E_2$  transitions to the XMCD spectra are one order of magnitude smaller than the dipole  $E_1$  transitions, hence, four orders of magnitude smaller than the intensity of the corresponding  $K$  XA spectra. Therefore, the detection of the quadrupole transitions in the XMCD spectra of these  $3d$   $K$  spectra is very close to impossible.

### 4.3 Conclusions for Chapter 4

The electronic band structure and XMCD spectra in CaMnTi<sub>2</sub>O<sub>6</sub> and CaCo<sub>3</sub>V<sub>4</sub>O<sub>12</sub> have been investigated theoretically within a DFT GGA+*U* approach in the framework of the SPR LMTO band-structure method.

In CaMnTi<sub>2</sub>O<sub>6</sub> A-site Mn<sup>2+</sup> ions stay in high-spin state 3*d*<sup>5</sup> and exhibit long-range *C* type AFM order. Different Mn<sub>1</sub> and Mn<sub>2</sub> ions possess different valencies 1.9+ and 2.2+, and different magnetic moments 4.527  $\mu_{\text{B}}$  and -4.628  $\mu_{\text{B}}$ . The shapes of the 3*d* partial DOSs are also differ from each other. Due to the AFM ordering and different coordinations (tetrahedral at Mn<sub>1</sub> sites and pseudosquare planar at Mn<sub>2</sub>) the XMCD spectra at the Mn *L*<sub>3</sub> edge have opposite signs and are shifted to each other producing the spectrum with major peak at 640 eV and two high energy shoulders at 641.5 eV and 644 eV. The core-hole effect was found to be small influence on the shape of the XA and XMCD spectra at the Mn *L*<sub>2,3</sub> and O *K* edges, however, it significantly improves the agreement between the theory and experiment at the Ti *L*<sub>2,3</sub> edges.

CaCo<sub>3</sub>V<sub>4</sub>O<sub>12</sub> possesses the AFM ordering and semiconducting behavior at low temperature [131]. The Mott insulator state is reproduced in the calculations if an on-site Coulomb repulsion on the Co and V ions is added. The energy band gap is rather small and equal to 0.109 eV at the  $\Gamma$  symmetry point, and both the Co<sup>2+</sup> and V<sup>4+</sup> ions are magnetic. The Mott insulating character of the open-shell Co ions arises mostly through the  $d_{3z^2-1}$  orbital with a small amount of  $d_{x^2-y^2}$ . A substantial orbital moment over 1  $\mu_{\text{B}}$  at the Co site is caused by a specific crystal structure of the compound.

The dichroism has been found to be very small at the Co, V, and Ca *K* edges, at least three orders of magnitude smaller than the XA spectra since the exchange splitting of the initial 1*s*-core state is extremely small and only the exchange and spin-orbit splitting of the final 2*p* states is responsible for the observed dichroism at the *K* XA edges. It has been found the magnetic dipole *M*<sub>1</sub> contributions at the transition metal *K* edges are extremely small in comparison with the *E*<sub>2</sub> transitions and can be neglected. The *E*<sub>2</sub> transitions indeed contribute to the low energy part of x-ray spectra. Such transitions are responsible for the pre-peak structures of all three XA spectra at the *K* XA edge.

## CHAPTER 5

### CONCLUSIONS

**In the Chapter 3** it is shown that the presence of an oxygen vacancy located in the first neighborhood of the second substitutional atom, additional Zn atoms and the lattice relaxation are found to improve the agreement between the theory and the experiment. For the different dopants T in (Zn,T)O one needs to make additional assumptions in order to reproduce experimental x-ray spectra. For T = V one has to suggest the AFM ordering between the V ions situated at the largest possible distance between V atoms with different spin directions. For T = Mn and Co the main features of x-ray spectra are reproduced without any additional assumptions, with the oxygen vacancy being responsible for the double-peak structure of the Mn  $L_{2,3}$  spectra. For T = Fe one has to assume there exist Fe atoms in  $Fe^{2+}$  and  $Fe^{3+}$  valence states. While  $Fe^{3+}$  valence is the ground LSDA state, the  $Fe^{2+}$  one is reproduced in constrained LSDA+ $U$  only. Mixed valence state is responsible for double-peak structure of the Fe  $L_{2,3}$  spectra.

**In the Chapter 4** it is shown that in CaMnTi<sub>2</sub>O<sub>6</sub> A-site Mn<sup>2+</sup> ions stay in high-spin state  $3d^5$  and exhibit long-range C type AFM order. Different Mn<sub>1</sub> and Mn<sub>2</sub> ions possess different valencies 1.9+ and 2.2+, and different magnetic moments. Due to the AFM ordering and different local environment the XMCD spectra at the Mn<sub>1,2</sub>  $L_3$  edge have opposite signs and are shifted to each other producing the total spectrum with major peak accompanied by two high energy features. The core-hole effect significantly improves the agreement between the theory and experiment at the Ti  $L_{2,3}$  edges only.

The Mott insulator state in CaCo<sub>3</sub>V<sub>4</sub>O<sub>12</sub> is reproduced in the calculations if an on-site Coulomb repulsion on the Co and V ions is added. The direct energy band gap of 0.109 eV is opened at the  $\Gamma$  symmetry point and arises mostly through the Co  $d_{3z^2-1}$  orbital. A substantial orbital moment over 1  $\mu_B$  at the Co site is caused by a specific crystal structure of the compound. The dichroism is found to be very small at the Co, V, and Ca  $K$  edges since it arises only due to the exchange and spin-orbit splitting of the final  $2p$  states. The  $E_2$  transitions are responsible for the low energy pre-peak structures of all three XA spectra at the  $K$  XA edge. At this edge the magnetic dipole  $M_1$  contributions are extremely small as compared with  $E_2$  ones and can be neglected.

## BIBLIOGRAPHY

- [1] Antonov V. N. X-ray magnetic dichroism in the (Zn,Co)O diluted magnetic semiconductors from first principle calculations. / V. N. Antonov, L. V. Bekenov, O. Jepsen, **D. V. Mazur**, and L. P. Germash. // *J. Appl. Phys.* – 2012. – Vol. 111. – P. 073702.
- [2] Antonov V. N. X-ray Magnetic Dichroism in (Zn,Mn)O Diluted Magnetic Semiconductors: First-principles Calculations. / V. N. Antonov, L. V. Bekenov, **D. V. Mazur**, and L. P. Germash. // *J. Korean Phys. Soc.* – 2012. – Vol. 60. – P. 1915–1922.
- [3] Bekenov L. V. Electronic Structure and X-Ray Magnetic Circular Dichroism in (Zn,T)O (T = V, Fe, Co) Diluted Magnetic Semiconductors. / L. V. Bekenov, **D. V. Mazur**, V. N. Antonov, L. P. Germash, and A. Ernst. // *Metallofiz. Noveishie Tekhnol.* – 2013. – Vol. 35. – P. 11–17.
- [4] Antonov V. N. Electronic structure and x-ray magnetic circular dichroism in ferroelectric CaMnTi<sub>2</sub>O<sub>6</sub>. / V. N. Antonov, D. A. Kukusta, S. V. Moklyak, **D. V. Mazur**, and L. V. Bekenov. // *Phys. Rev. B.* – 2020. – Vol. 101. – P. 054441.
- [5] Mazur D. V. Electronic Structure and X-ray Magnetic Circular Dichroism in A-site ordered perovskite CaCo<sub>3</sub>V<sub>4</sub>O<sub>12</sub>. / **D. V. Mazur**, L. V. Bekenov, B. Kh. Zhuravlov, S. V. Mokliak, Yu. M. Kucherenko, and V. M. Antonov. // *Metallofiz. Noveishie Tekhnol.* – 2023. – Vol. 45. – P. 1067–1082.
- [6] Žutić Igor. Spintronics: Fundamentals and applications. / Igor Žutić, Jaroslav Fabian, and S. Das Sarma. // *Rev. Mod. Phys.* – 2004. – Vol. 76. – P. 323–410.
- [7] Antonov V. N. X-Ray Magnetic Dichroism in Diluted Magnetic Semiconductors: First-Principles Calculations. In: Jasmin Wallace, editor, *Circular and Linear Dichroism, Lasers and Electro-Optics Research and Technology* / V. N. Antonov and L. V. Bekenov. // *Nova Science Publishers, Inc.* – 2016. – P. 1–130.
- [8] Furdyna J. K. Diluted magnetic semiconductors. / J. K. Furdyna. // *J. Appl. Phys.* – 1988. – Vol. 64. – P. R29–R64
- [9] Sanvito Stefano. Density Functional Calculations for III-V Diluted Ferromagnetic Semiconductors: A Review. / Stefano Sanvito, Gerhard Theurich, and Nicola A.

- Hill. // *Journal of Superconductivity*. – 2002. – Vol. 15. – P. 85–104.
- [10] Jungwirth T. Theory of ferromagnetic (III,Mn)V semiconductors. / T. Jungwirth, Jairo Sinova, J. Mašek, J. Kučera, and A. H. MacDonald. // *Rev. Mod. Phys.* – 2006. – Vol. 78. – P. 809.
- [11] Ohno H. (Ga,Mn)As: A new diluted magnetic semiconductor based on GaAs. / H. Ohno, A. Shen, F. Matsukura, A. Oiwa, A. Endo, S. Katsumoto, and Y. Iye. // *Appl. Physics Lett.* – 1996. – Vol. 69. – P. 363–365.
- [12] Dietl T. Zener Model Description of Ferromagnetism in Zinc-Blende Magnetic Semiconductors. / T. Dietl, H. Ohno, F. Matsukura, J. Cibert, and D. Ferrand. // *Science*. – 2000. – Vol. 287. – P. 1019.
- [13] Ueda Kenji. Magnetic and electric properties of transition-metal-doped ZnO films. / Kenji Ueda, Hitoshi Tabata, and Tomoji Kawai. // *Appl. Physics Lett.* – 2001. – Vol. 79. – P. 988–990.
- [14] Liu C. Ferromagnetism of ZnO and GaN: A Review. / C. Liu, F. Yun, and H. Morkoç. // *J. Mater. Sci.: Mater. Electron.* – 2005. – Vol. 16. – P. 555–597.
- [15] Cao H.T. Preparation and characterization of Al and Mn doped ZnO (ZnO: (Al, Mn)) transparent conducting oxide films. / H.T. Cao, Z.L. Pei, J. Gong, C. Sun, R.F. Huang, and L.S. Wen. // *Journal of Solid State Chemistry*. – 2004. – Vol. 177. – P. 1480–1487.
- [16] Dietl T. Zener Model Description of Ferromagnetism in Zinc-Blende Magnetic Semiconductors. / T. Dietl, H. Ohno, F. Matsukura, J. Cibert, and D. Ferrand. // *Science*. – 2000. – Vol. 287. – P. 1019–1022.
- [17] Sato K. First principles materials design for semiconductor spintronics. / K. Sato and H. Katayama-Yoshida. // *Semicond. Sci. Technol.* – 2002. – Vol. 17. – P. 367.
- [18] Iuşan D. Influence of defects on the magnetism of Mn-doped ZnO. / D. Iuşan, B. Sanyal, and O. Eriksson. // *J. Appl. Phys.* – 2007. – Vol. 101. – P. 09H101.
- [19] Mounkachi O. Electronic structure of acceptor defects in (Zn,Mn)O and (Zn,Mn)(O,N). / O. Mounkachi, A. Benyoussef, A. El Kenz, E. H. Saidi, and E. K. Hlil. // *J. Appl. Phys.* – 2009. – Vol. 106. – P. 093905.
- [20] Uspenskii Yu. Ab initio study of the magnetism in GaAs, GaN, ZnO, and ZnTe-

- based diluted magnetic semiconductors. / Yu. Uspenskii, E. Kulatov, H. Mariette, H. Nakayama, and H. Ohta. // *J. Magn. Magn. Mater.* – 2003. – Vol. 258–259. – P. 248–250.
- [21] Karmakar Debjani. Electronic structure and magnetic properties of (Fe,Co)-codoped ZnO: Theory and experiment. / Debjani Karmakar, T. V. Chandrasekhar Rao, J. V. Yakhmi, A. Yaresko, V. N. Antonov, R. M. Kadam, S. K. Mandal, R. Adhikari, A. K. Das, T. K. Nath, Nirmal Ganguli, I. Dasgupta, and G. P. Das. // *Phys. Rev. B.* – 2010. – Vol. 81. – P. 184421.
- [22] Bekenov L. V. Electronic and magnetic properties of  $(\text{Zn}_{1-x}\text{V}_x)\text{O}$  diluted magnetic semiconductors elucidated from x-ray magnetic circular dichroism at  $\text{V } L_{2,3}$  edges and first-principles calculations. / L. V. Bekenov, V. N. Antonov, S. Ostainin, A. N. Yaresko, I. V. Maznichenko, W. Hergert, I. Mertig, and A. Ernst. // *Phys. Rev. B.* – 2011. – Vol. 84. – P. 134421.
- [23] Chanier T. LSDA + U versus LSDA: Towards a better description of the magnetic nearest-neighbor exchange coupling in Co- and Mn-doped ZnO. / T. Chanier, M. Sargolzaei, I. Opahle, R. Hayn, and K. Koepernik. // *Phys. Rev. B.* – 2006. – Vol. 73. – P. 134418.
- [24] Feng Xiaobing. Electronic structures and ferromagnetism of Cu- and Mn-doped ZnO. / Xiaobing Feng. // *J. Phys.: Condens. Matter.* – 2004. – Vol. 16. – P. 4251–4259.
- [25] Yan Wensheng. Zn vacancy induced room-temperature ferromagnetism in Mn-doped ZnO. / Wensheng Yan, Zhihu Sun, Qinghua Liu, Zhongrui Li, Zhiyun Pan, Jie Wang, Shiqiang Wei, Dan Wang, Yingxue Zhou, and Xinyi Zhang. // *Appl. Physics Lett.* – 2007. – Vol. 91. – P. 062113.
- [26] Sharma Parmanand. Ferromagnetism above room temperature in bulk and transparent thin films of Mn-doped ZnO. / Parmanand Sharma, Amita Gupta, K. V. Rao, Frank J. Owens, Renu Sharma, Rajeev Ahuja, J. M. Osorio Guillen, Börje Johansson, and G. A. Gehring. // *Nature Mater.* – 2003. – Vol. 2. – P. 673–677.
- [27] Gopal Priya. Magnetic interactions in transition-metal-doped ZnO: An *ab initio* study. / Priya Gopal and Nicola A. Spaldin. // *Phys. Rev. B.* – 2006. – Vol. 74. –

P. 094418.

- [28] He Y. Origin of ferromagnetism in ZnO codoped with Ga and Co: Experiment and theory. / Y. He, Parmanand Sharma, Krishanu Biswas, E. Z. Liu, Naofumi Ohtsu, A. Inoue, Y. Inada, M. Nomura, J. S. Tse, S. Yin, and J. Z. Jiang. // *Phys. Rev. B.* – 2008. – Vol. 78. – P. 155202.
- [29] Liu En-Zuo. Ferromagnetism induced by defect complex in Co-doped ZnO. / En-Zuo Liu, Yan He, and J. Z. Jiang. // *Appl. Physics Lett.* – 2008. – Vol. 93. – P. 132506.
- [30] Iuşan Diana. Electronic structure and chemical and magnetic interactions in ZnO doped with Co and Al: Experiments and *ab initio* density-functional calculations. / Diana Iuşan, Ronny Knut, Biplab Sanyal, Olof Karis, Olle Eriksson, Victoria A. Coleman, Gunnar Westin, J. Magnus Wikberg, and Peter Svedlindh. // *Phys. Rev. B.* – 2008. – Vol. 78. – P. 085319.
- [31] He A. L. Electronic structure and magnetic properties of Mn-doped ZnO nanotubes: An ab initio study. / A. L. He, X. Q. Wang, Y. Q. Fan, and Y. P. Feng. // *J. Appl. Phys.* – 2010. – Vol. 108. – P. 084308.
- [32] Risbud A. S. Magnetism in polycrystalline cobalt-substituted zinc oxide. / A. S. Risbud, N. A. Spaldin, Z. Q. Chen, S. Stemmer, and Ram Seshadri. // *Phys. Rev. B.* – 2003. – Vol. 68. – P. 205202.
- [33] Spaldin Nicola A. Search for ferromagnetism in transition-metal-doped piezoelectric ZnO. / Nicola A. Spaldin. // *Phys. Rev. B.* – 2004. – Vol. 69. – P. 125201.
- [34] Sluiter Marcel H. F. First Principles Based Design and Experimental Evidence for a ZnO-Based Ferromagnet at Room Temperature. / Marcel H. F. Sluiter, Y. Kawazoe, Parmanand Sharma, A. Inoue, A. R. Raju, C. Rout, and U. V. Waghmare. // *Phys. Rev. Lett.* – 2005. – Vol. 94. – P. 187204.
- [35] Badaeva Ekaterina. Investigation of pure and  $\text{Co}^{2+}$ -doped ZnO quantum dot electronic structures using the density functional theory: choosing the right functional. / Ekaterina Badaeva, Yong Feng, Daniel R Gamelin, and Xiaosong Li. // *New J. Phys.* – 2008. – Vol. 10. – P. 055013.
- [36] Zhao L. The electronic and magnetic properties of (Mn,N)-codoped ZnO from

- first principles. / L. Zhao, P. F. Lu, Z. Y. Yu, X. T. Guo, Y. Shen, H. Ye, G. F. Yuan, and L. Zhang. // *J. Appl. Phys.* – 2010. – Vol. 108. – P. 113924.
- [37] Petit L. Electronic structure of transition-metal impurities in *p*-type ZnO. / L. Petit, T. C. Schulthess, A. Svane, Z. Szotek, W. M. Temmerman, and A. Janotti. // *Phys. Rev. B.* – 2006. – Vol. 73. – P. 045107.
- [38] Sato K. First-principles theory of dilute magnetic semiconductors. / K. Sato, L. Bergqvist, J. Kudrnovský, P. H. Dederichs, O. Eriksson, I. Turek, B. Sanyal, G. Bouzerar, H. Katayama-Yoshida, V. A. Dinh, T. Fukushima, H. Kizaki, and R. Zeller. // *Rev. Mod. Phys.* – 2010. – Vol. 82. – P. 1633.
- [39] Sato Kazunori. High Curie Temperature and Nano-Scale Spinodal Decomposition Phase in Dilute Magnetic Semiconductors. / Kazunori Sato, Hiroshi Katayama-Yoshida, and Peter H. Dederichs. // *Jpn. J. Appl. Phys.* – 2005. – Vol. 44. – P. L948–L951.
- [40] Katayama-Yoshida H. Theory of ferromagnetic semiconductors. / H. Katayama-Yoshida, K. Sato, T. Fukushima, M. Toyoda, H. Kizaki, V. A. Dinh, and P. H. Dederichs. // *Phys. status solidi A.* – 2007. – Vol. 204. – P. 15–32.
- [41] Fukushima Tetsuya. Spinodal Decomposition under Layer by Layer Growth Condition and High Curie Temperature Quasi-One-Dimensional Nano-Structure in Dilute Magnetic Semiconductors. / Tetsuya Fukushima, Kazunori Sato, Hiroshi Katayama-Yoshida, and Peter H. Dederichs. // *Jpn. J. Appl. Phys.* – 2006. – Vol. 45. – P. L416–L418.
- [42] Katayama-Yoshida H. Computational nano-materials design for high-image ferromagnetism in wide-gap magnetic semiconductors. / H. Katayama-Yoshida, K. Sato, T. Fukushima, M. Toyoda, H. Kizaki, V.A. Dinh, and P.H. Dederichs. // *J. Magn. Magn. Mater.* – 2007. – Vol. 310. – P. 2070–2077.
- [43] Sato Kazunori. Super-Paramagnetic Blocking Phenomena and Room-Temperature Ferromagnetism in Wide Band-Gap Dilute Magnetic Semiconductor (Ga,Mn)N. / Kazunori Sato, Tetsuya Fukushima, and Hiroshi Katayama-Yoshida. // *Jpn. J. Appl. Phys.* – 2007. – Vol. 46. – P. L682–L684.
- [44] Sukkar M. H. DEFECT EQUILIBRIA IN ZnO VARISTOR MATERIALS. In

- M. F. Yan and A. H. Heuer, editors, *Advances in Ceramics*, Columbus, Ohio. / M. H. Sukkar and H. L. Tuller. // American Ceramic Society. – 1983. – Vol. 7. – P. 71–90.
- [45] Mahan G. D. Intrinsic defects in ZnO varistors. / G. D. Mahan. // *J. Appl. Phys.* – 1983. – Vol. 54. – P. 3825–3832.
- [46] Hagemark K.I. Defect structure of Zn-doped ZnO. / K.I. Hagemark. // *Journal of Solid State Chemistry*. – 1976. – Vol. 16. – P. 293–299.
- [47] Choi Jae Shi. Study of the nonstoichiometric composition op zinc oxide. / Jae Shi Choi and Chul Hyun Yo. // *Journal of Physics and Chemistry of Solids*. – Vol. 37. – P. 1149–1151.
- [48] Sleight Arthur W. Nonstoichiometry and Doping of Zinc Oxide. / Arthur W. Sleight and Ruiping Wang. // In *Solid-State Chemistry of Inorganic Materials*, MRS Symposia Proceedings, editors: P. K. Davies, A. J. Jacobson, C. C. Torardi, and T. A. Vanderah. – Materials Research Society: Pittsburgh, 1996. – Vol. 453. – P. 323–330.
- [49] Hoffman J. W. Diffusion of oxygen in single crystal zinc oxide. / J. W. Hoffman and I. Lauder. // *Trans. Faraday Soc.* – 1970. – Vol. 66. – P. 2346–2353.
- [50] Ziegler E. Electrical properties and non-stoichiometry in ZnO single crystals. / E. Ziegler, A. Heinrich, H. Oppermann, and G. Stöver. // *phys. stat. sol. (a)*. – 1981. – Vol. 66. – P. 635–648.
- [51] Ando K. Large magneto-optical effect in an oxide diluted magnetic semiconductor  $Zn_{1-x}Co_xO$ . / K. Ando, H. Saito, Zhengwu Jin, T. Fukumura, M. Kawasaki, Y. Matsumoto, and H. Koinuma. // *Appl. Physics Lett.* – 2001. – Vol. 78. – P. 2700.
- [52] Yoo Y.-Z. ZnO–CoO solid solution thin films. / Y.-Z. Yoo, T. Fukumura, Zhengwu Jin, K. Hasegawa, M. Kawasaki, P. Ahmet, T. Chikyow, and H. Koinuma. // *J. Appl. Phys.* – 2001. – Vol. 90. – P. 4246–4250.
- [53] Kikoin K. Peculiarities of the ferromagnetic ordering in diluted magnetic insulators. / K. Kikoin. // *Low Temp. Phys.* – 2009. – Vol. 35. – P. 58–61.
- [54] Fukumura T. Magnetic properties of Mn-doped ZnO. / T. Fukumura, Zhengwu

- Jin, M. Kawasaki, T. Shono, T. Hasegawa, S. Koshihara, and H. Koinuma. // *Appl. Physics Lett.* – 2001. – Vol. 78. – P. 958.
- [55] Tiwari A. Structural, optical and magnetic properties of diluted magnetic semiconducting  $Zn_{1-x}Mn_xO$  films. / A. Tiwari, C. Jin, A. Kivt, D. Kumar, J.F. Muth, and J. Narayan. // *Solid State Commun.* – 2002. – Vol. 121. – P. :371–374.
- [56] Jung S. W. Ferromagnetic properties of  $Zn_{1-x}Mn_xO$  epitaxial thin films. / S. W. Jung, S.-J. An, Gyu-Chul Yi, C. U. Jung, Sung-Ik Lee, and Sunglae Cho. // *Appl. Physics Lett.* – 2002. – Vol. 80. – P. 4561.
- [57] Cheng X. M. Magnetic properties of epitaxial Mn-doped ZnO thin films. / X. M. Cheng and C. L. Chien. // *J. Appl. Phys.* – 2003. – Vol. 93. – P. 7876–7878.
- [58] Yoon S. W. Magnetic properties of ZnO-based diluted magnetic semiconductors. / S. W. Yoon, S.-B. Cho, S. C. We, S. Yoon, B. J. Suh, H. K. Song, and Y. J. Shin. // *J. Appl. Phys.* – 2003. – Vol. 93. – P. 7879–7881.
- [59] Roy V. A. L. Magnetic properties of Mn doped ZnO tetrapod structures. / V. A. L. Roy, A. B. Djurišić, H. Liu, X. X. Zhang, Y. H. Leung, M. H. Xie, J. Gao, H. F. Lui, and C. Surya. // *Appl. Physics Lett.* – 2004. – Vol. 84. – P. 756.
- [60] Luo J. Structure and magnetic properties of Mn-doped ZnO nanoparticles. / J. Luo, J. K. Liang, Q. L. Liu, F. S. Liu, Y. Zhang, B. J. Sun, and G. H. Rao. // *J. Appl. Phys.* – 2005. – Vol. 97. – P. 086106.
- [61] Norberg Nick S. Synthesis of Colloidal  $Mn^{2+}:ZnO$  Quantum Dots and High- $T_C$  Ferromagnetic Nanocrystalline Thin Films. / Nick S. Norberg, Kevin R. Kittilstved, James E. Amonette, Ravi K. Kukkadapu, Dana A. Schwartz, and Daniel R. Gamelin. // *J. Am. Chem. Soc.* – 2004. – Vol. 126. – P. 9387–9398.
- [62] Norton D. P. Ferromagnetism in Mn-implanted ZnO:Sn single crystals. / D. P. Norton, S. J. Pearton, A. F. Hebard, N. Theodoropoulou, L. A. Boatner, and R. G. Wilson. // *Appl. Physics Lett.* – 2003. – Vol. 82. – P. 239.
- [63] Kittilstved Kevin R. Chemical Manipulation of High- $T_C$  Ferromagnetism in ZnO Diluted Magnetic Semiconductors. / Kevin R. Kittilstved, Nick S. Norberg, and Daniel R. Gamelin. // *Phys. Rev. Lett.* – 2005. – Vol. 94. – P. 147209.
- [64] Kim Sang Sub. Heteroepitaxial growth behavior of Mn-doped ZnO thin films

on Al<sub>2</sub>O<sub>3</sub> (0001) by pulsed laser deposition. / Sang Sub Kim, Jong Ha Moon, Byung-Teak Lee, Oh Sung Song, and Jung Ho Je. // *J. Appl. Phys.* – 2004. – Vol. 95. – P. 454–459.

- [65] Kolesnik S. Structural and magnetic properties of transition metal substituted ZnO. / S. Kolesnik, B. Dabrowski, and J. Mais. // *J. Appl. Phys.* – 2004. – Vol. 95. – P. 2582–2586.
- [66] Bondino F. Electronic structure of Mn-doped ZnO by x-ray emission and absorption spectroscopy. / F. Bondino, K. B. Garg, E. Magnano, E. Carleschi, M. Heinonen, R. K. Singhal, S. K. Gaur, and F. Parmigiani. // *J. Phys.: Condens. Matter.* – 2008. – Vol. 20. – P. 275205.
- [67] Gu Bo. Crystal structure effect on the ferromagnetic correlations in ZnO with magnetic impurities. / Bo Gu, Nejat Bulut, and Sadamichi Maekawa. // *J. Appl. Phys.* – 2008. – Vol. 104. – P. 103906.
- [68] Ishida Y. Soft x-ray magnetic circular dichroism study of weakly ferromagnetic Zn<sub>1-x</sub>V<sub>x</sub>O thin film. / Y. Ishida, J. I. Hwang, M. Kobayashi, Y. Takeda, K. Mamiya, J. Okamoto, S.-I. Fujimori, T. Okane, K. Terai, Y. Saitoh, Y. Muramatsu, A. Fujimori, A. Tanaka, H. Saeki, T. Kawai, and H. Tabata. // *Applied Physics Letters.* – 2007. – Vol. 90. – P. 022510.
- [69] Farley N. R. S. Magnetic properties of sol-gel-derived doped ZnO as a potential ferromagnetic semiconductor: a synchrotron-based study. / N. R. S. Farley, K. W. Edmonds, A. A. Freeman, G. van der Laan, C. R. Staddon, D. H. Gregory, and B. L. Gallagher. // *New J. Phys.* – 2008. – Vol. 10. – P. 055012.
- [70] Schoofs Frank. Strain dependent defect mediated ferromagnetism in Mn-doped and undoped ZnO thin films. / Frank Schoofs, Thomas Fix, Ali M. H. R. Hakimi, Sarnjeet S. Dhesi, Gerrit van der Laan, Stuart A. Cavill, Sean Langridge, Judith L. MacManus-Driscoll, and Mark G. Blamire. // *J. Appl. Phys.* – 2010. – Vol. 108. – P. 053911.
- [71] Shinagawa Tsutomu. Thermal Phase Transformation of ZnO-Based Transparent Ferromagnetic Composite Films and the Change in Magnetic Characteristics. / Tsutomu Shinagawa, Masanobu Izaki, Kuniaki Murase, Tomoya Uruga, Tetsuya

- Nákamura, Yasuyuki Matsumura, and Yasuhiro Awakura. // *J. Electrochem. Soc.* – 2006. – Vol. 153(2). – P. G168–G174.
- [72] Guo J.-H. X-ray spectroscopic study of the charge state and local ordering of room-temperature ferromagnetic Mn-doped ZnO. / J.-H. Guo, Amita Gupta, Parmanand Sharma, K. V. Rao, M. A. Marcus, C. L. Dong, J. M. O. Guillen, S. M. Butorin, M. Mattesini, P. A. Glans, K. E. Smith, C. L. Chang, and R. Ahuja. // *J. Phys.: Condens. Matter.* – 2007. – Vol. 19. – P. 172202.
- [73] Kang Y. J. Ferromagnetic  $Zn_{1-x}Mn_xO$  ( $x = 0.05, 0.1$ , and  $0.2$ ) Nanowires. / Y. J. Kang, D. S. Kim, S. H. Lee, J. Park, J. Chang, J. Y. Moon, G. Lee, J. Yoon, Y. Jo, and M. H. Jung. // *J. Phys. Chem. C.* – 2007. – Vol. 111. – P. 14956–14961.
- [74] Thakur P. X-ray absorption and magnetic circular dichroism characterizations of Mn doped ZnO. / P. Thakur, K. H. Chae, J.-Y. Kim, M. Subramanian, R. Jayavel, and K. Asokan. // *Appl. Physics Lett.* – 2007. – Vol. 91. – P. 162503.
- [75] Droubay T. C. Correlated substitution in paramagnetic  $Mn^{2+}$ -doped ZnO epitaxial films. / T. C. Droubay, D. J. Keavney, T. C. Kaspar, S. M. Heald, C. M. Wang, C. A. Johnson, K. M. Whitaker, D. R. Gamelin, and S. A. Chambers. // *Phys. Rev. B.* – 2009. – Vol. 79. – P. 155203.
- [76] Trolio A. Di. Bulk sensitive x-ray absorption and magnetic circular dichroism investigation of Mn- and Co-doped ZnO thin films. / A. Di Trolio, R. Larciprete, S. Turchini, and N. Zema. // *Appl. Physics Lett.* – 2010. – Vol. 97. – P. 052505.
- [77] Johnson Claire A. Mid-gap electronic states in  $Zn_{1-x}Mn_xO$ . / Claire A. Johnson, Kevin R. Kittilstved, Tiffany C. Kaspar, Tim C. Droubay, Scott A. Chambers, G. Mackay Salley, and Daniel R. Gamelin. // *Phys. Rev. B.* – 2010. – Vol. 82. – P. 115202.
- [78] Thakur P. Electronic Structure of Mn-Doped ZnO Studied by Using X-ray Absorption Spectroscopy. / P. Thakur, K. H. Chae, M. Subramanian, R. Jayavel, and K. Asokan. // *J. Korean Phys. Soc.* – 2008. – Vol. 53. – P. 2821–2825.
- [79] Thakur P. X-ray Absorption and Emission Studies of Mn-doped ZnO Thin Films. / P. Thakur, S. Gautan, K.H. Chae, M. Subramanian, R. Jayavel, and K. Asokan. // *J. Korean Phys. Soc.* – 2008. – Vol. 55. – P. 177–182.

- [80] Freeman A. A. Valence band orbital polarization in III-V ferromagnetic semiconductors. / A. A. Freeman, K. W. Edmonds, G. van der Laan, R. P. Campion, A. W. Rushforth, N. R. S. Farley, T. K. Johal, C. T. Foxon, B. L. Gallagher, A. Rogalev, and F. Wilhelm. // *Phys. Rev. B.* – 2008. – Vol. 77. – P. 073304.
- [81] Kataoka T. Electronic structure and magnetism of the diluted magnetic semiconductor Fe-doped ZnO nanoparticles. / T. Kataoka, M. Kobayashi, Y. Sakamoto, G. S. Song, A. Fujimori, F.-H. Chang, H.-J. Lin, D. J. Huang, C. T. Chen, T. Ohkochi, Y. Takeda, T. Okane, Y. Saitoh, H. Yamagami, A. Tanaka, S. K. Mandal, T. K. Nath, D. Karmakar, and I. Dasgupta. // *J. Appl. Phys.* – 2010. – Vol. 107. – P. 033718.
- [82] Kataoka Takashi. X-ray Magnetic Circular Dichroism Investigations of the Origin of Room Temperature Ferromagnetism in Fe-Doped ZnO Nanoparticles. / Takashi Kataoka, Masaki Kobayashi, Gyong Sok Song, Yuta Sakamoto, Atsushi Fujimori, Fan-Hsiu Chang, Hong-Ji Lin, Di Jing Huang, Chien Te Chen, Sanjay Kumar Mandal, Tapan Kumar Nath, Debjani Karmakar, and Indra Dasgupta. // *Jpn. J. Appl. Phys.* – Vol. 48. – P. 04C200.
- [83] Gautam Sanjeev. Electronic structure studies of Fe-doped ZnO nanorods by x-ray absorption fine structure. / Sanjeev Gautam, Shalendra Kumar, P. Thakur, K. H. Chae, Ravi Kumar, B. H. Koo, and C. G. Lee. // *J. Phys. D: Appl. Phys.* – 2009. – Vol. 42. – P. 175406.
- [84] Kobayashi M. Characterization of magnetic components in the diluted magnetic semiconductor  $Zn_{1-x}Co_xO$  by x-ray magnetic circular dichroism. / M. Kobayashi, Y. Ishida, J. I. Hwang, T. Mizokawa, A. Fujimori, K. Mamiya, J. Okamoto, Y. Takeda, T. Okane, Y. Saitoh, Y. Muramatsu, A. Tanaka, H. Saeki, H. Tabata, and T. Kawai. // *Phys. Rev. B.* – 2005. – Vol. 72. – P. 201201.
- [85] Gacic Milan. Magnetism of Co-doped ZnO thin films. / Milan Gacic, Gerhard Jakob, Christian Herbort, Hermann Adrian, Thomas Tietze, Sebastian Brück, and Eberhard Goering. // *Phys. Rev. B.* – 2007. – Vol. 75. – P. 205206.
- [86] Barla A. Paramagnetism of the Co sublattice in ferromagnetic  $Zn_{1-x}Co_xO$  films. / A. Barla, G. Schmerber, E. Beaurepaire, A. Dinia, H. Bieber, S. Colis, F. Scheurer,

- J.-P. Kappler, P. Imperia, F. Nolting, F. Wilhelm, A. Rogalev, D. Müller, and J. J. Grob. // [Phys. Rev. B.](#) – 2007. – Vol. 76. – P. 125201.
- [87] Ney A. Absence of Intrinsic Ferromagnetic Interactions of Isolated and Paired Co Dopant Atoms in  $Zn_{1-x}Co_xO$  with High Structural Perfection. / A. Ney, K. Ollefs, S. Ye, T. Kammermeier, V. Ney, T. C. Kaspar, S. A. Chambers, F. Wilhelm, and A. Rogalev. // [Phys. Rev. Lett.](#) – 2008. – Vol. 100. – P. 157201.
- [88] Rode K. Magnetism of  $(Zn,Co)O$  thin films probed by x-ray absorption spectroscopies. / K. Rode, R. Mattana, A. Anane, V. Cros, E. Jacquet, J.-P. Contour, F. Petroff, A. Fert, M.-A. Arrio, Ph. Sainctavit, P. Bencok, F. Wilhelm, N. B. Brookes, and A. Rogalev. // [Appl. Physics Lett.](#) – 2008. – Vol. 92. – P. 012509.
- [89] Opel M. Nanosized superparamagnetic precipitates in cobalt-doped ZnO. / M. Opel, K.-W. Nielsen, S. Bauer, S. T. B. Goennenwein, J. C. Cezar, D. Schmeisser, J. Simon, W. Mader, and R. Gross. // [Europ. Phys. J. B.](#) – 2008. – Vol. 63. – P. 437–444.
- [90] Tietze Thomas. XMCD studies on Co and Li doped ZnO magnetic semiconductors. / Thomas Tietze, Milan Gacic, Gisela Schütz, Gerhard Jakob, Sebastian Brück, and Eberhard Goering. // [New J. Phys.](#) – 2008. – Vol. 10. – P. 055009.
- [91] Kammermeier T. Element specific measurements of the structural properties and magnetism of  $Co_{x1-x}O$ . / T. Kammermeier, V. Ney, S. Ye, K. Ollefs, T.C. Kaspar, S.A. Chambers, F. Wilhelm, A. Rogalev, and A. Ney. // [J. Magn. Magn. Mater.](#) – 2009. – Vol. 321. – P. 699–701.
- [92] Singh Abhinav Pratap. NEXAFS and XMCD studies of single-phase Co doped ZnO thin films. / Abhinav Pratap Singh, Ravi Kumar, P. Thakur, N. B. Brookes, K. H. Chae, and W. K. Choi. // [J. Phys.: Condens. Matter.](#) – 2009. – Vol. 21. – P. 185005.
- [93] Kumar Shalendra. Ferromagnetism in Chemically-synthesized Co-doped ZnO. / Shalendra Kumar, Y.J. Kim, B.H. Koo, Heekyu Choi, C.G. Lee, S.K. Sharma, M. Knobel, S. Gautam, and K.H. Chae. // [J. Korean Phys. Soc.](#) – 2009. – Vol. 55. – P. 1060.
- [94] Ney A. Anisotropic paramagnetism of Co-doped ZnO epitaxial films. / A. Ney,

- T. Kammermeier, K. Ollefs, S. Ye, V. Ney, T. C. Kaspar, S. A. Chambers, F. Wilhelm, and A. Rogalev. // [Phys. Rev. B.](#) – 2010. – Vol. 81. – P. 054420.
- [95] Ney A. Magnetism of Co doped ZnO with Al codoping: Carrier-induced mechanisms versus extrinsic origins. / A. Ney, T. Kammermeier, K. Ollefs, S. Ye, V. Ney, T. C. Kaspar, S. A. Chambers, F. Wilhelm, and A. Rogalev. // [Phys. Rev. B.](#) – Vol. 82. – P. 041202.
- [96] Ney V. Tuning the magnetic properties of  $Zn_{1-x}Co_xO$  films. / V. Ney, S. Ye, T. Kammermeier, K. Ollefs, A. Ney, T.C. Kaspar, S.A. Chambers, F. Wilhelm, and A. Rogalev. // [J. Magn. Magn. Mater.](#) – 2010. – Vol. 322. – P. 1232.
- [97] Ney V. Co-Doped ZnO Epitaxial Films: From a Brillouin-Like Paramagnet to a Phase-Separated Superparamagnetic Ensemble. / V. Ney, S. Ye, K. Ollefs, T. Kammermeier, F. Wilhelm, A. Rogalev, and A. Ney. // [J. Nanosci. Nanotechnol.](#) – 2010. – Vol. 10. – P. 5958–5963.
- [98] Ney A. Advanced spectroscopic synchrotron techniques to unravel the intrinsic properties of dilute magnetic oxides: the case of Co:ZnO. / A. Ney, M. Opel, T. C. Kaspar, V. Ney, S. Ye, K. Ollefs, T. Kammermeier, S. Bauer, K.-W. Nielsen, S. T. B. Goennenwein, M. H. Engelhard, S. Zhou, K. Potzger, J. Simon, W. Mader, S. M. Heald, J. C. Cezar, F. Wilhelm, A. Rogalev, R. Gross, and S. A. Chambers. // [New J. Phys.](#) – 2010. – Vol. 12. – P. 013020.
- [99] Kobayashi M. Antiferromagnetic interaction between paramagnetic Co ions in the diluted magnetic semiconductor  $Zn_{1-x}Co_xO$ . / M. Kobayashi, Y. Ishida, J. I. Hwang, Y. Osafune, A. Fujimori, Y. Takeda, T. Okane, Y. Saitoh, K. Kobayashi, H. Saeki, T. Kawai, and H. Tabata. // [Phys. Rev. B.](#) – 2010. – Vol. 81. – P. 075204.
- [100] Photongkam P. Enhancement of Co substitution induced by Eu codoping in ZnO-based diluted magnetic semiconducting thin films. / P. Photongkam, Y. B. Zhang, M. H. N. Assadi, S. Li, D. Yu, M. Ionescu, and A. V. Pan. // [J. Appl. Phys.](#) – 2010. – Vol. 107. – P. 033909.
- [101] Jiang Yong. Experimental and theoretical investigations on ferromagnetic nature of Mn-doped dilute magnetic semiconductors. / Yong Jiang, Wensheng Yan, Zhihu Sun, Qinghua Liu, Zhiyun Pan, Tao Yao, Yuanyuan Li, Zemin Qi, Guobin

Zhang, Pengshou Xu, Ziyu Wu, and Shiqiang Wei. // [J. Phys.: Conf. Ser.](#) – 2009. – Vol. 190. – P. 012100.

- [102] Ratcliff II William D. Chapter 5 – Multiferroics. In: Felix Fernandez-Alonso and David L. Price, editors, Neutron Scattering. Magnetic and Quantum Phenomena, Experimental Methods in the Physical Sciences. / William D. Ratcliff II and Jeffrey W. Lynn. // [Academic Press](#). – 2015. – Vol. 48. – P. 291–338.
- [103] Spaldin Nicola A. The Renaissance of Magnetoelectric Multiferroics. / Nicola A. Spaldin and Manfred Fiebig. // [Science](#). – 2005. – Vol. 309. – P. 391–392.
- [104] Eerenstein W. Multiferroic and magnetoelectric materials. / W. Eerenstein, N. D. Mathur, and J. F. Scott. // [Nature](#). – 2008. – Vol. 442. – P. 759–765.
- [105] Binek Ch. Magnetoelectronics with magnetoelectrics. / Ch. Binek and B. Doudin. // [J. Phys.: Condens. Matter](#). – 2005. – Vol. 17. – P. L39.
- [106] Gajek Martin. Tunnel junctions with multiferroic barriers. / Martin Gajek, Manuel Bibes, Stéphane Fusil, Karim Bouzehouane, Josep Fontcuberta, Agnès Barthélémy, and Albert Fert. // [Nature Mater](#). 2007. – Vol. 6. – P. 296–302.
- [107] Nan Ce-Wen. Multiferroic magnetoelectric composites: Historical perspective, status, and future directions. / Ce-Wen Nan, M. I. Bichurin, Shuxiang Dong, D. Viehland, and G. Srinivasan. // [J. Appl. Phys](#). – 2008. – Vol. 103. – P. 031101.
- [108] Wang J. Epitaxial BiFeO<sub>3</sub> Multiferroic Thin Film Heterostructures. / J. Wang, J. B. Neaton, H. Zheng, V. Nagarajan, S. B. Ogale, B. Liu, D. Viehland, V. Vaithyanathan, D. G. Schlom, U. V. Waghmare, N. A. Spaldin, K. M. Rabe, M. Wuttig, and R. Ramesh. // [Science](#). – 2003. – Vol. 299. – P. 1719–1722.
- [109] Stroppa Alessandro. The multiferroic phase of DyFeO<sub>3</sub>: an *ab initio* study. / Martijn Marsman, Georg Kresse, and Silvia Picozzi. // [New J. Phys.](#) – 2010. – Vol. 12. – P. 093026
- [110] Herrero-Martín Javier. Magnetic and electronic properties of the ferroelectric-photovoltaic ordered double perovskite CaMnTi<sub>2</sub>O<sub>6</sub> investigated by x-ray absorption spectroscopies. / Javier Herrero-Martín, Javier Ruiz-Fuertes, Thomas Bernert, Monika Koch-Müller, Eiken Haussühl, and José Luis García-Muñoz. // [Phys. Rev. B](#). – Vol. 97. – P. 235129.

- [111] Jonker G.H. Ferromagnetic compounds of manganese with perovskite structure. / G.H. Jonker and J.H. van Santen. // *Physica.* – 1950. – Vol. 16. – P. 337–349.
- [112] Wollan E. O. Neutron Diffraction Study of the Magnetic Properties of the Series of Perovskite-Type Compounds  $[(1-x)\text{La},x\text{Ca}]\text{MnO}_3$ . / E. O. Wollan and W. C. Koehler. // *Phys. Rev.* – 1950. – Vol. 100. – P. 545.
- [113] Goodenough John B. Theory of the Role of Covalence in the Perovskite-Type Manganites  $[\text{La}, \text{M(II)}]\text{MnO}_3$ . / John B. Goodenough. // *Phys. Rev.* – 1955. – Vol. 100. – P. 564.
- [114] Mochizuki Masahito. Orbital physics in the perovskite Ti oxides. / Masahito Mochizuki and Masatoshi Imada. // *New J. Phys.* – 2004. – Vol. 6. – P. 154.
- [115] Imada Masatoshi. Metal-insulator transitions. / Masatoshi Imada, Atsushi Fujimori, and Yoshinori Tokura. // *Rev. Mod. Phys.* – 1998. – Vol. 30. – P. 1039.
- [116] Glazer A. M. The classification of tilted octahedra in perovskites. / A. M. Glazer. // *Acta Cryst.* – 1972. – Vol. B28. – P. 3384–3392.
- [117] Howard C. J. Group-Theoretical Analysis of Octahedral Tilting in Perovskites. / C. J. Howard and H. T. Stokes. // *Acta Cryst.* – 1998. – Vol. B54. – P. 782–789.
- [118] Eng Hank W. Investigations of the electronic structure of  $d^0$  transition metal oxides belonging to the perovskite family. / Hank W. Eng, Paris W. Barnes, Benjamin M. Auer, and Patrick M. Woodward. // *J. Solid State Chem.* – 2003. – Vol. 175. – P. 94–109.
- [119] Kim Beom Hyun. Nearest and next-nearest superexchange interactions in orthorhombic perovskite manganites  $\text{RMnO}_3$  ( $\text{R}$  = rare earth). / Beom Hyun Kim and B. I. Min. // *Phys. Rev. B.* – Vol. 80. – P. 064416.
- [120] Deschanvres A. / A. Deschanvres, B. Raveau, and F. Tollemer. // *Bull. Soc. Chim. Fr.* – 1967. – Vol. 11. – P. 4077.
- [121] Marezio M. High pressure synthesis and crystal structure of  $\text{NaMn}_7\text{O}_{12}$ . / M. Marezio, P.D. Dernier, J. Chenavas, and J.C. Joubert. // *J. Solid State Chem.* – 1973. – Vol. 6. – P. 16.
- [122] Homes C. C. Optical Response of High-Dielectric-Constant Perovskite-Related Oxide. / C. C. Homes, T. Vogt, S. M. Shapiro, S. Wakimoto, and A. P. Ramirez.

// *Science.* – 2001. – Vol. 293. – P. 673–676.

- [123] Long Y. W. Temperature-induced A–B intersite charge transfer in an A-site-ordered  $\text{LaCu}_3\text{Fe}_4\text{O}_{12}$  perovskite. / Y. W. Long, N. Hayashi, T. Saito, M. Azuma, S. Muranaka, and Y. Shimakawa. // *Nature.* – 2009. – Vol. 458. – P. 60.
- [124] Johnson R. D. Giant Improper Ferroelectricity in the Ferroaxial Magnet  $\text{CaMn}_7\text{O}_{12}$ . / R. D. Johnson, L. C. Chapon, D. D. Khalyavin, P. Manuel, P. G. Radaelli, and C. Martin. // *Phys. Rev. Lett.* – 2012. – Vol. 108. – P. 067201.
- [125] Shimakawa Yuichi. A-Site-Ordered Perovskites with Intriguing Physical Properties. / Yuichi Shimakawa. // *Inorg. Chem.* – 2008. – Vol. 47. – P. 8562–8570.
- [126] Shiraki Hiroshi. Metallic Behavior in A-Site-Ordered Perovskites  $\text{ACu}_3\text{V}_4\text{O}_{12}$  with  $A = \text{Na}^+$ ,  $\text{Ca}^{2+}$ , and  $\text{Y}^{3+}$ . / Hiroshi Shiraki, Takashi Saito, Masaki Azuma, and Yuichi Shimakawa. // *J. Phys. Soc. Jpn.* – 2008. – Vol. 77. – P. 064705.
- [127] Ovsyannikov Sergey V. Structural and Magnetic Transitions in  $\text{CaCo}_3\text{V}_4\text{O}_{12}$  Perovskite at Extreme Conditions. / Sergey V. Ovsyannikov, Elena Bykova, Anna Pakhomova, Denis P. Kozlenko, Maxim Bykov, Sergey E. Kichanov, Natalia V. Morozova, Igor V. Korobeinikov, Fabrice Wilhelm, Andrei Rogalev, Alexander A. Tsirlin, Alexander V. Kurnosov, Yury G. Zainulin, Nadezda I. Kadyrova, Alexander P. Tyutyunnik, and Leonid Dubrovinsky. // *Inorg. Chem.* – 2017. – Vol. 56. – P. 6251–6263.
- [128] Petit Christophe T. G. Novel Redox Reversible Oxide, Sr-doped Cerium Orthovanadate to Metavanadate. / Christophe T. G. Petit, Rong Lan, Peter I. Cowin, John T. S. Irvine, and Shanwen Tao. // *J. Mater. Chem.* – 2011. – Vol. 21. – P. 525–531.
- [129] Aimi Akihisa. High-Pressure Synthesis of A-Site Ordered Double Perovskite  $\text{CaMnTi}_2\text{O}_6$  and Ferroelectricity Driven by Coupling of A-Site Ordering and the Second-Order Jahn–Teller Effect. / Akihisa Aimi, Daisuke Mori, Ko-ichi Hiraki, Toshihiro Takahashi, Yue Jin Shan, Yuichi Shirako, Jianshi Zhou, and Yoshiyuki Inaguma. // *Chem. Mater.* – 2014. – Vol. 26. – P. 2601–2608.
- [130] Gou Gaoyang. A-Site Ordered Double Perovskite  $\text{CaMnTi}_2\text{O}_6$  as a Multifunctional Piezoelectric and Ferroelectric–Photovoltaic Material. / Gaoyang Gou,

Nenian Charles, Jing Shi, and James M. Rondinelli. // *Inorg. Chem.* – 2017. – Vol. 56. – P. 11854–11861.

- [131] Ovsyannikov Sergey V. New Antiferromagnetic Perovskite  $\text{CaCo}_3\text{V}_4\text{O}_{12}$  Prepared at High-Pressure and High-Temperature Conditions. / Sergey V. Ovsyannikov, Yury G. Zainulin, Nadezda I. Kadyrova, Alexander P. Tyutyunnik, Anna S. Semenova, Deepa Kasinathan, Alexander A. Tsirlin, Nobuyoshi Miyajima, and Alexander E. Karkin. // *Inorg. Chem.* – 2013. – Vol. 52. – P. 11703–11710.
- [132] Anisimov Vladimir I. Band theory and Mott insulators: Hubbard  $U$  instead of Stoner  $I$ . / Vladimir I. Anisimov, Jan Zaanen, and Ole K. Andersen. // *Phys. Rev. B.* – Vol. 44. – P. 943.
- [133] Hohenberg P. Inhomogeneous Electron Gas. / P. Hohenberg and W. Kohn. // *Phys. Rev.* – 1964. – Vol. 136. P. B864–B871.
- [134] Kohn W. Self-Consistent Equations Including Exchange and Correlation Effects. / W. Kohn and L. J. Sham. // *Phys. Rev.* – 1965. – Vol. 140. – P. A1133–A1137.
- [135] Sham L. J. One-Particle Properties of an Inhomogeneous Interacting Electron Gas. / L. J. Sham and W. Kohn. // *Phys. Rev.* – 1966. – Vol. 145. – P. 561–582.
- [136] Langreth D.C. Exchange-correlation energy of a metallic surface. / D.C. Langreth and J.P. Perdew. // *Solid State Commun.* – 1975. – Vol. 17. – P. 1425–1429.
- [137] Gunnarsson O. Exchange and correlation in atoms, molecules and solids by the spin-density-functional formalism. / O. Gunnarsson and B. I. Lundqvist. // *Phys. Rev. B.* – 1976. – Vol. 13. – P. 4274.
- [138] Gunnarsson O. Erratum: Exchange and correlation in atoms, molecules, and solids by the spin-density-functional formalism. / O. Gunnarsson and B. I. Lundqvist. // *Phys. Rev. B.* – 1977. – Vol. 15. – P. 6006.
- [139] Gunnarsson O. Density Functional Calculations for Atoms, Molecules and Clusters. / O. Gunnarsson and R. O. Jones. // *Phys. Scr.* – 1980. – Vol. 21. – P. 394.
- [140] Gorobchenko V. D. The dielectric constant of an interacting electron gas. / V. D. Gorobchenko and Evgenii G. Maksimov. // *Sov. Phys. Usp.* – 1980. – Vol. 23. – P. 35.
- [141] Hedin L. Explicit local exchange-correlation potentials. / L. Hedin and B. I.

- Lundqvist. // *J. Phys. C: Solid State Phys.* – 1971. – Vol. 4. – P. 2064–2084.
- [142] von Barth U. A local exchange-correlation potential for the spin polarized case. / U. von Barth and L. Hedin. // *J. Phys. C: Solid State Phys.* – 1972. – Vol. 5. – P. 1629.
- [143] Perdew John P. Density-Functional Theory for Fractional Particle Number: Derivative Discontinuities of the Energy. / John P. Perdew, Robert G. Parr, Mel Levy, and Jose L. Balduz Jr. // *Phys. Rev. Lett.* – 1982. – Vol. 49. – P. 1691–1694.
- [144] Gunnarsson O. Density-Functional Treatment of an Exactly Solvable Semiconductor Model. / O. Gunnarsson and K. Schönhammer. // *Phys. Rev. Lett.* – 1986. – Vol. 56. – P. 1968.
- [145] Svane A. Localization in the self-interaction-corrected density-functional formalism. / A. Svane and O. Gunnarsson. // *Phys. Rev. B.* - 1988. – Vol. 37. – P. 9919(R).
- [146] Herring C. In George Tibor Rado and Harry Suhl, editors. Magnetism: Exchange interactions among itinerant electrons. / C. Herring. // New York: Academic Press. – 1966. – Vol. IV.
- [147] Anisimov V. I. Density-functional theory and NiO photoemission spectra. / V. I. Anisimov, I. V. Solovyev, M. A. Korotin, Czyżyk, and G. A. Sawatsky. // *Phys. Rev. B.* – 1993. – Vol. 48. – P. 16929.
- [148] Anisimov V. I. Density-functional calculation of effective Coulomb interactions in metals. / V. I. Anisimov and O. Gunnarsson. // *Phys. Rev. B.* – 1991. – Vol. 43. – P. 7570.
- [149] de Groot F. M. F. 2p x-ray absorption of 3d transition-metal compounds: An atomic multiplet description including the crystal field. / F. M. F. de Groot, J. C. Fuggle, B. T. Thole, and G. A. Sawatzky. // *Phys. Rev. B.* – 1990. – Vol. 42. – P. 5459.
- [150] Harmon B.N. Calculation of magneto-optical properties for 4f systems: LSDA + Hubbard  $U$  results. / B.N. Harmon, V.P. Antropov, A.I. Liechtenstein, I.V. Solovyev, and V.I. Anisimov. // *J. Phys. Chem. Solids.* – 1995. – Vol. 56. – P. 1521–1524.

- [151] Oppeneer P. M. Theory of the anomalous magnetic phase transition in UNiSn. / P. M. Oppeneer, A. N. Yaresko, A. Ya. Perlov, V. N. Antonov, and H. Eschrig. // *Phys. Rev. B.* – 1996. – Vol. 54. – P. R3706(R).
- [152] Wigner E. On the Construction of Metallic Sodium. / E. Wigner and F. Seitz. // *Phys. Rev.* – 1933. – Vol. 43. – P. 804.
- [153] Slater J. C. Wave Functions in a Periodic Potential. / J. C. Slater. // *Phys. Rev.* – 1937. – Vol. 51. – P. 846.
- [154] Shaw Jerry C. Inversion of Fermi-Surface Data Using Partial-Wave Phase Shifts and Their Derivatives: An Application to the Noble Metals. / Jerry C. Shaw, J. B. Ketterson, and L. R. Windmiller. // *Phys. Rev. B.* – 1972. – Vol. 5. – P. 3894.
- [155] Andersen O. K. Crystal Potential Parameters from Fermi-Surface Dimensions. / O. K. Andersen. // *Phys. Rev. Lett.* – 1971. – Vol. 27. – P. 1211.
- [156] Andersen O. K. Simple approach to the band-structure problem. / O. K. Andersen. // *Solid State Communications.* – 1973. – Vol. 13. – P. 133–136.
- [157] Varshalovich D. A. Quantum Theory of Angular Momentum. / D. A. Varshalovich, A. N. Moskalev, and V. K. Khersonskii. // *WORLD SCIENTIFIC.* – 1988.
- [158] Nemoshkalenko V. V. The Relativistic Linear Muffin-Tin Orbital Method: Application to Au. / A. E. Krasovskii, V. N. Antonov, Vl. N. Antonov, U. Fleck, H. Wonn, and P. Ziesche. // *Phys. Stat. Sol. (b)*. – 1983. – Vol. 120. – P. 283–296.
- [159] Andersen O. Krogh. Linear methods in band theory. / O. Krogh Andersen. // *Phys. Rev. B.* – 1975. – Vol. 12. – P. 3060.
- [160] MacDonald A. H. Relativistic density functional formalism. / A. H. MacDonald and S. H. Vosko. // *J. Phys. C: Solid State Phys.* – 1979. – Vol. 12. – P. 2977–2990.
- [161] Ebert H. Two ways to perform spin-polarized relativistic linear muffin-tin-orbital calculations. / H. Ebert. // *Phys. Rev. B.* – 1988. – Vol. 38. – P. 9390–9397.
- [162] Solovyev I. V. Spin-polarized relativistic linear-muffin-tin-orbital method: Volume-dependent electronic structure and magnetic moment of plutonium. / I. V. Solovyev, A. I. Lichtenstein, V. A. Gubanov, V. P. Antropov, and O. K. Andersen. // *Phys. Rev. B.* – 1991. – Vol. 43. – P. 14414–14422.
- [163] Krasovskii A. E. Improved approach to spin-polarized relativistic LMTO formal-

- ism: Application to the electronic structure of Fe-Ni compounds at the Earth's core conditions. / A. E. Krasovskii. // *Phys. Rev. B.* – 1999. – Vol. 60. – P. 12788–12798.
- [164] Feder R. Relativistic multiple scattering theory of electrons by ferromagnets. / R. Feder, F. Rosicky, and B. Ackermann. // *Z. Physik B - Condensed Matter.* – 1983. – Vol. 52. – P. 31–36.
- [165] Strange P. Relativistic spin-polarized scattering theory – solution of the single-site problem. / P. Strange, J. Staunton, and B. L. Gyorffy. // *J. Phys. C: Solid State Phys.* – 1984. – Vol. 17. – P. 3355–3371.
- [166] Cortona P. Relativistic extension of the spin-polarized local-density-functional theory: Study of the electronic and magnetic properties of the rare-earth ions. / P. Cortona, S. Doniach, and C. Sommers. // *Phys. Rev. A.* – 1985. – Vol. 31. – P. 2842–2850.
- [167] Ebert H. Magneto-optical effects in transition metal systems. / H. Ebert. // *Rep. Prog. Phys.* – 1996. – Vol. 59. – P. 1665–1735.
- [168] Hannon J. P. X-Ray Resonance Exchange Scattering. / J. P. Hannon, G. T. Trammell, M. Blume, and Doon Gibbs. // *Phys. Rev. Lett.* – 1988. – Vol. 61. – P. 1245.
- [169] Hannon J. P. X-Ray Resonance Exchange Scattering. / J. P. Hannon, G. T. Trammell, M. Blume, and Doon Gibbs. // *Phys. Rev. Lett.* – 1989. – Vol. 62. – P. 2644.
- [170] Lovesey S. W. X-Ray Scattering and Absorption by Magnetic Materials. / S. W. Lovesey and S. P. Collins. // Oxford: Oxford University Press. – 1996.
- [171] Kortright J. B. Resonant magneto-optical properties of Fe near its  $2p$  levels: Measurement and applications. / J. B. Kortright and Sang-Koog Kim. // *Phys. Rev. B.* – 2000. – Vol. 62. – P. 12216.
- [172] Kleiner W. H. Space-Time Symmetry of Transport Coefficients. / W. H. Kleiner. // *Phys. Rev.* – 1966. – Vol. 142. – P. 318.
- [173] Erskine J. L. Calculation of the  $M_{2,3}$  magneto-optical absorption spectrum of ferromagnetic nickel. / J. L. Erskine and E. A. Stern. // *Phys. Rev. B.* – 1975. – Vol. 12. – P. 5016.
- [174] Thole B. T. Strong Magnetic Dichroism Predicted in the  $M_{4,5}$  X-Ray Absorption

- Spectra of Magnetic Rare-Earth Materials. / B. T. Thole, G. van der Laan, and G. A. Sawatzky. // [Phys. Rev. Lett.](#) – 1985. – Vol. 55. – P. 2086.
- [175] van der Laan Gerrit. Experimental proof of magnetic x-ray dichroism. / Gerrit van der Laan, Bernard T. Thole, George A. Sawatzky, Jeroen B. Goedkoop, John C. Fuggle, Jean-Marc Esteva, Ramesh Karnatak, J. P. Remeika, and Hanna A. Dabkowska. // [Phys. Rev. B.](#) – 1986. – Vol. 34. – P. 6529.
- [176] Schütz G. Absorption of circularly polarized x-rays in iron. / G. Schütz, W. Wagner, W. Wilhelm, P. Kienle, R. Zeller, R. Frahm, and G. Materlik. // [Phys. Rev. Lett.](#) – 1987. – Vol. 58. – P. 737.
- [177] Schütz G. Spin-dependent extended x-ray-absorption fine structure: Probing magnetic short-range order. / G. Schütz, R. Frahm, P. Mautner, R. Wienke, W. Wagner, W. Wilhelm, and P. Kienle. // [Phys. Rev. Lett.](#) – 1989. – Vol. 62. – P. 2620.
- [178] Ebert H. Theory of circularly polarized x-ray absorption by ferromagnetic Fe. / H. Ebert, P. Strange, and B. L. Gyorffy. // [J. Appl. Phys.](#) – 1988. – Vol. 63. – P. 3055–3057.
- [179] Chen C. T. Soft-x-ray magnetic circular dichroism at the  $L_{2,3}$  edges of nickel. / C. T. Chen, F. Sette, Y. Ma, and S. Modesti. // [Phys. Rev. B.](#) – 1990. – Vol. 42. – P. 7262(R)–7265(R).
- [180] van der Laan G. Strong magnetic x-ray dichroism in  $2p$  absorption spectra of  $3d$  transition-metal ions. / G. van der Laan and B. T. Thole. // [Phys. Rev. B.](#) – 1991. – Vol. 43. – P. 13401.
- [181] Chen C. T. Experimental Confirmation of the X-Ray Magnetic Circular Dichroism Sum Rules for Iron and Cobalt. / C. T. Chen, Y. U. Idzerda, H.-J. Lin, N. V. Smith, G. Meigs, E. Chaban, G. H. Ho, E. Pellegrin, and F. Sette. // [Phys. Rev. Lett.](#) – 1995. – Vol. 75. – P. 152.
- [182] Schneider C. M. Magnetic spectromicroscopy from Fe(100). / C. M. Schneider, K. Holldack, M. Kinzler, M. Grunze, H. P. Oepen, F. Schäfers, H. Petersen, K. Meinel, and J. Kirschner. // [Appl. Physics Lett.](#) – 1993. – Vol. 63. – P. 2432–2434.
- [183] Holldack K. A detector for circular polarization of soft x rays. / K. Holldack,

T. Kachel, F. Schäfers, and I. Packe. // *Rev. Sci. Instrum.* – 1996. – Vol. 67. – P. 2485–2489.

- [184] Argyres Petros N. Theory of the Faraday and Kerr Effects in Ferromagnetics. / Petros N. Argyres. // *Phys. Rev.* – 1955. – Vol. 97. – P. 334.
- [185] Guo G. Y. Spin- and orbital-polarized multiple-scattering theory of magneto-x-ray effects in Fe, Co, and Ni. / G. Y. Guo. // *Phys. Rev. B.* – 1998. – Vol. 55. – P. 11619.
- [186] Durham P. J. Electron Spectroscopy of Metallic Systems. In: P. Phariseu and W. M. Temmerman, editors. *The Electronic Structure of Complex Systems.* / P. J. Durham. // *New York: Plenum.* – 1984. – P. 709–759.
- [187] Venus D. Magnetic dichroism in UV photoemission at off-normal emission: Study of the valence bands. / D. Venus, W. Kuch, M.-T. Lin, C. M. Schneider, H. Ebert, and J. Kirschner. // *Phys. Rev. B.* – 1997. – Vol. 55. – P. 2594.
- [188] Menchero J. G. One-electron theory of core-level photoemission from ferromagnets. / J. G. Menchero. // *Phys. Rev. B.* – 1998. – Vol. 57. – P. 993.
- [189] van der Laan Gerrit. Dichroism in the angle-resolved X-ray photoemission from magnetic materials. / Gerrit van der Laan. // *J. Magn. Magn. Mater.* – 1995. – Vol. 148. – P. 53–57.
- [190] van der Laan G. Theory of simple spectra. / G. van der Laan. // *J. Electron. Spectrosc. Relat. Phenom.* – 1997. – Vol. 86. – P. 41–47.
- [191] van der Laan Gerrit. The role of the spin polarization in x-ray magnetic circular dichroism spectra of itinerant magnets. / Gerrit van der Laan. // *J. Phys.: Condens. Matter.* – 1997. - Vol. 9. – P. L259.
- [192] van der Laan Gerrit. Relation between the angular dependence of magnetic x-ray dichroism and anisotropic ground-state moments. / Gerrit van der Laan. // *Phys. Rev. B.* – 1998. – Vol. 57. – P. 5250.
- [193] Menchero J. G. Spin polarization and many-body effects in Ni 3p core-level photoemission. / J. G. Menchero. // *Phys. Rev. B.* – 1998. – Vol. 57. – P. 1001.
- [194] Fanelsa A. Magnetic dichroism in core-level x-ray photoemission with unpolarized excitation. / A. Fanelsa, R. Schellenberg, F. U. Hillebrecht, E. Kisker, J. G.

- Menchero, A. P. Kaduwela, C. S. Fadley, and M. A. Van Hove. // [Phys. Rev. B.](#) – 1996. – Vol. 54. – P. 17962.
- [195] Henk J. Magnetic circular dichroism in photoemission by linear polarized light. / J. Henk and R. Feder. // [Phys. Rev. B.](#) – 1997. – Vol. 55. – P. 11476.
- [196] Menchero J. G. Theory of photoemission from the Ni 2p core level. / J. G. Menchero. // [Phys. Rev. B.](#) – 1997. – Vol. 55. – P. 5505.
- [197] Schellenberg R. Photoelectron diffraction: A source for magnetic dichroism in angle-resolved photoemission from ferromagnets. / R. Schellenberg, E. Kisker, A. Fanelsa, F. U. Hillebrecht, J. G. Menchero, A. P. Kaduwela, C. S. Fadley, and M. A. Van Hove. // [Phys. Rev. B.](#) – 1998. – Vol. 57. – P. 14310.
- [198] Ebert H. Polarization dependence of the 2p-core-level photoemission spectra of Fe. / H. Ebert, L. Baumgarten, C. M. Schneider, and J. Kirschner. // [Phys. Rev. B.](#) – 1991. – Vol. 44. – P. 4406.
- [199] Ebert H. A relativistic description of spin- and angular-resolved core level photoemission spectroscopy for magnetic solids. / H. Ebert and G.-Y. Guo. // [J. Magn. Magn. Mater.](#) – 1995. – Vol. 148. – P. 174–176.
- [200] Guo G. Y. First-principles calculation of magnetic x-ray dichroism in Fe and Co multilayers. / G. Y. Guo, H. Ebert, W. M. Temmerman, and P. J. Durham. // [Phys. Rev. B.](#) – 1994. – Vol. 50. – P. 3861.
- [201] Tamura E. Linear and Circular Dichroism in Angle Resolved Fe 3p Photoemission. / E. Tamura, G. D. Waddill, J. G. Tobin, and P. A. Sterne. // [Phys. Rev. Lett.](#) – 1994. – Vol. 73. – P. 1533.
- [202] Arola E. Self-interaction-corrected relativistic theory of magnetic scattering of x rays: Application to praseodymium. / E. Arola, M. Horne, P. Strange, H. Winter, Z. Szotek, and W. M. Temmerman. // [Phys. Rev. B.](#) – 2004. – Vol. 70. – P. 235127.
- [203] Nemoshkalenko V. V. Electronic Structure and Soft X-Ray Emission Spectra of 5d Transition Metals. / V. V. Nemoshkalenko, V. N. Antonov, Vl. N. Antonov, W. John, H. Wonn, and P. Ziesche. // [Phys. status solidi B.](#) – 1982. – Vol. 111. – P. 11–52.
- [204] Thole B. T. Branching ratio in x-ray absorption spectroscopy. / B. T. Thole and

- G. van der Laan. // *Phys. Rev. B.* – 1988. – Vol. 38. – P. 3158.
- [205] Thole B. T. X-ray circular dichroism as a probe of orbital magnetization. / B. T. Thole, P. Carra, F. Sette, and G. van der Laan. // *Phys. Rev. Lett.* – 1992. – Vol. 68. – P. 1943.
- [206] Carra Paolo. X-ray circular dichroism and local magnetic fields. / Paolo Carra, B. T. Thole, Massimo Altarelli, and Xindong Wang. // *Phys. Rev. Lett.* – 1993. – Vol. 70. – P. 694.
- [207] Ankudinov A. Sum rules for polarization-dependent x-ray absorption. / A. Ankudinov and J. J. Rehr. // *Phys. Rev. B.* – 1995. – Vol. 51. – P. 1282.
- [208] Guo G. Y. Interpretation of x-ray circular dichroism: Multiple-scattering theory approach. / G. Y. Guo. // *Phys. Rev. B.* – 1998. – Vol. 57. – P. 10295.
- [209] Luo Jin. Scattering operator for elastic and inelastic resonant x-ray scattering. / Jin Luo, G. T. Trammell, and J. P. Hannon. // *Phys. Rev. Lett.* – 1993. – Vol. 71. – P. 287.
- [210] Wu Y. Enhanced orbital magnetic moment on Co atoms in Co/Pd multilayers: A magnetic circular x-ray dichroism study. / Y. Wu, J. Stöhr, B. D. Hermsmeier, M. G. Samant, and D. Weller. // *Phys. Rev. Lett.* – 1992. – Vol. 69. – P. 2307.
- [211] Guo G. Y. Magnetic X-ray Dichroism and Anisotropy Energy of Fe and Co Multilayers. In: J. S. Faulkner and R. G. Jordan, editors. *Metallic Alloy: Experimental and Theoretical Perspective*. / G. Y. Guo, H. Ebert, W. M. Temmerman, and P. J. Durham. // Dordrecht: Kluwer Academic. – 1994. – P. 339–348.
- [212] Wu Ruqian. Limitation of the Magnetic-Circular-Dichroism Spin Sum Rule for Transition Metals and Importance of the Magnetic Dipole Term. / Ruqian Wu and A. J. Freeman. // *Phys. Rev. Lett.* – 1994. – Vol. 73. – P. 1994.
- [213] Tjeng L. H. Magnetic circularly polarized  $2p$  resonant photoemission of nickel. / L. H. Tjeng, C. T. Chen, P. Rudolf, G. Meigs, G. van der Laan, and B. T. Thole. // *Phys. Rev. B.* – 1994. – Vol. 48. – P. 13378.
- [214] Zaanen J.  $L_{2,3}$  absorption spectra of the lighter  $3d$  transition metals. / J. Zaanen, G. A. Sawatzky, J. Fink, W. Speier, and J. C. Fuggle. // *Phys. Rev. B.* – 1985. – Vol. 32. – P. 4905.

- [215] Richtmyer F. K. The widths of the  $L$ -series and of the energy levels of Au(79). / F. K. Richtmyer, S. W. Barnes, and E. Ramberg. // *Phys. Rev.* – 1934. – Vol. 46. – P. 843.
- [216] Campbell J.L. Widths of the atomic K-N7 levels. / J.L. Campbell and Tibor Papp. // *At. Data Nucl. Data Tables.* – 2001. – Vol. 77. – P. 1–56.
- [217] Perdew John P. Accurate and simple analytic representation of the electron-gas correlation energy. / John P. Perdew and Yue Wang. // *Phys. Rev. B.* – 1992. – Vol. 45. – P. 13244–13249.
- [218] Perdew John P. Erratum: Accurate and simple analytic representation of the electron-gas correlation energy [Phys. Rev. B 45, 13244 (1992)]. / John P. Perdew and Yue Wang. // *Phys. Rev. B.* – 1992. – Vol. 45. – P. 079904.
- [219] Perdew John P. Generalized Gradient Approximation Made Simple. / John P. Perdew, Kieron Burke, and Matthias Ernzerhof. // *Phys. Rev. Lett.* – 1996. – Vol. 77. – P. 3865.
- [220] Perdew John P. Erratum: Generalized Gradient Approximation Made Simple [Phys. Rev. Lett. 77, 3865 (1996)]. / John P. Perdew, Kieron Burke, and Matthias Ernzerhof. // *Phys. Rev. Lett.* – 1997. – Vol. 78. – P. 1396.
- [221] Blöchl P. E. Improved tetrahedron method for Brillouin-zone integrations. / P. E. Blöchl, O. Jepsen, and O. K. Andersen. // *Phys. Rev. B.* – 1994. – Vol. 49. – P. 16223.
- [222] Yaresko A. N. Localized U  $5f$  electrons in UPd<sub>3</sub> from LDA +  $U$  calculations. / A. N. Yaresko, V. N. Antonov, and P. Fulde. // *Phys. Rev. B.* – 2003. – Vol. 67. – P. 155103.
- [223] Solovyev I. V. Corrected atomic limit in the local-density approximation and the electronic structure of  $d$  impurities in Rb. / I. V. Solovyev, P. H. Dederichs, and V. I. Anisimov. // *Phys. Rev. B.* – 1994. – Vol. 50. – P. 16861–16871.
- [224] Dederichs P. H. Ground States of Constrained Systems: Application to Cerium Impurities. / P. H. Dederichs, S. Blügel, R. Zeller, and H. Akai. // *Phys. Rev. Lett.* – 1984. – Vol. 53. – P. 2512–2515.
- [225] Pickett W. E. Reformulation of the LDA +  $U$  method for a local-orbital basis. /

- W. E. Pickett, S. C. Erwin, and E. C. Ethridge. // [Phys. Rev. B.](#) – 1998. – Vol. 58. – P. 1201–1209.
- [226] Cococcioni Matteo. Linear response approach to the calculation of the effective interaction parameters in the LDA + U method. / Matteo Cococcioni and Stefano de Gironcoli. // [Phys. Rev. B.](#) – 2005. – Vol. 71. – P. 035105.
- [227] Nakamura Kazuma. First-principles calculation of effective onsite Coulomb interactions of 3d transition metals: Constrained local density functional approach with maximally localized Wannier functions. / Kazuma Nakamura, Ryotaro Arita, Yoshihide Yoshimoto, and Shinji Tsuneyuki. // [Phys. Rev. B.](#) – 2006. – Vol. 74. – P. 235113.
- [228] Aryasetiawan F. Frequency-dependent local interactions and low-energy effective models from electronic structure calculations. / F. Aryasetiawan, M. Imada, A. Georges, G. Kotliar, S. Biermann, and A. I. Lichtenstein. // [Phys. Rev. B.](#) – 2004. – Vol. 70. – P. 195104.
- [229] Solovyev I. V. Screening of Coulomb interactions in transition metals. / I. V. Solovyev and M. Imada. // [Phys. Rev. B.](#) – 2005. – Vol. 71. - P. 045103.
- [230] Antropov V. P. Magnetic anisotropic effects and electronic correlations in MnBi ferromagnet. / V. P. Antropov, V. N. Antonov, L. V. Bekenov, A. Kutepov, and G. Kotliar. // [Phys. Rev. B.](#) – 2014. – Vol. 90. – P. 054404.
- [231] Aryasetiawan F. Calculations of Hubbard  $U$  from first-principles. / F. Aryasetiawan, K. Karlsson, O. Jepsen, and U. Schönberger. // [Phys. Rev. B.](#) – 2006. – Vol. 74. – P. 125106.
- [232] Lie K. Theoretical site- and symmetry-resolved density of states and experimental EELS near-edge spectra of AlB<sub>2</sub> and TiB<sub>2</sub>. / K. Lie, R. Høier, and R. Brydson. // [Phys. Rev. B.](#) – 2000. – Vol. 61. – P. 1786–1794.
- [233] Mo Shang-Di. *Ab initio* calculation of the core-hole effect in the electron energy-loss near-edge structure. / Shang-Di Mo and W. Y. Ching. // [Phys. Rev. B.](#) – 2000. – Vol. 62. – P. 7901–7907.
- [234] Mo S.-D. X-ray absorption near-edge structure in alpha-quartz and stishovite: *Ab initio* calculation with core–hole interaction. / S.-D. Mo and W. Y. Ching. //

[Appl. Physics Lett.](#) – 2001. – Vol. 78. – P. 3809–3811.

- [235] Yong-Nian Xu. Core exciton, valence exciton, and optical properties of yttrium aluminum garnet ( $\text{Y}_3\text{Al}_5\text{O}_{12}$ ). / Yong-Nian Xu, Yu Chen, Shang-Di Mo, and W. Y. Ching. // [Phys. Rev. B.](#) – 2002. – Vol. 65. – P. 235105.
- [236] Ching Wai-Yim. Calculation of XANES/ELNES Spectra of All Edges in  $\text{Si}_3\text{N}_4$  and  $\text{Si}_2\text{N}_2\text{O}$ . / Wai-Yim Ching, Shang-Di Mo, and Yu Chen. // [J. Am. Ceram. Soc.](#) – 2002. – Vol. 85. – P. 11.
- [237] Mizoguchi Teruyasu. First-principles calculations of ELNES and XANES of selected wide-gap materials: Dependence on crystal structure and orientation. / Teruyasu Mizoguchi, Isao Tanaka, Satoru Yoshioka, Masahiro Kunisu, Tomoyuki Yamamoto, and W. Y. Ching. // [Phys. Rev. B.](#) – 2004. – Vol. 70. – P. 045103.
- [238] Saib S. Structural phase transformations of GaN and InN under high pressure. / S. Saib and N. Bouarissa. // [Physica B.](#) – 2007. – Vol. 387. – P. 377–382.
- [239] Blöchl P. E. Projector augmented-wave method. / P. E. Blöchl. // [Phys. Rev. B.](#) – 1994. – Vol. 50. – P. 17953.
- [240] Kresse G. From ultrasoft pseudopotentials to the projector augmented-wave method. / G. Kresse and D. Joubert. // [Phys. Rev. B.](#) – 1999. – Vol. 59. – P. 1758.
- [241] Pickett Warren E. Electronic structure and half-metallic transport in the  $\text{La}_{1-x}\text{Ca}_x\text{MnO}_3$  system. / Warren E. Pickett and David J. Singh. // [Phys. Rev. B.](#) – 1996. – Vol. 53. – P. 1146.
- [242] Antonov V. N. X-ray magnetic dichroism in the III-V diluted magnetic semiconductors: First principle calculations. / V. N. Antonov, A. N. Yaresko, and O. Jepsen. // [Phys. Rev. B.](#) – 2010. – Vol. 81. – P. 075209.
- [243] Schwitalla J. Electron Core-Hole Interaction in the X-Ray Absorption Spectroscopy of 3d Transition Metals. / J. Schwitalla and H. Ebert. // [Phys. Rev. Lett.](#) – 1998. – Vol. 80. – P. 4586.
- [244] Thakur P. Electronic structure of Cu-doped ZnO thin films by x-ray absorption, magnetic circular dichroism, and resonant inelastic x-ray scattering. / P. Thakur, V. Bisogni, J. C. Cezar, N. B. Brookes, G. Ghiringhelli, S. Gautam, K. H. Chae,

- M. Subramanian, R. Jayavel, and K. Asokan. // *J. Appl. Phys.* – 2010. – Vol. 107. – P. 103915.
- [245] Ruiz-Fuertes J. Ambient-temperature high-pressure-induced ferroelectric phase transition in CaMnTi<sub>2</sub>O<sub>6</sub>. / J. Ruiz-Fuertes, T. Bernert, D. Zimmer, N. Schrotter, M. Koch-Müller, B. Winkler, L. Bayarjargal, C. Popescu, S. MacLeod, and K. Glazyrin. // *Phys. Rev. B.* – 2017. – Vol. 96. – P. 094101.
- [246] Antonov Victor. Electronic Structure and Magneto-Optical Properties of Solids. / Victor Antonov, Bruce Harmon, and Alexander Yaresko. // *Dordrecht: Springer Dordrecht.* – 2004.
- [247] Sefat Athena S. High-resolution EELS study of the vacancy-doped metal/insulator system, Nd<sub>1-x</sub>TiO<sub>3</sub>,  $x = 0$  to 0.33. / Athena S. Sefat, Gisele Amow, Meng-Yue Wu, Gianluigi A. Botton, and J.E. Greedan. // *J. Solid State Chem.* – 2005. – Vol. 178. – P. 1008–1016.
- [248] Krüger Peter. X-ray absorption spectra at the Ca  $L_{2,3}$  edge calculated within multichannel multiple scattering theory. / Peter Krüger and Calogero R. Natoli. // *Phys. Rev. B.* – 2004. – Vol. 70. – P. 245120.
- [249] Ankudinov A. L. Dynamic screening effects in x-ray absorption spectra. / A. L. Ankudinov, A. I. Nesvizhskii, and J. J. Rehr. // *Phys. Rev. B.* – 2003. – Vol. 67. – P. 115120.
- [250] Rhee H. B. Strong interactions, narrow bands, and dominant spin-orbit coupling in Mott insulating quadruple perovskite CaCo<sub>3</sub>V<sub>4</sub>O<sub>12</sub>. / H. B. Rhee and W. E. Pickett. // *Phys. Rev. B.* – 2014. – Vol. 90. – P. 205119.
- [251] Ebert H. Fully relativistic treatment of core states for spin-dependent potential. / H. Ebert. // *J. Phys.: Condens. Matter.* – 1989. – Vol. 1. – P. 9111.